Geofluids

Seepage Characteristics of Fractured Rock Mass Under Multi-Field Coupling

Lead Guest Editor: Yiding Bao
Guest Editors: Defeng Wang and Chen Cao

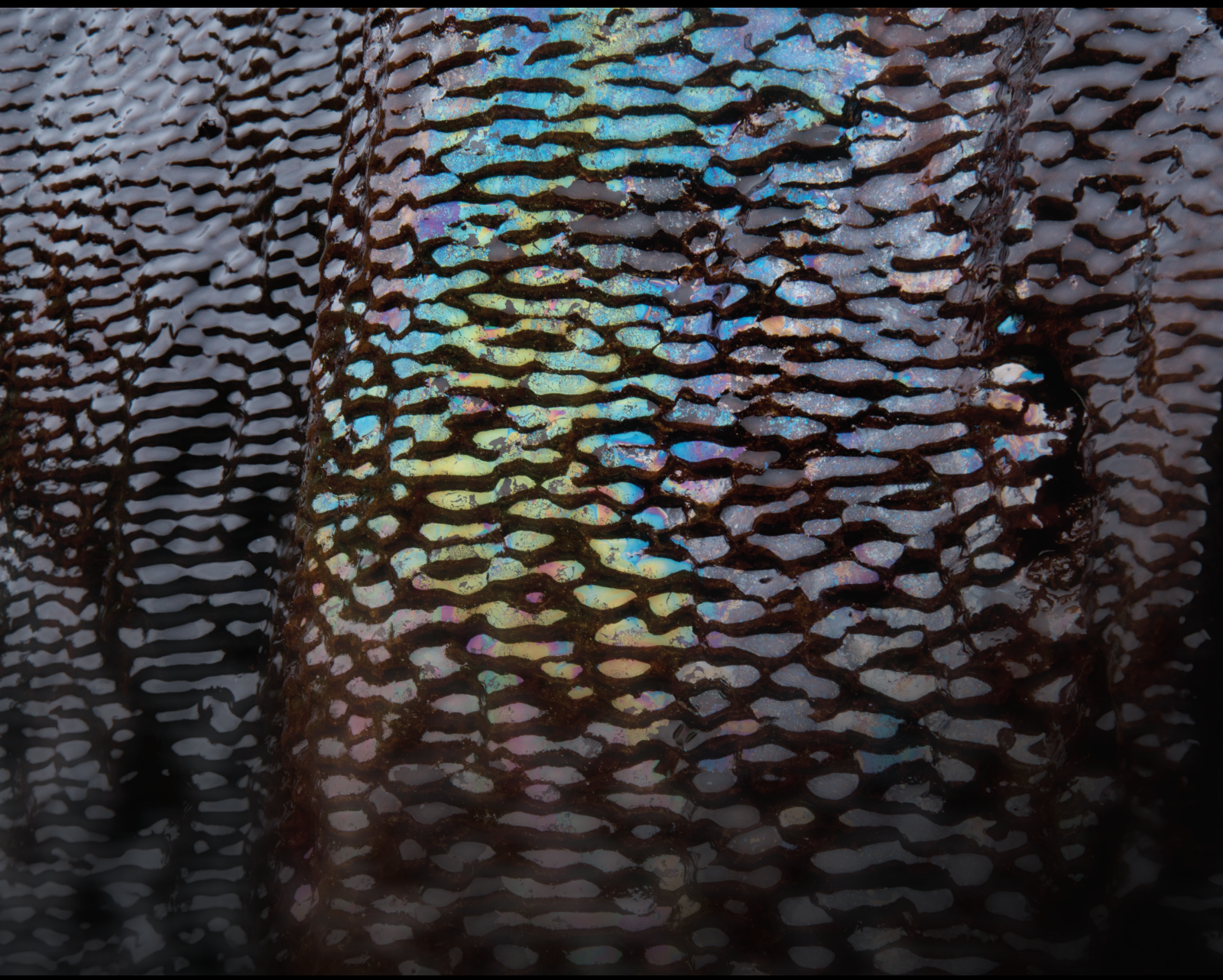

Seepage Characteristics of Fractured Rock Mass Under Multi-Field Coupling

Geofluids

Seepage Characteristics of Fractured Rock Mass Under Multi-Field Coupling

Lead Guest Editor: Yiding Bao
Guest Editors: Defeng Wang and Chen Cao

Chief Editor

Associate Editors

Academic Editors

Contents

Hindawi
Geofluids
Volume 2024, Article ID 4572483, 9 pages
https://doi.org/10.1155/2024/4572483

Research Article

A Numerical Simulation Approach for Superheated Steam Flow during Multipoint Steam Injection in Horizontal Well

Qiuying Du, Mingzhong Li, Chenwei Liu, Zhifeng Bai, Chenru Zhou, and Xiangyu Wang

School of Petroleum Engineering, China University of Petroleum, Qingdao 266580, China

Correspondence should be addressed to Mingzhong Li; limingzhong_upc@hotmail.com

Received 4 September 2022; Revised 12 October 2022; Accepted 23 January 2023; Published 19 January 2024

Academic Editor: Yiding Bao

Superheated steam flow during multipoint steam injection technology has a good effect on improving the steam absorption profile of heavy oil thermal recovery wells, enhancing the production degree of horizontal section of thermal recovery wells, and enhancing oil recovery. Based on the structure of multipoint steam injection horizontal string, considering the characteristics of variable mass flow, pressure drop of steam-liquid two-phase flow, and throttling pressure difference of steam injection valve in the process of steam injection, this paper establishes the calculation model of various parameters of multipoint steam injection horizontal wellbore and calculates the distribution of steam injection rate, temperature, pressure gradient, and dryness along the section of multipoint steam injection in horizontal wellbore. The results show that the temperature and pressure decrease gradually from heel to toe, and the steam dryness decreases gradually. Considering the influence of throttle pressure difference of steam injection valve and pressure drop of gas-liquid two-phase flow in the wellbore, the traditional calculation model of steam injection thermodynamic parameters is optimized, and the optimization of wellbore structure and steam injection parameters is an effective method to achieve uniform steam injection in horizontal wells. The steam injection uniformity of horizontal wells can be effectively improved by adjusting the steam injection valve spacing and steam injection parameters. When the steam injection volume is 200 m^3/d and the steam injection valve spacing is 20 m, a more stable steam injection effect can be obtained. The findings of this study can help for better understanding of improving the uniformity of steam injection and enhancing the recovery factor.

1. Introduction

In the process of heavy oil production, the horizontal well has a large contact area with the reservoir, the range of steam injection is wide, and the productivity is higher than that of the vertical well [1, 2]. The multipoint steam injection technology in horizontal wells is widely used to improve the uniformity of steam injection, to optimize the steam chamber, and to enhance oil recovery [3]. This technology is widely used in Liaohe, Shengli, and Xinjiang oilfields, and the result is that technology can improve reservoir productivity, improve the steam injection uniformity, and enhance the oil recovery [4, 5]. However, there are few theoretical studies on this technology. A steady thermodynamic calculation model of gas-liquid two-phase flow in a steam injection column of multipoint steam injection was established [6], and the vapor injection valve with uniform distribution of the steam injection volume in horizontal wells was optimized as the objective function. However, due to the heterogeneity of the heavy oil reservoir and the effect of the vapor energy loss along the channel after the horizontal well scale implementation, there is a general problem of the heterogeneous production of horizontal tanks in the process of general steam injection [7–9]. Taking into account the above problem, scientists design a distributor that limits multiple flows to horizontal wells, injecting steam into multiple locations of horizontal reservoirs simultaneously through distributors.

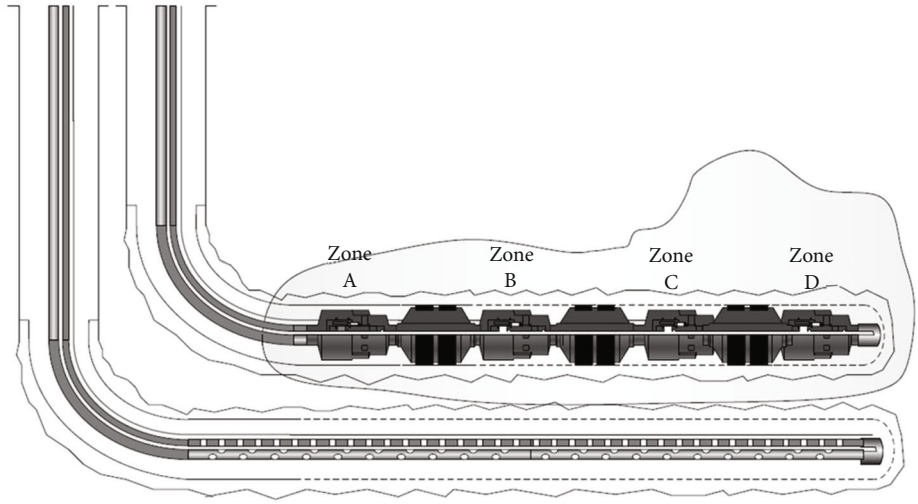

Figure 1: Wellbore structure and steam chamber expansion diagram of multipoint steam injection well.

In previous studies, the uniformity of multipoint steam injection is affected by the steam injection parameters and the location of the steam injection point, and the development of the steam cavity is not uniform, as shown in Figure 1; there are few studies on the optimization of the steam injection device and steam injection parameters [10].

To make stability of superheated steam injected into formation, get the uniform expansion of the steam chamber. First, the mathematical model is presented. Then, three-dimensional numerical simulation was carried out on the multipoint steam injection string, and the variation of parameters along the multipoint steam injection was analyzed to obtain the variable mass flow law of superheated steam in the wellbore. Finally, the steam injection situation under different steam injection volumes and steam injection positions was compared to optimize the steam injection uniformity. However, this paper only optimizes the parameters of steam injection volume and steam injection valve configuration, without considering other potential influencing factors, and will continue to explore and study related influencing factors in the future.

2. Mathematical Model

Fluid flow process in multipoint steam injection horizontal well is shown in Figure 2.

2.1. Basic Assumptions of the Model

(1) The oil reservoir in the horizontal portion is divided equally in the horizontal direction, and the thermal physical parameter of the reservoir does not vary with the change in temperature

(2) When heat is transferred from the well to the outer edge of cementation, steady heat transfer occurs, and unsteady heat transfer occurs when the heat is transferred from the outer edge of the cement ring to the heat storage chamber

(3) The horizontal well is divided into n microsegments, and the vapor injected into the same microsegment is uniformly sucked into the reservoir

2.2. Calculation of Pressure Gradient along the Path. After the saturated vapor is injected into the wellbore, it becomes a gas-liquid two-phase flow, and the gas-liquid two-phase flow is required to calculate the pressure change. According to the pressure gradient equation, the pressure gradient equation mainly includes friction loss pressure gradient, potential energy pressure gradient, and kinetic energy pressure gradient model [11–13].

The pressure gradient equation is expressed as Equation (1) by the conservation of mass and momentum.

$$\frac{\Delta p}{\Delta Z} = \frac{\rho_m g \sin\theta - \tau_f}{1 - \left(i_s q / A_p^2 p\right)}, \tag{1}$$

where p is the pressure at the well point, Pa; Z is the depth, m; ρ_m is wet vapor density, kg/m^3; g is the acceleration of gravity, m/s^2; θ is an angle between the well and the horizontal direction, °; τ_f is the friction loss slope, Pa/m; i_s is the steam mass flow rate, kg/s; q is the volume flow of steam, m^3/s; A_p is the cross-section of the tubing, m^2.

2.3. A Computational Model of Temperature in the Well. The temperature and pressure of saturated steam have a coupling relationship, as shown in the following equation:

$$T_s = 210.2376 p_s^{0.21} - 30, \tag{2}$$

where T_s is the temperature of steam, °C, and P_s is the steam pressure, MPa.

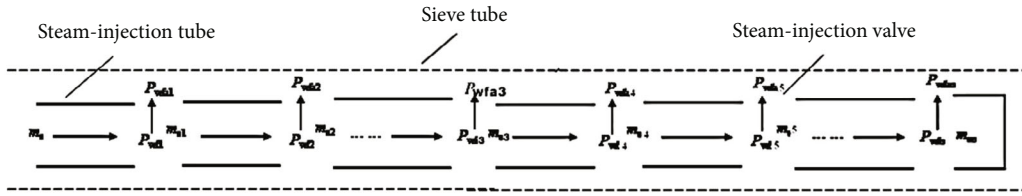

Figure 2: Horizontal well steam injection simulation diagram.

2.4. A Model of Steam Dryness along Well. Based on the law of energy conservation, at the same time and at the same depth, the heat loss is equivalent to the energy loss of the wet steam [14, 15], as shown in the following equation:

$$\frac{dQ}{dZ} = -i_s \frac{\mathrm{dh}_m}{dZ} - i_s \frac{d}{dZ}\left(\frac{v^2}{2}\right) + i_s g, \tag{3}$$

where Q is heat loss, J; h_m is the specific heat enthalpy of wet saturated steam, kJ/kg; v is the wet steam velocity, m/s.

After finishing Equation (3), we can get

$$C_1 \frac{\mathrm{dx}}{dZ} + C_2 x + C_3 = 0. \tag{4}$$

Among them, $C_1 = i_s(h_s - h_w)$.

$$\begin{aligned} C_2 &= i_s\left[\left(\frac{\mathrm{dh}_s}{\mathrm{dp}} - \frac{\mathrm{dh}_w}{\mathrm{dp}}\right)\frac{\mathrm{dp}}{dZ}\right], \\ C_3 &= \frac{dQ}{dZ} + i_s \frac{\mathrm{dh}_s}{\mathrm{dp}}\frac{\mathrm{dp}}{dZ} + \frac{i_s^3}{A^2\rho}\frac{d}{dZ}\left(\frac{1}{\rho}\right) - i_s g, \end{aligned} \tag{5}$$

where h_s is the specific heat enthalpy of dry saturated steam, kJ/kg, and h_w is a specific enthalpy of saturated water, kJ/kg; drying $x_{z,t}$ of any depth Z is expressed as follows [16]:

$$x_{Z,t} = e^{-(C_2/C_1)Z}\left[-\frac{C_3}{C_2}e^{(C_2/C_1)Z} + x_w + \frac{C_3}{C_2}\right], \tag{6}$$

where x_w is the dryness of the initial injected steam, decimal.

2.5. Friction and Calculation of Work Done by Friction. The calculation is as follows: the microelement segment is subdivided into several smaller microelement segments according to the number of slit rows, and the thermophysical parameters of the fluid on each microelement segment are the same [17, 18]. Firstly, the mass flow rate and flow rate of fluid on each small microelement section are calculated, and then the friction force and frictional work on the microelement segment are calculated [19]. Then, the total friction force and frictional work on the microelement section are calculated by superposition [20–22]. The method provides a more detailed description of fluid flow in a slotted screen horizontal wellbore.

The steam absorption capacity of the reservoir of each row slit is

$$m_{\mathrm{sfl}} = \frac{\mathrm{m_{sf}dl}}{\mathrm{dl}/l_u} = m_{\mathrm{sf}} \cdot l_u. \tag{7}$$

The mass flow of the j row slit is

$$m_{\mathrm{sl}}(j) = m_{\mathrm{s},i} - m_{\mathrm{sfl}} \cdot (j\text{-}1)\left(j = 1, 2, \cdots\cdots, p_{\mathrm{gf}}\right). \tag{8}$$

The average flow velocity on the small and microelement segments is

$$v_{\mathrm{sl}}(j) = \frac{m_{\mathrm{sl}}(j)}{\rho_m A} = \frac{4m_{\mathrm{sl}}(j)}{\rho_m \pi D_{\mathrm{in}}^2}. \tag{9}$$

In unit time, the work done by the friction force on the microelement segment is expressed as follows [23–25]:

$$\frac{\Delta W(j) = \tau_{\mathrm{cl}}(j) l_u}{l_u/v_{\mathrm{sl}}(j) = \tau_{\mathrm{cl}}(j) v_{\mathrm{sl}}(j)\left(j = 1, 2, \cdots\cdots, p_{\mathrm{gf}}\right)}, \tag{10}$$

where $\tau_{\mathrm{cl}}(j)$ is the friction force between the steam and the inside of the screen tube, N. The calculation method is

$$\tau_{\mathrm{cl}}(j) = f \cdot \rho_{\mathrm{m}} \cdot \frac{\pi D_{\mathrm{in}} l_u}{8} v_{\mathrm{sl}}^2(j)\left(j = 1, 2, \cdots\cdots, p_{\mathrm{gf}}\right). \tag{11}$$

The expression of the work done by the friction force on the segment of length dl in unit time is

$$dW = \sum_{j=1}^{p_{\mathrm{gf}}} \Delta W(j) = \sum_{j=1}^{p_{\mathrm{gf}}} \tau_{\mathrm{cl}}(j) v_{\mathrm{sl}}(j). \tag{12}$$

The expression of friction on the segment dl is [26, 27]

$$\tau_c = \sum_{j=1}^{p_{\mathrm{gf}}} \tau_{\mathrm{cl}}(j) = \sum_{j=1}^{p_{\mathrm{gf}}} f \cdot \rho_m \cdot \frac{\pi D l_u}{8} v_{\mathrm{sl}}^2(j) = \frac{\rho_m \pi D l_u}{8} \sum_{j=1}^{p_{\mathrm{gf}}} f \cdot v_{\mathrm{sl}}^2(j), \tag{13}$$

where f is the dimensionless friction coefficient [28]. The calculation method of friction coefficient between fluid and pipe wall adopts the conventional calculation method of pipe flow [29, 30], and the calculation process is as follows:

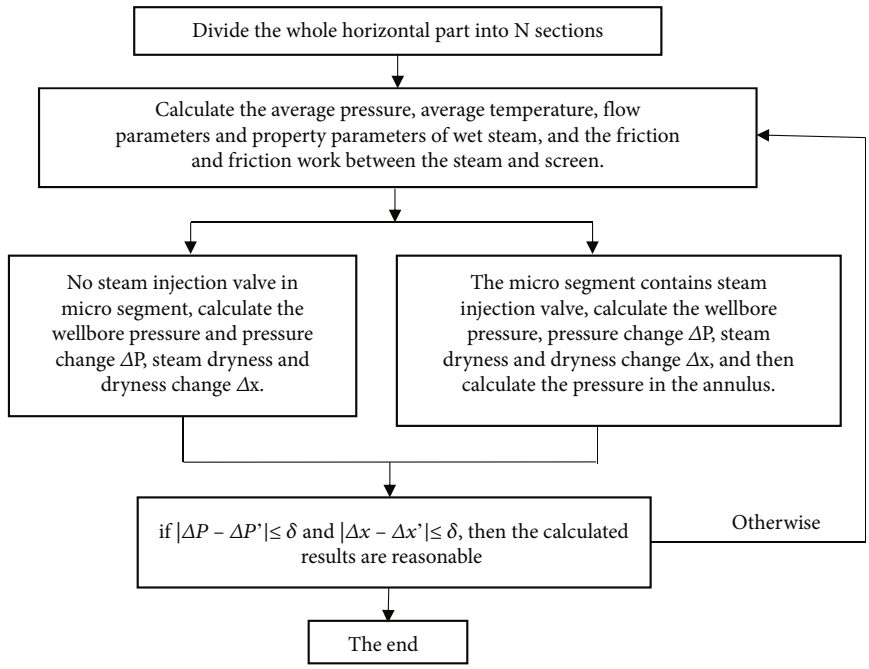

Figure 3: The flow diagram of the calculation model.

(1) Calculate Reynolds number [31–33]

The Reynolds number calculation formula of two-phase flow is as follows:

$$R_e = \frac{v_{sl}^2(j) \cdot D_{in} \cdot [\rho_w E_l + \rho_s(1 - E_l)]}{\mu_w E_l + \mu_s(1 - E_l)}, \tag{14}$$

where R_e is Reynolds number; ρ_w and ρ_s are the density of liquid water and dry saturated steam, kg/m^3; μ_w is the viscosity of hot water in water vapor, MPa·s; μ_s is the viscosity of dry saturated steam in water vapor, MPa·s; E_l is the volume liquid content of inlet, dimensionless.

(2) Determine the flow state and calculate the hydraulic friction coefficient [34, 35]

$$\begin{aligned} &R_e \le 2000, \\ &f = \frac{64}{R_e}, \\ &3000 < R_e < \frac{50.9}{\varepsilon^{8/7}}, \\ &f = \frac{0.3164}{R_e^{0.25}}, \\ &\frac{50.9}{\varepsilon^{8/7}} < R_e < \frac{(665 - 765 \lg \varepsilon)}{\varepsilon}, \\ &f = \left\{-1.81 \lg \left[\left(\frac{\varepsilon}{3.7 D_{in}}\right)^{1.11} + \frac{6.9}{R_e}\right]\right\}^{-2}. \end{aligned} \tag{15}$$

3. Solution of the Model

(1) Vapor pressure, mass flow rate, temperature, and dryness at the heel are known, the whole horizontal part is divided into N sections, and each section is $d_l = L/N$

(2) The pressure drop change ΔP and dryness change Δx of d_l length are estimated as the initial values of iterative calculation, and the average pressure, average temperature, flow parameters and property parameters of the wet steam mixture, and the friction and friction work between the steam and the screen are calculated successively

(3) When there is no steam injection valve in the microsegment, the wellbore pressure and pressure change ΔP as well as steam dryness and dryness change Δx in the microsegment are calculated; when the microsegment contains steam injection valve, the wellbore pressure and pressure change ΔP and steam dryness and dryness change Δx in the microsegment are calculated first, and then the pressure in the annulus is calculated

(4) Compare the calculated Δx and ΔP with the estimated Δx and ΔP in step 2; if $|\Delta P - \Delta P'| \le \delta$ and $|\Delta x - \Delta x'| \le \delta$, then the calculated results are reasonable. Otherwise, $\Delta P = \Delta P'$, $\Delta x = \Delta x'$, and return to step 2 to recalculate

(5) Steps 2 to 4 are repeated to calculate the vapor pressure distribution, temperature, and degree of drying on each microsegment until the cumulative length

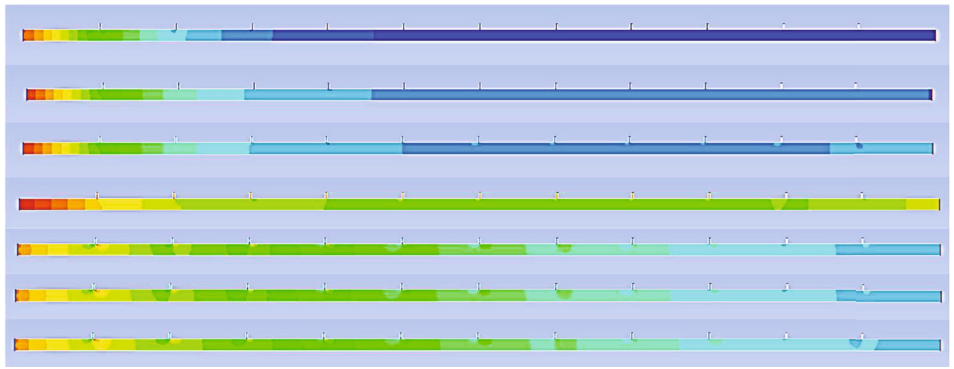

Figure 4: Multipoint steam injection pressure field $t = 3$ s; $t = 6$ s; $t = 9$ s; $t = 12$ s; $t = 15$ s; $t = 18$ s; $t = 21$ s.

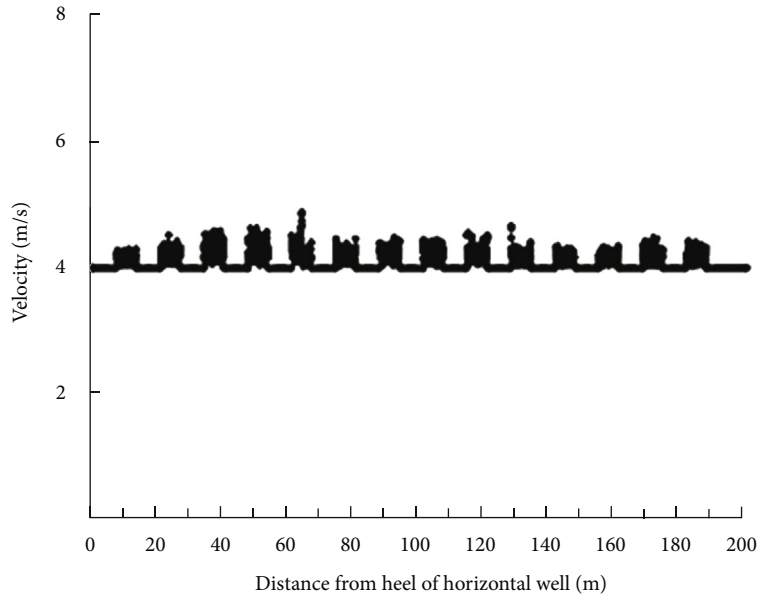

Figure 5: Steam injection velocity distribution curve.

of each microsegment is equal to or greater than the total length of the horizontal well (Figure 3).

4. Case Verification and Analysis

The distribution of pressure field, velocity field, and temperature field in multipoint steam injection wellbore is shown in Figures 4–6. When the steam flows through the steam injection valve, steam flow pressure is reduced, overall speed increased, and temperature decreased, which is close to the changes in the rate of steam injection; the steam valve side first increases then decreases, and the temperature rises after lower first. In order to explore the main factors affecting uniform steam injection, the steam injection velocity, the distance between the steam injection valves, and the steam drying performance are numerically simulated.

Based on the basic geological data of the Maccan River oilfield, a multipoint steam injection horizontal well model was established. The 3-dimensional model data are shown in Tables 1–3.

4.1. Effect of Steam Injection Rate Change on Uniform Steam Injection. In order to explore the influence of the change of steam injection speed on multipoint steam injection, the interval between the opening area of the steam injection valve and the control valve is constant. The quantity of steam injection was performed for 100 m^3/d, 150 m^3/d, and 200 m^3/d (Figure 7); as the amount of steam injection increases, more steam is injected into the reservoir near the horizontal well, resulting in good steam injection uniformity and an increase in cumulative oil production. When the quantity of steam injection reaches 200 m^3/d, the production efficiency is the highest.

4.2. Influence of Changing Steam Injection Valve Spacing on Uniform Steam Injection. The external screen structure remains unchanged, and the steam injection valve spacing was adjusted to 10 m, 20 m, and 30 m, respectively, to reestablish the mathematical model and conduct numerical simulation (Figure 8); with the decrease of steam injection valve spacing, more steam is injected into the reservoir near the heel of the horizontal well, while the steam reaching the

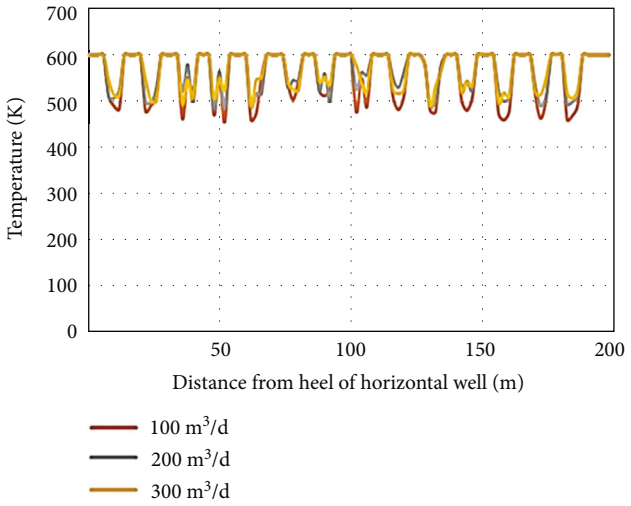

Figure 6: Influence of steam valve distribution on temperature field variation.

Table 1: Heat transfer characteristic data.

Volumetric heat capacity of rock (J/(m^3*C))	0.0000014
Thermal conductivity of rock (m*day*C)	220
Thermal conductivity of water (m*day*C)	0.000002
Thermal conductivity of steam (m*day*C)	2390000

Table 2: Steam injection data.

Horizontal well length (m)	850
Steam injection pressure (MPa)	2
Steam injection rate (kg/s)	1.73
Injection pressure (MPa)	2.12
Steam injection temperature (K)	500
Steam dryness (%)	95

Table 3: Screen structure basic data.

Gap density (slot/m)	446
Gap length (mm)	60
Screen outside diameter (mm)	219.1
Buried depth (m)	450-1400
Sieve tube cut seam wide (mm)	0.3048
Screen inner diameter (mm)	201.2
Slot axial spacing (mm)	7.112
Slot radial spacing (mm)	33.274

toe of the horizontal section gradually decreases; the heating effect of the reservoir near the toe deteriorates, and it brings about the good heating effect of the reservoir near the heel. When the interval of the steam injection valve is 20 m, the ground layer has a good heating effect. The heterogeneity of the steam chamber is more serious if the distance between the steam injection valves is 10 m compared with the steam injection valve. In short, when the number of control valves is 20 m, the injection production profile and the steam

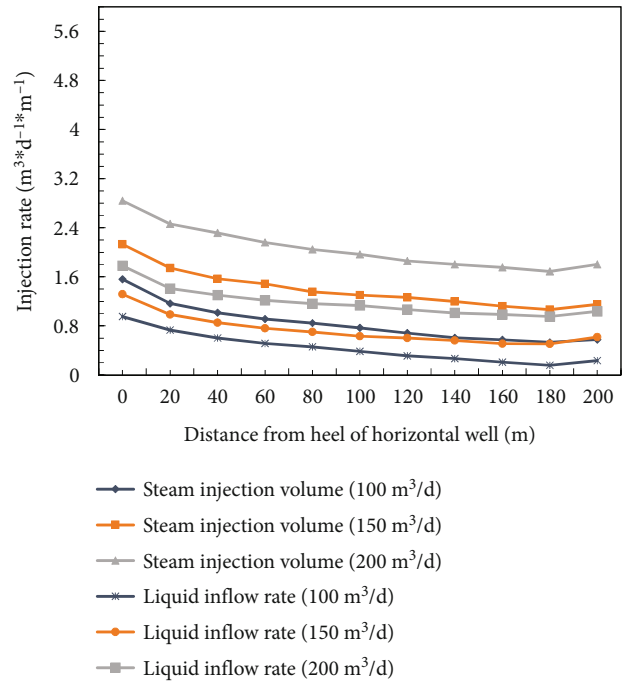

Figure 7: Injection and production profiles with different steam injection volumes.

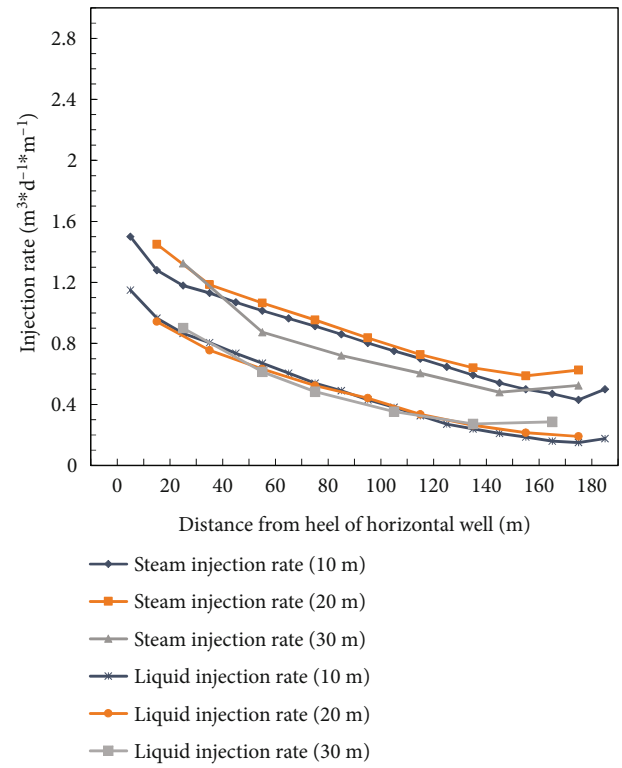

Figure 8: Injection-production profiles with different valve spacing.

chamber are uniformly distributed, and the best steam injection effect can be obtained.

In the schematic diagram of the temperature field change in the wellbore, the steam flow velocity in the steam injection tube is closely related to the position of the steam injection

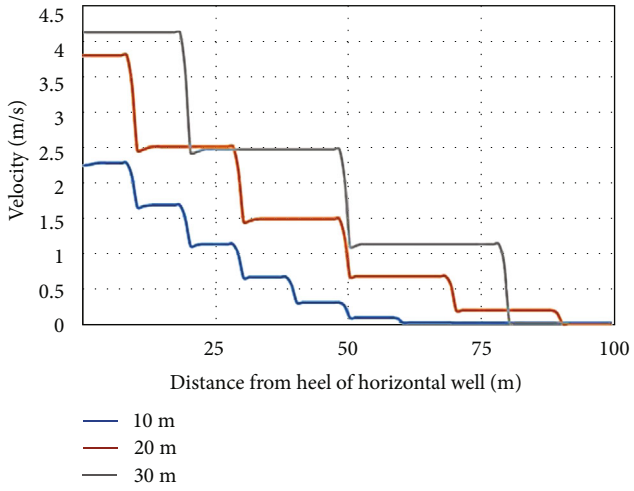

Figure 9: Influence of steam valve distribution on velocity field variation.

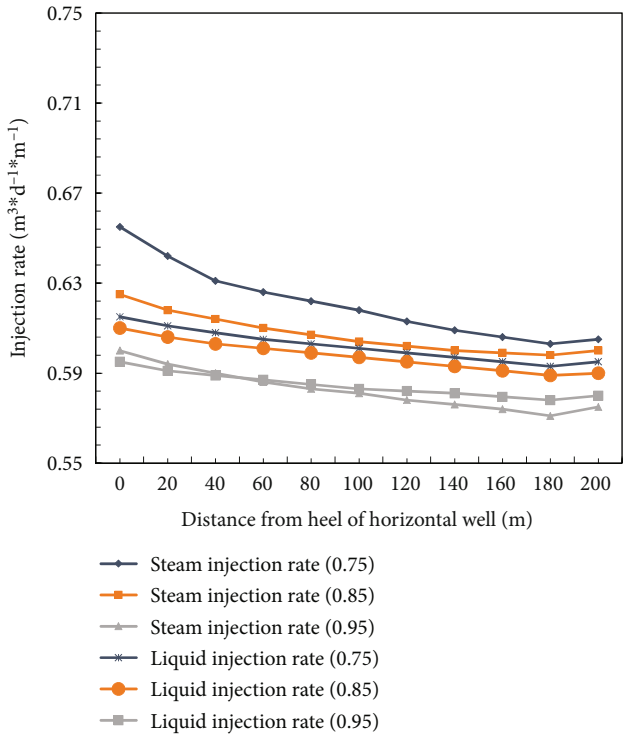

Figure 10: Injection-production profiles with different steam dryness.

valve (Figure 9). Whenever the steam flows into the wellbore annulus through the steam injection valve, the steam speed will drop sharply. In the process of flow in the injection tube, the velocity remains relatively stable.

4.3. Effect of Changing Steam Dryness on Uniform Steam Injection. With the increase in vapor dryness, the vapor density decreases, the steam velocity increases in the well, the friction loss of the vapor in the flow process increases, and the decrease of vapor pressure increases. To explore the influence of steam dryness on the uniformity of steam injection, under the same conditions of other parameters, the variation law of uniform distribution of steam injection profile was compared when the steam dryness was 0.75, 0.85, and 0.95, respectively (Figure 10). With the increase of steam dryness, the average steam inlet flow and liquid inlet flow in the horizontal section of the horizontal well gradually decreased, but the distribution uniformity of the steam injection profile gradually increased.

5. Summary and Conclusions

Characteristics of variable mass flow rate in the steam injection process are considered based on a multipoint steam injection horizontal well. A calculation model of various parameters of multipoint steam injection horizontal well was established. Practical examples of multipoint steam injection are introduced. In order to calculate the vapor parameters along the well in the multipoint steam injection process, the nodal point analysis method is adopted. The effect of the steam injection parameter and the interval of the steam injection valve were analyzed on the vapor parameter along the well in the multipoint steam injection process. The following conclusions can be drawn from this study:

(1) When the steam flows into the steam injection valve, the pressure decreases, the gas-liquid two-phase flow rate accelerates, the temperature decreases remarkably, and the friction loss becomes large

(2) The well injection pressure hardly affects the heat loss of steam injection, and the heat loss in the well decreases with the increase of the distance between steam injection valves. The higher the injection rate, the higher the heat supplement is, the lower the heat loss is, and the higher the dryness of bottomhole steam is

(3) In the actual steam injection process in the mine, the amount of steam injection can be increased appropriately to increase the dry steam at the bottom of the well, and the distance between the steam injection valves cannot be reduced

Data Availability

Data can be obtained from the corresponding author.

Conflicts of Interest

The authors declare that there is no conflict of interest regarding the publication of this paper.

Acknowledgments

This work was supported by the National Science and Technology Major Project (No. 2016ZX05031-002) and the National Natural Science Foundation of China (No. 51704190).

References

[1] F. Sun, Y. Yao, G. Li et al., "An improved two-phase model for saturated steam flow in multi-point injection horizontal wells under steady-state injection condition," *Journal of Petroleum ence & Engineering*, vol. 167, article 0518303620, pp. 844–856, 2018.

[2] P. Li, Y. Zhang, H. Hu, Y. Liu, Y. Liu, and H. Chen, "Optimization of the slotted liners parameters during dual tubing steam injection process," *IOP Conference Series Earth and Environmental Science*, vol. 431, no. 1, article 012042, 2020.

[3] F. Sun, Y. Yao, and X. Li, "The heat and mass transfer characteristics of superheated steam coupled with non-condensing gases in horizontal wells with multi-point injection technique," *Energy*, vol. 143, pp. 995–1005, 2017.

[4] X. Feng, J. Qinghui, Y. Zuyang, and Z. Xiaobo, "Nonlinear flow behavior through rough-walled rock fractures: the effect of contact area," *Computers and Geotechnics*, vol. 102, pp. 179–195, 2018.

[5] H. Chen, M. Li, Q. Di, and C. Liu, "Numerical simulation of the outflow performance for horizontal wells with multiple steam injection valves," *Acta Petrolei Sinica*, vol. 38, no. 6, pp. 696–704, 2017.

[6] S. Huang, M. Cao, Y. Xia, X. Chen, and M. Yang, "Heat and mass transfer characteristics of steam in a horizontal wellbore with multi-point injection technique considering wellbore stock liquid," *International Journal of Heat & Mass Transfer*, vol. 127, pp. 949–958, 2018.

[7] S. F. Xue, H. J. Wang, and G. L. Zhu, "Improved calculation model of suction profile of horizontal well," *Special Oil and Gas Reservoirs*, vol. 15, no. 5, pp. 94–97, 2008.

[8] X. Feng, J. Qinghui, X. Chaoshui, and Z. Xiaobo, "Influences of connectivity and conductivity on nonlinear flow behaviours through three-dimension discrete fracture networks," *Computers and Geotechnics*, vol. 107, pp. 128–141, 2019.

[9] F. Sun, Y. Yao, and G. Li, "Comments on heat and mass transfer characteristics of steam in a horizontal wellbore with multi-point injection technique considering wellbore stock liquid [International Journal of Heat and Mass Transfer 127 (2018) 949-958]," *International Journal of Heat & Mass Transfer*, vol. 132, pp. 1319–1321, 2019.

[10] C. Zhu, X. D. Xu, X. T. Wang et al., "Experimental investigation on nonlinear flow anisotropy behavior in fracture media," *Geofluids*, vol. 2019, Article ID 5874849, 9 pages, 2019.

[11] S. Mozaffari, M. Nikookar, M. R. Ehsani, L. Sahranavard, E. Roayaie, and A. H. Mohammadi, "Numerical modeling of steam injection in heavy oil reservoirs," *Fuel*, vol. 112, pp. 185–192, 2013.

[12] M. R. Chesney, F. Felten, H. S. Hallibuton, and J. Edlebeck, "Design, testing, and field performance of steam-injection flow-control devices for use in SAGD oil recovery," in *SPE Canada heavy oil technical conference*, OnePetro, 2015.

[13] X. P. Liu, Z. S. Zhang, and X. E. Liu, "Simulation model of flow pressure drop coupled with seepage in horizontal wellbore," *Journal of Southwest Petroleum Insitute*, vol. 22, no. 2, pp. 36–39, 2000.

[14] S. Huang, Y. Xia, H. Xiong, H. Liu, and X. Chen, "A three-dimensional approach to model steam chamber expansion and production performance of SAGD process," *International Journal of Heat and Mass Transfer*, vol. 127, no. Part A, pp. 29–38, 2018.

[15] C. Zhu, Y. Lin, and G. Feng, "Influence of temperature on quantification of meso-cracks: implications for physical properties of fine-grained granite," *Lithosphere*, vol. 2021, no. - Special 4, Article ID 7824057, 2021.

[16] C. S. Guo, F. Y. Qu, Y. Liu, J. R. Niu, and Y. Zou, "Simulation of steam injection process for horizontal well with heavy oil recovery," *Heat Transfer Engineering*, vol. 39, no. 13-14, pp. 1283–1295, 2017.

[17] X. F. Ni, S. L. Cheng, C. L. Li, and J. Q. An, "A new model for calculating parameters in steam injection well," *Chinese Journal of Computational Physics*, vol. 22, no. 3, pp. 251–255, 2005.

[18] C. Temizel, C. H. Canbaz, Y. Palabiyik, M. Irani, K. Balaji, and R. Ranjith, "Production optimization through intelligent wells in steam trapping in SAGD operations," in *SPE Western Regional Meeting*, OnePetro, 2019.

[19] Y. Qian, L. Richeng, J. Hongwen, S. Haijian, L. Yu, and L. He, "Experimental study of nonlinear flow behaviors through fractured rock samples after high-temperature exposure," *Rock Mechanics and Rock Engineering*, vol. 52, no. 9, pp. 2963–2983, 2019.

[20] Z. Fan, C. He, and A. Xu, "Calculation model for on-way parameters of horizontal wellbore in the superheated steam injection," *Petroleum Exploration and Development*, vol. 43, no. 5, pp. 798–805, 2016.

[21] M. C. He, Q. Sui, M. Li et al., "Compensation excavation method control for large deformation disaster of mountain soft rock tunnel," *International Journal of Mining Science and Technology*, vol. 32, no. 5, pp. 951–963, 2022.

[22] H. Gu, L. Cheng, S. Huang, B. Bo, Y. Zhou, and Z. Xu, "Thermophysical properties estimation and performance analysis of superheated-steam injection in horizontal wells considering phase change," *Energy Conversion & Management*, vol. 99, pp. 119–131, 2015.

[23] Y. Qian, J. Hongwen, L. Richeng, L. Yu, S. Haijian, and H. Guansheng, "Pore characteristics and nonlinear flow behaviors of granite exposed to high temperature," *Bulletin of Engineering Geology and the Environment*, vol. 79, no. 3, pp. 1239–1257, 2020.

[24] A. Z. Xu, Z. F. Fan, L. He, X. Xue, and B. Bo, "Optimization of superheated steam huff and puff wells sequence in heavy oil reservoir," *Applied Mechanics & Materials*, vol. 295, pp. 3154–3157, 2013.

[25] C. He, A. Xu, Z. Fan et al., "An integrated heat efficiency model for superheated steam injection in heavy oil reservoirs," *Oil & Gas Science and Technology*, vol. 74, no. 2, p. 7, 2019.

[26] P. Li, Y. Zhang, X. Sun, H. Chen, and Y. Liu, "A numerical model for investigating the steam conformance along the dual-string horizontal wells in SAGD operations," *Energies*, vol. 13, no. 15, p. 3981, 2020.

[27] M. Li, H. Chen, Y. Zhang, W. Li, Y. Wang, and M. Yu, "A coupled reservoir/wellbore model to simulate the steam injection performance of horizontal wells," *Energy Technology*, vol. 3, no. 5, pp. 535–542, 2015.

[28] S. F. Kaslusky and K. S. Udell, "A theoretical model of air and steam co-injection to prevent the downward migration of DNAPLs during steam-enhanced extraction," *Journal of Contaminant Hydrology*, vol. 55, no. 3-4, pp. 213–232, 2002.

[29] I. D. Gates and N. Chakrabarty, "Optimization of steam assisted gravity drainage in McMurray reservoir," *Journal of Canadian Petroleum Technology*, vol. 45, no. 9, pp. 54–62, 2006.

[30] L. I. Xiuluan, L. I. Hao, L. U. Jian, J. Hang, and W. Hongzhuang, "3D physical simulation on dual horizontal well SAGD in heterogeneous reservoir," *Shiyou Xuebao/Acta Petrol Sinica*, vol. 35, no. 3, pp. 536–542, 2014.

[31] Y. Qian, J. Wu, C. Zhu, Q. Wang, and X. Jinyong, "The role of multiple heating and water cooling cycles on physical and mechanical responses of granite rocks," *Geomechanics and Geophysics for Geo-Energy and Geo-Resources*, vol. 7, no. 3, p. 69, 2021.

[32] M. Desheng, J. Guo, C. Zan, H. Wang, and L. Shi, "Physical simulation of improving the uniformity of steam chamber growth in the steam assisted gravity drainage," *Petroleum Exploration & Development*, vol. 40, no. 2, pp. 202–207, 2013.

[33] M. Dong, F. Zhang, J. Lv, M. Hu, and Z. Li, "Study on deformation and failure law of soft-hard rock interbedding toppling slope base on similar test," *Bulletin of Engineering Geology and the Environment*, vol. 79, no. 9, pp. 4625–4637, 2020.

[34] D. Ren, X. Wang, Z. Kou et al., "Feasibility evaluation of CO2 EOR and storage in tight oil reservoirs: a demonstration project in the Ordos Basin," *Fuel*, vol. 331, article 125652, 2023.

[35] Q. Wang, M. C. He, S. C. Li et al., "Comparative study of model tests on automatically formed roadway and gob-side entry driving in deep coal mines," *International Journal of Mining Science and Technology*, vol. 31, no. 4, pp. 591–601, 2021.

Hindawi
Geofluids
Volume 2023, Article ID 1758153, 14 pages
https://doi.org/10.1155/2023/1758153

Research Article

Numerical Simulation of Diversion Tunnel Excavation Using GPU-Accelerated Anisotropic Random Fields

Guo-jin Zhu,[1,2] Yu Ning,[2] Zhi-hao Cui,[3] Nanxiang Hu,[4] Qing-xiang Meng,[1,2] and Chun Zhu[4]

[1]*Research Institute of Geotechnical Engineering, Hohai University, Nanjing 210098, China*
[2]*Kunming Engineering Co. Ltd., Power Construction Corporation, Kunming 650051, China*
[3]*Shanghai Investigation, Design & Research Institute Corporation, Shanghai 200335, China*
[4]*School of Earth Sciences and Engineering, Hohai University, Nanjing 210098, China*

Correspondence should be addressed to Zhi-hao Cui; cui_zhihao@ctg.com.cn and Qing-xiang Meng; mqx@hhu.edu.cn

Received 17 October 2022; Revised 17 December 2022; Accepted 18 March 2023; Published 18 April 2023

Academic Editor: Mohammed Fattah

In this study, a combined anisotropic random field and GPU-accelerated Cholesky decomposition algorithm is proposed for diversion tunnel excavation. With the MATLAB programming control be used to combine the advantages of GPU and CPU computing, the efficient method of generating large numerical model random fields is realized. Based on the geological structure characteristics of red-layered soft rocks in central Yunnan, the anisotropic rock random field and tunnel excavation with different rotation angles are simulated. The results show that the variability of rotational anisotropy random fields and mechanical parameters of the red-bedded soft rocks in central Yunnan has a large influence on the deformation and stress state of the surrounding rocks at the excavation face of the tunnel. This study can provide theoretical and technical support for the design and construction of relevant rock engineering in the red-layered soft rock area in central Yunnan.

1. Introduction

With the rapid improvement of engineering construction level in China, the development and utilization of underground space are becoming more and more extensive, and the related engineering problems are gradually increasing [1, 2]. The surrounding rock body of a tunnel or underground chamber is a geological material with typical nonhomogeneous characteristics. However, in the traditional geotechnical engineering analysis, the rock is mostly assumed to be a continuous medium with homogeneous properties. This simplified treatment cannot consider the randomness and spatial variability of the actual engineering rock mechanical parameters [3, 4]. In the engineering design stage, due to the lack of profound understanding of the spatial variability of rock geological materials, engineers often cannot anticipate the potential hazards in underground engineering well. Therefore, how to analyze and evaluate the randomness of rock parameters reasonably is of great significance to the stability analysis of underground cavern engineering [4–7].

At this stage, there are three main methods for the stochastic analysis of mechanical parameters of geological materials. One is to consider the interval distribution of parameters in the calculation process, such as interval finite element [8, 9] and fuzzy finite element methods [10, 11]. These methods can input interval parameters directly and obtain a simulation result in a certain interval range by calculation. However, these methods are difficult to deal with the intrinsic model of nonlinear materials [12]. The second method is the mesoscale modeling of the heterogeneous media based on the statistical property of the microstructure [13–19]. However, the analysis scale of this solution is not big enough for the large-scale geotechnic engineering.

The other approach is to characterize the spatial variability of the geological structural properties of the cavern envelope using random field theory [20]. Beacher and Ingra

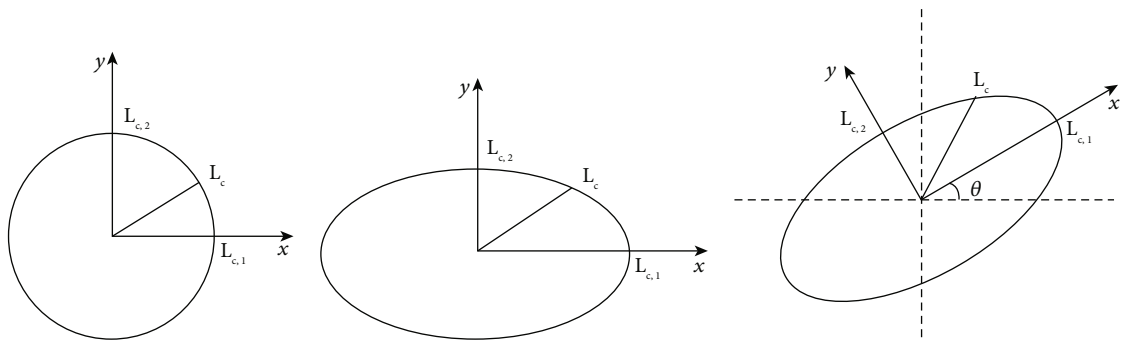

(a) Isotropic (b) Horizontal anisotropy (c) Rotational anisotropy

Figure 1: Correlation structure diagram of anisotropic random fields.

chose the Taylor expansion of the stochastic finite element method to analyze the reliability of ground settlement [21]. Vanmarcke and Grigoriu made pioneering work in the field of soil property parameters [22]. Suchomel and Mašín considered the spatial variable cohesion (c) and friction angle (φ) of soil mechanical parameters to compare probabilistic methods for assessing slope stability and discussed the influence of parameters' spatial variability on slope stability [23]. Li et al. proposed a new stochastic finite element method for analyzing slope reliability based on the consideration of spatial variability of slope soil coefficients, which improved the computational efficiency of slope reliability analysis [24]. The effect of spatial variability of infiltration parameters on slope stability was analyzed by Griffiths and Lane [25]. Cho [26] used random field theory to assess slope stability. Jiang et al. [27] conducted random field simulation of geological materials based on the Cholesky decomposition and investigated the effect of different autocorrelation functions on the reliability of slopes.

Based on the literature above, it is evident that the random field method is capable of describing the spatial variability of geotechnical material parameters more accurately. The random field method can be easily implemented in commercial or open-source programs. At present, the random field method for geotechnical materials is mainly applied to the stability analysis of slopes [28]. Less research has been done in the stability analysis of excavation in underground caverns or tunnels.

In this study, the modeling theory of anisotropic random field is optimized and an efficient generation algorithm for random field of underground caverns is developed. Due to a large number of model meshes, the covariance matrix decomposition method may exist the problem of slow computation. Based on the Cholesky decomposition theory and GPU acceleration technology, an efficient random field generation technique with GPU acceleration is proposed. An automated control calculation program was written using MATLAB. With the consideration of the geological structure characteristics of red-layered soft rocks in central Yunnan, an anisotropic rock random field model with different rotation angles was established to analyze the deformation and stress distribution state of the tunnel after excavation in central Yunnan. The influence of the randomness of the surrounding rock parameters on the secondary stress state of the surrounding rock was studied.

2. Methodology

2.1. Isotropic Random Field. There are methods to generate random fields. Currently, two main types of random field generation methods are commonly used [29]. In this study, a generator of spatially correlated random variables is combined with a discretization method to compute, for each node in the random field grid, a random variable that is correlated with other nodes in the random field. These spatially correlated random variables are assigned to a cell or integration point in the finite element model. The random field is generated by a combination of the covariance matrix decomposition method and the midpoint method. Using the covariance matrix decomposition method, a set of correlated random variables can be generated as follows:

$$z_c(x) = L\chi, \tag{1}$$

where $z_c(x)$ is a vector that contains spatially correlated random variables, χ is the independent zero-mean vector representing the unit variance, normally distributed random variables, and L is the Cholesky decomposition of the correlation matrix.

Therefore, the calculation of the correlation matrix is the key to this method. After loading the grid file to obtain the node coordinates, the correlation coefficient matrix R_{ij} for a set of N random variables collected in the vector y is defined as

$$\begin{aligned} R_{ij} &= \frac{\mathrm{Cov}\left(y_i, y_j\right)}{\sqrt{\mathrm{Var}(y_i)\mathrm{Var}\left(y_j\right)}} \\ &= \begin{bmatrix} 1 & \rho(y_1, y_2) & \cdots & \rho(y_1, y_n) \\ & 1 & & \rho(y_2, y_n) \\ & & \ddots & \vdots \\ \text{symmetric} & & & 1 \end{bmatrix}, \end{aligned} \tag{2}$$

where $\rho(y_i, y_j)$ is the correlation coefficient of y_i and y_j.

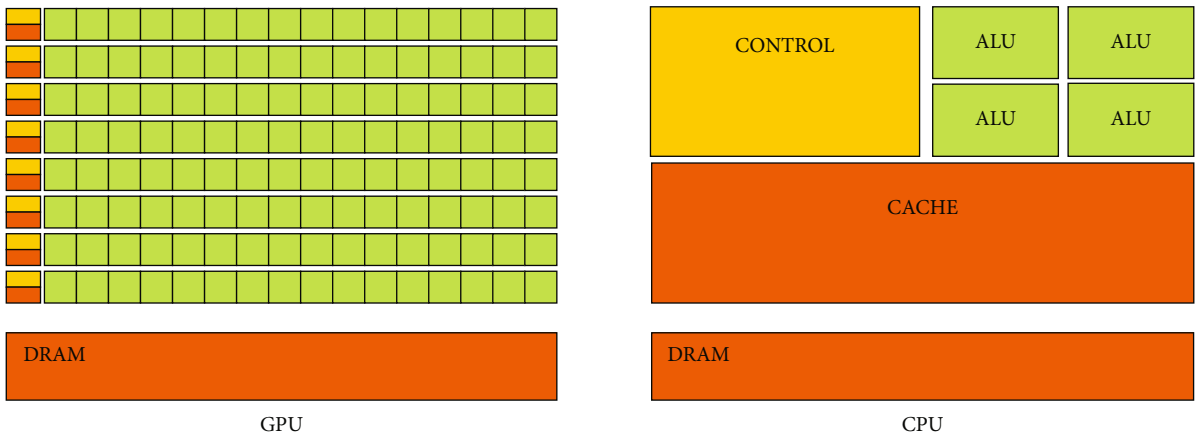

Figure 2: Schematic of GPU and CPU hardware architecture.

Table 1: Comparison of computing time of different computing schemes.

Array size		100	500	1000	2000	5000	8000	10000
Calculation time (s)	CPU	0.0021	0.0072	0.0258	0.1444	1.5374	10.7636	24.7266
	GPU	0.0138	0.0337	0.0565	0.1432	1.0668	2.5609	4.0514

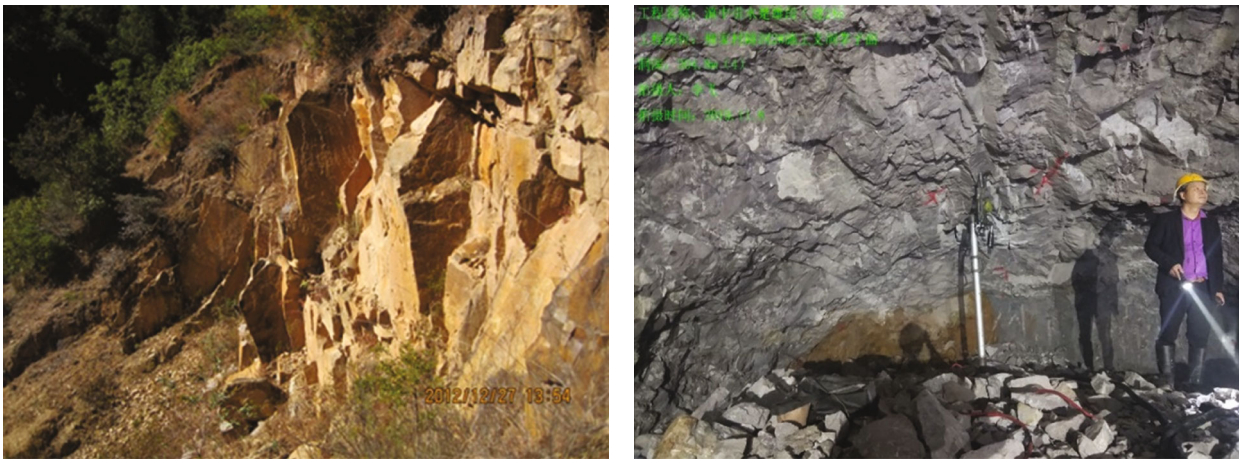

(a) Field rock survey (b) In-tunnel survey

Figure 3: No mudstone-type stratigraphic structure.

The correlation matrix is symmetric and positive definite, and the correlation coefficient matrix R_{ij} is decomposed into upper triangular matrix and lower triangular matrix by the Cholesky decomposition:

$$R = LL^T. \tag{3}$$

Currently, there are two main types of correlation functions, namely, exponential correlation functions (Exp) and squared exponential (SExp) correlation functions, as follows:

$$\text{Exp}: \rho(\Delta x_1, \Delta x_2) = c_1 + (1 - c_1) \exp\left(-\sqrt{\left(\frac{\Delta x_1}{L_{c,1}}\right)^2 + \left(\frac{\Delta x_2}{L_{c,2}}\right)^2}\right), \tag{4}$$

$$\text{SExp}: \rho(\Delta x_1, \Delta x_2) = c_1 + (1 - c_1) \exp \cdot \left[-\left(\left(\frac{\Delta x_1}{L_{c,1}}\right)^2 + \left(\frac{\Delta x_2}{L_{c,2}}\right)^2\right)\right], \tag{5}$$

where c_1 is the threshold value of the correlation function and $L_{c,1}$ and $L_{c,2}$ are the correlation lengths.

The correlation coefficient matrix is a symmetric matrix R_{ij} that can be obtained by a two-dimensional correlation function [30]. After obtaining the correlation matrix, it can be decomposed using the Cholesky decomposition method. When the SExp correlation function is chosen and the number of nodes is larger than the correlation length, the correlation matrix is nonpositive; i.e., all the eigenvalues of

(a) Muddy siltstone with mudstone (b) Calcareous siltstone with mudstone

Figure 4: Intercalated mudstone-type stratigraphic structure.

(a) Interbedded calcareous mudstone and calcareous siltstone (b) Interbedded siltstone and calcareous siltstone

Figure 5: Interstratification type stratigraphic structure.

(a) Field rock survey (b) In-tunnel survey

Figure 6: All-mudstone-type stratigraphic structure.

the matrix are no longer positive. In this case, it needs to be corrected. In the modified Cholesky decomposition algorithm, the parameters less than the tolerance value are set to zero to obtain stable results. This algorithm gives an "approximate" Cholesky decomposition. After the decomposition of the correlation matrix, the eigenvalues and eigenvectors are obtained. The decomposition of the correlation matrix is obtained according to

$$L = A \times \sqrt{\lambda}, \tag{6}$$

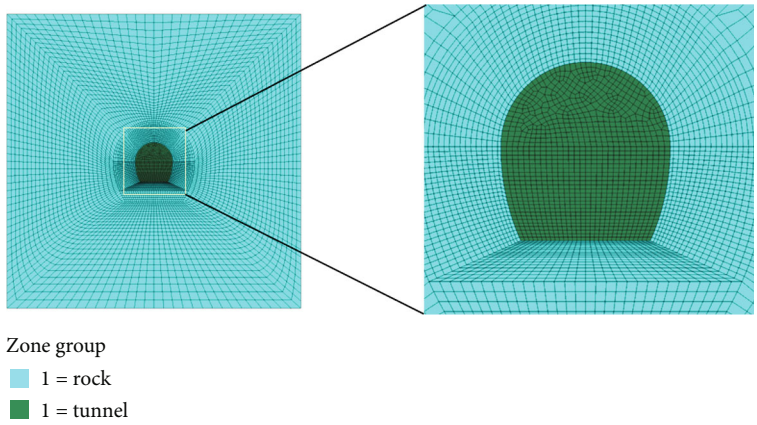

Figure 7: Meshed model and local enlarged figure of water diversion tunnel excavation simulation.

Table 2: Suggested values of random field parameters for red layer excavation tunnels in central Yunnan.

Threshold of correlation function	Cohesion c (MPa)	Friction angle φ (°)	Young's modulus (GPa)	Poisson's ratio	Density (kg/m^3)	Geostress (MPa)
0.5	0.1-0.4	25-35	20	0.25	2500	14.5

where A is the matrix containing the eigenvectors and λ is the diagonal matrix containing the eigenvalues.

Based on the derivation above, the calculation of random field CRV (correlated random variables) can be finally established as shown in

$$\mathrm{CRV} = \mu + L \times \mathrm{RV} \times \sigma, \tag{7}$$

where μ is the standard normal distribution mean, σ is the standard deviation of the standard normal distribution, and RV is the standard normal distribution random quantity.

2.2. Anisotropic Random Field. In order to study the modeling theory of anisotropic random fields in geotechnical bodies, it is necessary to recall the definition of correlation length. According to Equations (4) and (5), the value of correlation length is equal to the integration of the correlation function over the full domain. The phase correlation length is the key to measure the spatial variability of geological materials. The difference of its length in different orientations determines the anisotropic characteristics of the random field. The structural characteristics of the random field can be characterized by the correlation length contour. The points in space with the same coefficients associated with the center of the circle are connected to form the correlation length contour, as shown in Figure 1.

$L_{c,1}$ and $L_{c,2}$ denote the correlation lengths along the main directions of the two coordinate axes. L_c is the correlation length in a direction in coordinate space. θ is the rotation angle of the coordinate axes with respect to the horizontal datum. It follows that when the correlation lengths along the principal directions of the two coordinate axes are different, the contour changes from an isotropic circle to an ellipse. This describes the random field with horizontal anisotropy characteristics. When the axes are rotated by an angle θ based on the horizontal line, the length of the projection on the axes also changes. This situation characterizes the random field with rotational anisotropy.

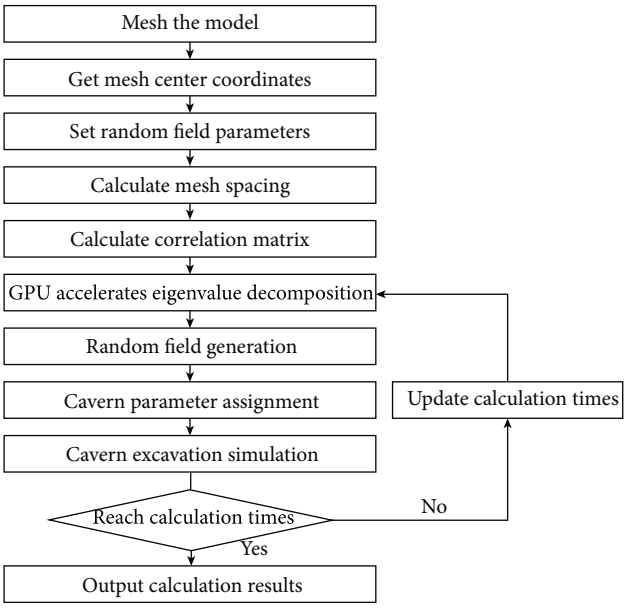

Figure 8: Flow chart of the excavation analysis of the water diversion tunnel in central Yunnan based on the random field theory.

If the anisotropy of rocks is going to be characterized by random fields, suitable modifications according to the definition of random field generation have to be made. In combination with the random field theory described above, this study proposes a method for generating random fields applicable to the anisotropy of rock materials. Along a

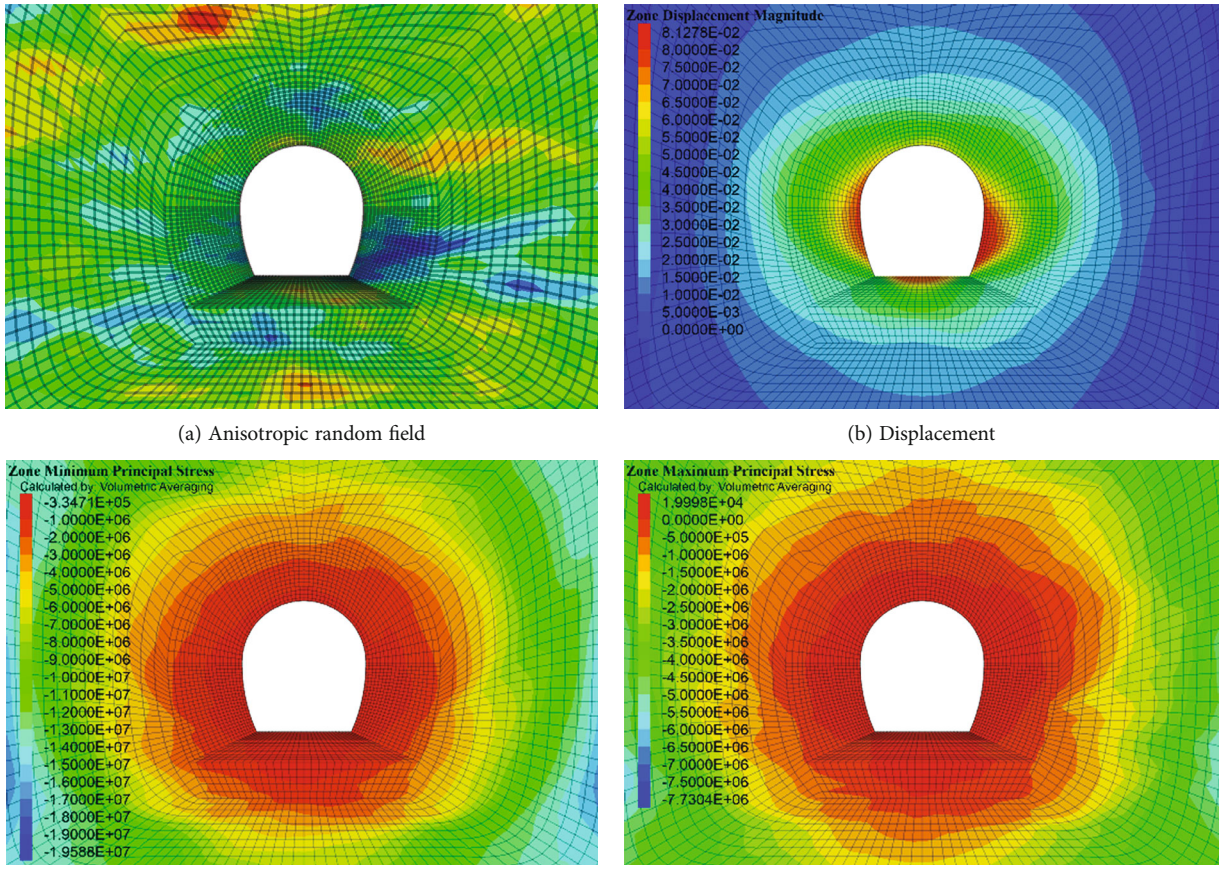

(a) Anisotropic random field

(b) Displacement

(c) Major principal stress

(d) Minor principal stress

Figure 9: Analysis of cavern excavation results with 0° anisotropic field.

certain principal axis direction where anisotropic characteristics need to be reflected, the correlation length of that direction is appropriately increased. For example, for the horizontal anisotropy shown in Figure 1(b), the desired anisotropic random field can be obtained by increasing the correlation length of the axial direction. In contrast, the rotational anisotropy shown in Figure 1(c) is not along the principal axis direction. Based on Equations (8) and (9), the new modification Δx_1 and Δx_2 of the correlation length projection along the X-direction and Y-direction can be obtained by changing the angle θ of the reference coordinate, instead of taking the standard coordinate axis as reference. Taking the exponential correlation function as an example, the random field of rotational anisotropy can be obtained by rotating counterclockwise.

$$\Delta x_1 = \Delta x \cos\theta + \Delta y \sin\theta, \tag{8}$$

$$\Delta x_2 = \Delta y \cos\theta - \Delta x \sin\theta. \tag{9}$$

2.3. Anisotropic Random Field Simulation Based on GPU Acceleration. Hardware acceleration refers to that in the process of scientific computing; due to the excessive amount of data to be computed, the computer assigns computational tasks exclusively to a specific piece of hardware to process, reducing the load on the core processor and thus improving computational efficiency. Hardware acceleration technology, widely used in image processing, is commonly known as the graphics processing unit (GPU). Before the advent of the GPU, the CPU had been responsible for a large amount of data processing tasks in the computer. In terms of design thinking, CPUs are suited to complete a single task as fast as possible, usually a line of computation from start to finish. Multimedia data processing is a task that computers are often faced with and usually requires computer hardware that can provide great computational density and efficient parallel computing. In fact, CPUs have difficulty in meeting their huge multimedia data processing requirements in their hardware itself. Software optimization alone could not deal with this problem, until the advent of GPUs.

GPUs are tasked with composing and displaying images of millions of pixels on the screen, requiring parallel processing of millions of tasks. CPUs and GPUs differ greatly in architecture, as illustrated in Figure 2. It can be seen that the GPU has more logical algorithm units (ALUs) and is also multithreaded and parallel, without excessive control and storage functions. Therefore, GPUs have super high computational efficiency and good processing power for dense and large amount of data and complex algorithms. However, the CPU needs to control the whole computation process and

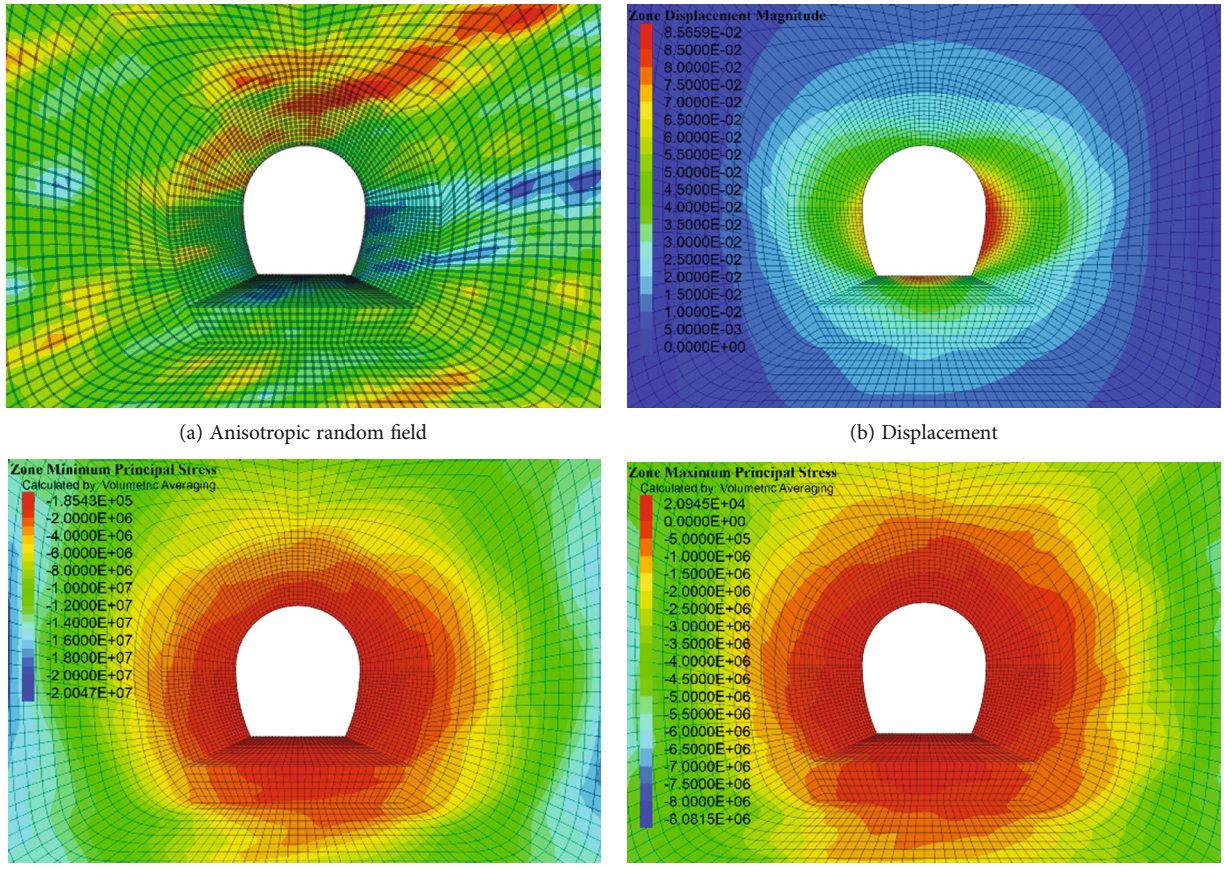

(a) Anisotropic random field

(b) Displacement

(c) Major principal stress

(d) Minor principal stress

Figure 10: Analysis of cavern excavation results with 15° anisotropic field.

store the data at the same time, and it has a small number of logical operation units and can only process one data line in one time period, which is inefficient for large and complex array computation.

CUDA is a general-purpose parallel computing architecture introduced by NVIDIA that contains calling instructions and a GPU computing engine that enables the GPU to solve complex computational problems. Program code developed based on CUDA separates out the complex array processing part of the entire computational processing flow and calls the GPU to accelerate it. Each discrete block of computational requirements is further subdivided into a new set of instructions. Finally, all of the subdivided computational tasks are executed simultaneously on the GPU processor. This is the principle of efficient parallel computing GPU hardware acceleration.

The traditional method of improving Cholesky decomposition to generate random fields is good, but the computational efficiency is very low and there are few practical applications. In order to put the random field generated by this method into practical application, the random field generation efficiency needs to be improved significantly. In the random field generation method proposed in this study, the decomposition of the correlation matrix is calculated using MATLAB programming. Among them, the modified Cholesky decomposition can be found in MATLAB with the corresponding eigenvalue decomposition operation, while in the case of larger and more complex models with more coordinate data. The correlation matrix array generated by the length of the coordinate data is huge. The decomposition process of the correlation matrix array is extremely time-consuming. The cycle efficiency of simulation calculation is seriously affected. To address this difficulty, this study uses GPU acceleration technology to improve the simulation efficiency.

In the key step of correlation matrix decomposition, the efficiency of GPU parallel computation increases significantly when the matrix size gradually increases, and the efficiency of cyclic simulation increases dramatically. However, the entire process of correlation matrix decomposition remains in the hands of the CPU. In the 2D random field simulations carried out in this study, MATLAB was used for the conversion of the simple code. When proceeding the modified Cholesky decomposition, the *gpuArray* command is called to load the relevant matrix into the GPU. After completing the decomposition of the correlation matrix with efficient parallel operations in the GPU, the required eigenvector matrix and eigenvalue matrix are called back to the CPU for the next computation by the *gather* command. Table 1 compares the decomposition of the correlation matrix with different sizes when computers with CPU and GPU computation schemes are used, respectively.

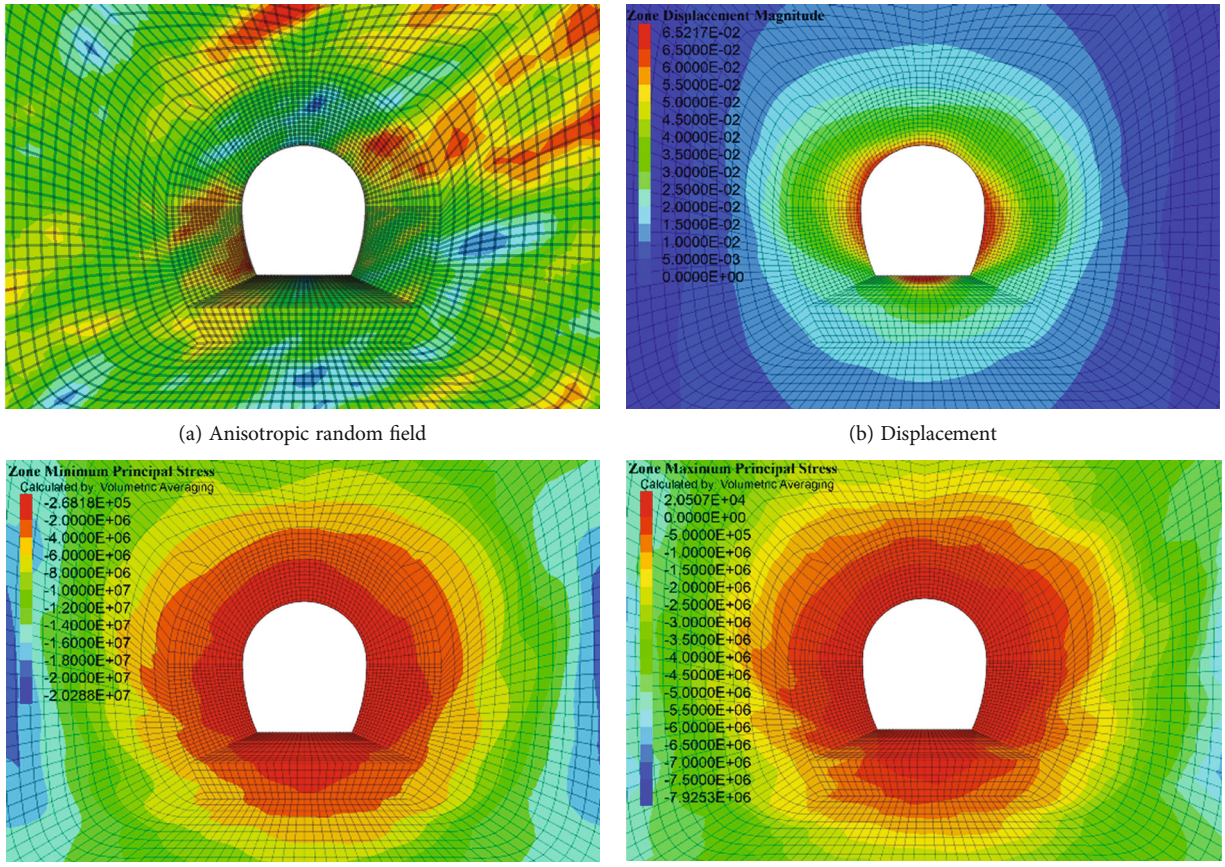

(a) Anisotropic random field

(b) Displacement

(c) Major principal stress

(d) Minor principal stress

Figure 11: Analysis of cavern excavation results with 30° anisotropic field.

As can be seen, the advantage of GPU acceleration gradually emerges as the array of operational matrices becomes larger, and its computational speed is much faster than that of the CPU, which saves a lot of time when doing multiple round-robin operations to compute probability problems.

3. Simulation of the Red Layer in Central Yunnan

3.1. Geological Background. The tectonics of rock stratum in soft rock body refers to the spatial distribution and arrangement among the sedimentary layers in the rock stratum. For example, the thick-layered block-thin laminated structure rock body refers to the sandwich-like and interlayer-like structures of the spatial combination arrangement of each stratigraphic rock unit (which can be divided according to lithology, layer thickness, etc.). It can be seen that the original rock stratigraphic structure of the weak geotechnical body is closely related to the engineering rock structure type.

In this study, the stratigraphic structure characteristics of the red-layered weak rock body in the Chuxiong section of the Yunnan Central Water Diversion Project are analyzed as an example. Through on-site engineering geological investigation and geological data analysis, the spatial variation law of the geological structure of the red-layered soft rock is analyzed. In this study, the mudstone content and the spatial distribution and arrangement of other rock layers were selected as the analysis index. Based on this, the red-bedded soft rock stratigraphy was classified as mudstone-free type, interbedded mudstone type, interbedded type, mudstone-dominated type, and all-mudstone type. Obviously, the mud content of the rock strata of different tectonic types in the above order is gradually increasing. In a sense, the engineering geological properties of the red-bedded soft rocks will gradually diminish.

Figure 3 shows the mud-free type of chondrites, which is characterized by a rather heterogeneous spatial distribution of strata. The distribution of different rocks is random and loose, and there is no prominent anisotropy in a certain spatial direction. The main rocks are gravels, and the corresponding random field model can be considered an isotropic random field.

Figure 4 shows the structure of the intercalated mudstone-type stratigraphy, which shows the intercalation of soft mudstone layers between hard sandstone layers. There is obvious anisotropy in specific spatial directions and spatial variability along the strike of the interbedded layers. The anisotropic random field model can be used to simulate this type of interbedded mudstone formation.

Figure 5 shows the anisotropic characteristics of the spatial structure of interstratified strata. In the red layer region of central Yunnan, the interstratified strata are mainly

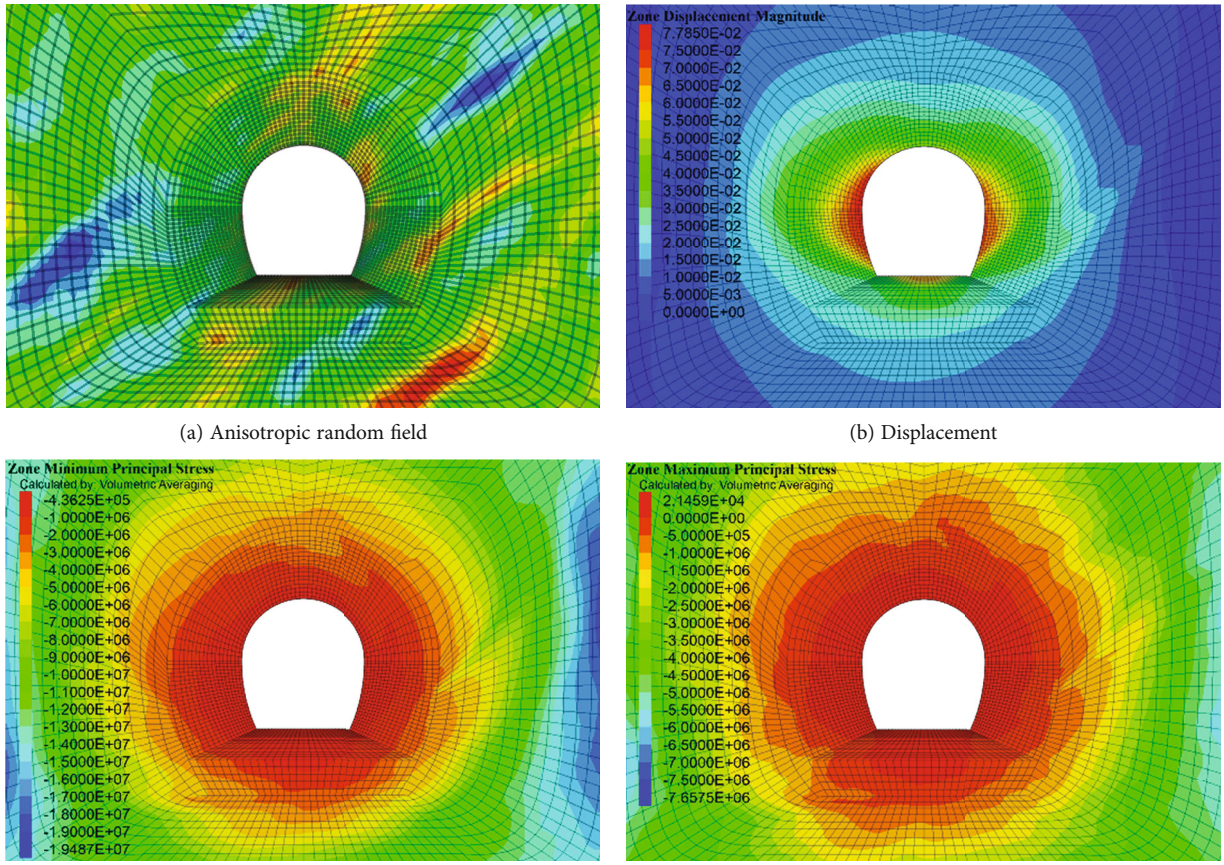

(a) Anisotropic random field

(b) Displacement

(c) Major principal stress

(d) Minor principal stress

Figure 12: Analysis of cavern excavation results with 45° anisotropic field.

quartz sandstone, calcareous siltstone, and calcareous mudstone and siltstone layered with each other, forming a spatial structure of one layer of different rock-soil bodies. In the spatial direction, the variation of interstratified strata is obvious, and the anisotropic random field is applicable to describe their geological and structural characteristics.

Figure 6 shows the geological and tectonic features of the all-mudstone-type red layer. The rock types of the all-mudstone red layer are mainly calcareous and siltstone mudstone. In terms of geological structure, there is no obvious anisotropic feature in the all-mudstone red layer. However, because of the large content of soft rocks, the deformation of the all-mudstone red layer is larger under the excavation and unloading conditions. Therefore, its engineering risk should be considered as a key issue.

3.2. Modeling and Analysis Process for Red-Layered Soft Rock Tunnels in Central Yunnan. In the water diversion project in central Yunnan, a section of horseshoe-shaped hydraulic tunnel was selected for the study. The burial depth of this section of hydraulic tunnel is about 600 m, and the surface topography is gently sloping. The numerical model is shown in Figure 7. The model has a length of 80 m, a height of 80 m, a bottom wall of 8.72 m, and a height of 9.43 m. The rock and tunnel areas are divided in the model, and a hexahedral structured mesh is used to divide the model mesh. The number of meshes in this numerical model is 7225, and the number of nodes is 14594.

This section of hydraulic tunnel is in the softly interbedded cavern section of the Lion Rock tuff. The initial ground stress in this section of the hydraulic tunnel can be found by the depth of burial and the weight of the rock mass. The fluctuation value of the cohesion c of the rock strength parameter is suggested to be between 0.1 and 0.4 MPa, and the fluctuation value of the internal friction angle φ is suggested to be between 25 and 35 degrees. The site engineering geological survey report provides suggested values for other rock mechanics parameters, as shown in Table 2.

Based on the random field theory, the hydraulic tunnel excavation simulation requires a preassigned model. According to the working conditions, a numerical model of the tunnel excavation area as well as the surrounding rock is established with the grid be divided. The preprocessing of the dissected mesh is done by a written program. The coordinates of the grid centroids are exported, and the coordinate matrix is generated in MATLAB. Then, the correlation matrix is generated from the coordinate matrix, and the random field matrix is generated using the covariance matrix decomposition method. Based on the Mohr-Coulomb principal structure model, the attributes to be assigned are selected and the coefficient-based equations are obtained using quadratic curve fitting. The random field matrix is substituted

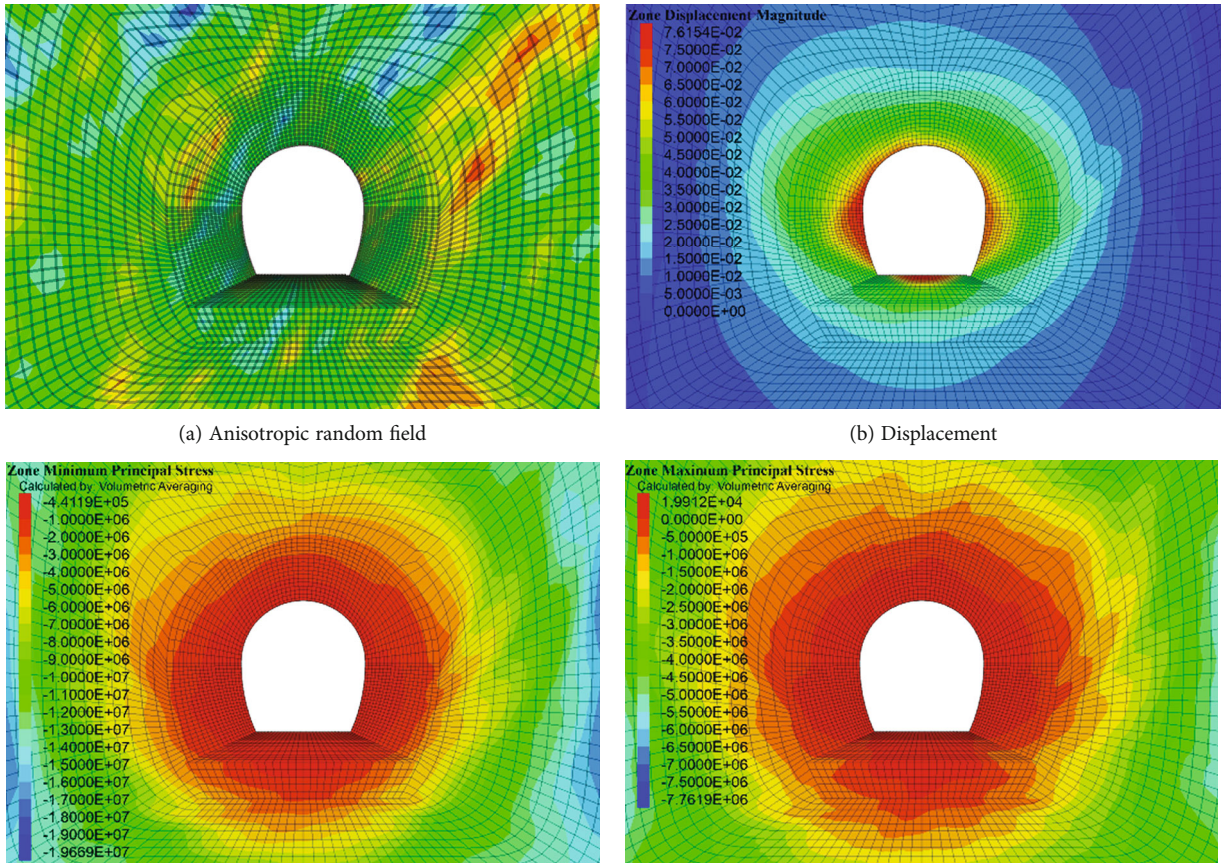

(a) Anisotropic random field

(b) Displacement

(c) Maximum principal stress

(d) Minimum principal stress

Figure 13: Analysis of cavern excavation results with 60° anisotropic field.

through code programming control to generate an initial random assigned model of the cavity based on random field theory. Numerical simulation analysis is performed on the produced numerical model. The maximum displacement of the surrounding rock in the excavation area of the hydraulic tunnel and the corresponding coordinate positions are recorded for a variety of random field conditions. The whole process can be accomplished by executing operating system commands with MATLAB. The specific flow chart is shown in Figure 8.

4. Study on the Influence Law of Anisotropy with Field

4.1. Computing Conditions. To simplify the analysis, this study assumes that the tunnel excavation is completed in one go. When the numerical simulation of cavern excavation is implemented in FLAC software, if the material properties of the rock mass in the tunnel excavation area are directly changed to null, it may cause a sharp release of ground stress, resulting in instantaneous collapse of the cavern. In order to reflect the progressive excavation process of the tunnel, the elastic modulus of the rock body in the excavation area of the cavern chamber can be reduced to 5% of the initial one by gradual weakening. Then, the material properties are changed to null, and the numerical simulation of the tunnel excavation process is finally completed. By the method above, the excavation numerical simulation of anisotropic random field cavern chamber with different rotation angles is done. The simulation results are analyzed as follows.

4.2. Simulation Results and Analysis. Figure 9(a) shows the enlarged view of the local model when the random field is horizontally anisotropic. After the excavation, the deformation results of the cavern are shown in Figure 9(b). It can be seen that the deformation of the right side wall of this hydraulic tunnel is larger than that of the left side wall under the condition of horizontal anisotropic random field. The maximum deformation is 81.3 mm, which is located in the middle of the right side wall, about 3.6 m from the bottom edge. The random field parameter at this location is the minimum value of the cavern envelope. The main stress distribution of the cavern chamber is shown in Figures 9(c) and 9(d). Due to the excavation, a significant ground stress release was generated in the critical area of the tunnel envelope. The major principal stress decreased from an initial 14.50 MPa to 0.34 MPa. The minor principal stress decreased from 14.50 MPa (compressive stress) to a tensile stress of 0.02 MPa. Due to the variability of mechanical parameters caused by the rock random field, the stresses in the cavern envelope exhibit an asymmetric distribution. However, the general distribution pattern is similar. The

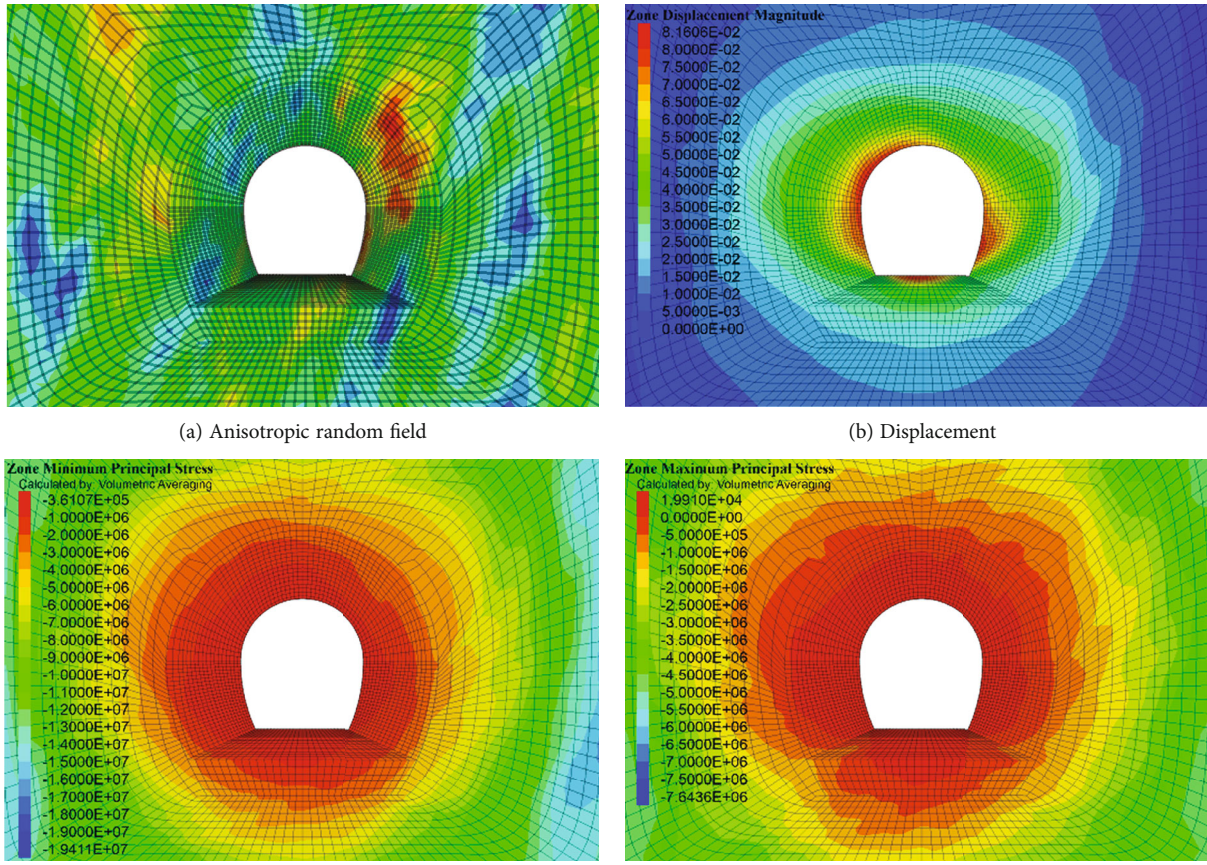

(a) Anisotropic random field

(b) Displacement

(c) Major principal stress

(d) Minor principal stress

Figure 14: Analysis of cavern excavation results with 75° anisotropic field.

further away from the tunnel excavation critical surface, the less the stress release and shows an irregular circular divergence.

An enlarged local model of the anisotropic random field with 15 degrees of rotation is shown in Figure 10(a). After the end of excavation, the deformation of the tunnel is shown in Figure 10(b). It can be seen that in the anisotropic random field with 15 degrees of rotation, the deformation of the tunnel surrounding rock shows a phenomenon of large right and small left. The maximum deformation is 85.7 m, which is located in the middle of the right side wall, about 4 m from the bottom edge. A strip of rock with weak parameters is distributed at this location. The main stress distribution of the cavern is shown in Figures 10(c) and 10(d). It can be seen that the surrounding rock of the tunnel has a significant stress release due to excavation. The major principal stress decreases from 14.50 MPa to 0.19 MPa, and the minor principal stress decreases from 14.50 MPa in compression to 0.02 MPa in tension, while the stress distribution around the chamber is asymmetric due to the randomness of the mechanical parameters. The values of the random mechanical parameters of the rock mass in the direction to the left of the vault are larger. Therefore, the large principal stress release in the internal surrounding rock at this location is not very obvious compared with that in the surrounding rock at other locations.

The local model enlargement of the anisotropic random field with 30 degrees of rotation is shown in Figure 11(a). After the end of excavation, the cavern excavation deformation is shown in Figure 11(b). In general, it shows a large deformation of the right side wall and a small deformation of the left side wall. The direction of the most value of displacement is orthogonal to the direction of random field anisotropy. The maximum deformation is 65.2 mm, which occurs in the middle of the sidewall. The mechanical parameters of the tunnel envelope are higher in this simulation; therefore, the maximum value of the displacement is smaller than that of the random field simulation in the direction of 15 degrees of rotation. The principal stress distribution in the tunnel is shown in Figures 11(c) and 11(d). The significant stress relief in the tunnel envelope due to excavation resulted in a decrease of the major principal stress from 14.50 MPa to 0.27 MPa. Due to the randomness of the parameters, the stresses in the tunnel surrounding rock show asymmetric distribution characteristics.

The enlarged local model of anisotropic random field with 45 degrees of rotation is shown in Figure 12(a). After excavation, the deformation of tunnel surrounding rock is shown in Figure 12(b). Under this condition, the tunnel deformation shows the distribution pattern that the left side wall is large while the right side wall is small. The maximum deformation occurs in the middle of the left sidewall with a

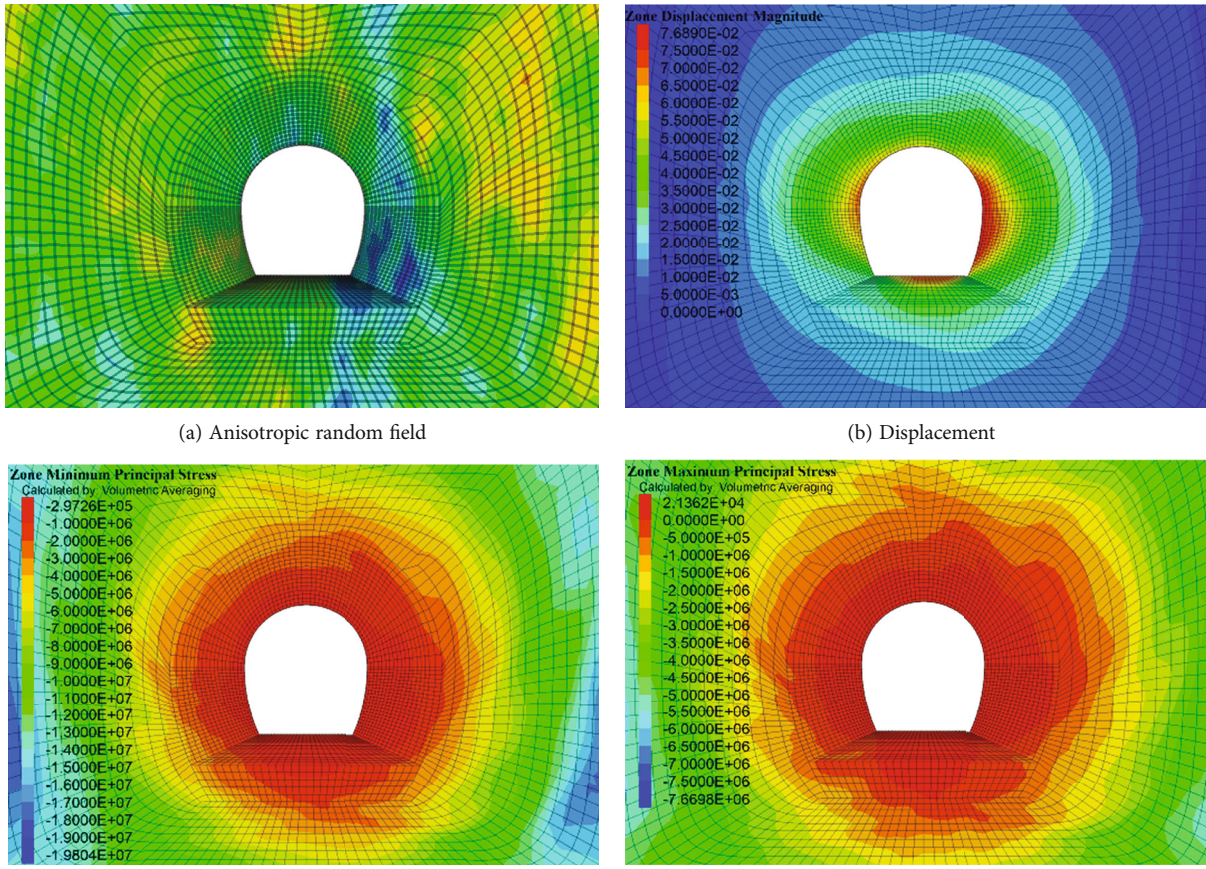

(a) Anisotropic random field

(b) Displacement

(c) Major principal stress

(d) Minor principal stress

Figure 15: Analysis of cavern excavation results with 90° anisotropic field.

value of 77.9 mm, and the main stress distribution in the chamber is shown in Figures 12(c) and 12(d). The excavation resulted in a significant release of the ground stress in the tunnel surrounding rock. The major principal stress decreased from 14.50 MPa to 0.44 MPa. The minor principal stress decreased from 14.50 MPa in compressed condition to 0.02 MPa in tensile stress. Although the tunnel shape is symmetrical, the randomness of the parameters makes the stresses in the tunnel envelope show asymmetric distribution.

An enlarged local model of the anisotropic random field rotated by 60 degrees is shown in Figure 13(a). Figure 13(b) demonstrates the deformation of the tunnel excavation. Overall, the deformation of the left side wall is larger than that of the right side wall. The maximum displacement is 76.2 mm, which occurs in the middle of the left side wall at about 3.6 m from the bottom edge. Figures 13(c) and 13(d) show the main stress distribution in the tunnel envelope. Due to the excavation, the tunnel surrounding rock has produced obvious stress release.

Figure 14(a) shows the local model of anisotropic random field with 75 degrees of rotation. Figure 14(b) shows the simulation results of the deformation of the tunnel envelope after excavation. In general, the displacement of the left side wall of the tunnel enclosure is larger than that of the right side wall. The distribution direction of the most value of displacement is orthogonal to the random field anisotropy direction, and the maximum deformation value of 81.6 mm appears in the direction of 165 degrees on the left side of the vault. The main stress distribution of the cavern chamber, after excavation, and the ground stress of the tunnel surrounding rock occurred a significant stress release. The simulation results of large and small principal stresses are shown in Figures 14(c) and 14(d). The major principal stress decreases from 14.50 MPa to 0.36 MPa and remains in the compressive state. The randomness of the parameters makes the stresses in the cavity surrounding rock show asymmetric distribution.

Figure 15(a) shows an enlarged view of the local model of the rotated 90 degrees of anisotropic random field. The deformation of the surrounding rock after tunnel excavation is shown in Figure 15(b). It can be seen that, in general, the surrounding rock of the tunnel shows a pattern that the deformation of the right side wall is larger than that of the left side wall. The distribution direction of the displacement maximum is orthogonal to the random field anisotropy direction. A strip of rock with weaker mechanical parameters appears on the right side of the tunnel envelope. This increases the displacement of the surrounding rock in this area. The maximum deformation of the tunnel envelope is 76.9 mm, which occurs in the middle of the right sidewall about 4 m from the bottom edge. Figures 15(c) and 15(d)

Table 3: Summary and comparison between simulation results with random field with different rotation angle.

Computing conditions: anisotropic random field with different rotation angle	Maximum deformation (mm)	Location that maximum deformation occurs	Major principal stress (MPa)	Minor principal stress (MPa)
0°	81.3	Right side wall	0.34	-0.02
15°	85.7	Right side wall	0.19	-0.02
30°	65.2	Right side wall	0.27	-0.02
45°	77.9	Left side wall	0.44	-0.02
60°	76.2	Left side wall	0.44	-0.02
75°	81.6	Left side wall	0.36	-0.02
90°	76.9	Right side wall	0.30	-0.02

show the main stress distribution of the cavern. It can be seen that there is a significant stress release in the tunnel surrounding rock due to excavation. The major principal stress decreases from 14.50 MPa to 0.30 MPa.

For comparison between random fields with different rotation angle, the information is collected and summarized in Table 3. It can be seen that, due to the variability of mechanical parameters caused, the stresses in the cavern envelope exhibit an asymmetric distribution. There is a significant stress release in the tunnel surrounding rock due to excavation in each simulation, and the general distribution pattern is similar. In addition, when the rotation angle is 45°, 60°, and 75°, the maximum deformation occurs in the middle of the left side wall and has a slightly larger major principal than other conditions.

5. Conclusion

In this study, numerical simulation of excavation deformation of hydraulic tunnels was carried out for the anisotropic random field of red-bedded soft rocks in central Yunnan. The Mohr-Coulomb model was chosen for the rock material, and the internal friction angle and cohesion were set as random parameters, while other parameters were defined as constants. The effects of different correlation functions and different correlation lengths on the cavern excavation are compared in the isotropic random field model. The deformation characteristics and stress distribution laws of the anisotropic random field with different rotation angles are also compared.

The stress distribution patterns of anisotropic random field with different rotation angles are compared, because the randomness of the parameters causes the displacement and stress field of the cavern surrounding rock after excavation to show an asymmetric distribution law. The distribution law of maximum displacement is mainly related to the high and low values of the random parameters of the excavated cavern envelope. The maximum displacement value generally appears at the lowest parameter value. For the deeply buried tunnel in this study, the horizontal ground stress is large. The maximum displacement of the tunnel envelope appears at the side walls on both sides and not at the vault position. At the same time, there is an obvious stress release in the tunnel envelope. The excavation-induced ground stress release is weaker in the areas where the stochastic parameters are taken to be higher than elsewhere. Large deformation also does not occur in these domains.

Data Availability

The data used to support the findings of this study are included within the article.

Conflicts of Interest

The authors declare no conflict of interest.

Acknowledgments

This research is supported by the Fundamental Research Funds for the Central Universities (B200201059) and the Natural Science Foundation of China (Grant Nos. 51709089, 51939004, 12062026, and 11772116).

References

[1] J. C. Zhang, W. Y. Xu, H. L. Wang, R. B. Wang, Q. X. Meng, and S. W. du, "A coupled elastoplastic damage model for brittle rocks and its application in modelling underground excavation," *International Journal of Rock Mechanics and Mining Sciences*, vol. 84, pp. 130–141, 2016.

[2] Q.-X. Meng, H.-L. Wang, W.-Y. Xu, W. C. Xie, R. B. Wang, and J. C. Zhang, "Robust equivalent tunnelling Mohr–Coulomb strength parameters for generalised Hoek–Brown media," *European Journal of Environmental and Civil Engineering*, vol. 20, no. 8, pp. 841–860, 2016.

[3] Y. Ding, Q. Zhang, S. Zhao, W. Chu, and Q. Meng, "An improved DEM-based mesoscale modeling of bimrocks with high-volume fraction," *Computers and Geotechnics*, vol. 157, article 105351, 2023.

[4] Q. Meng, H. Xue, H. Song, X. Zhuang, and T. Rabczuk, "Rigid-block DEM modeling of mesoscale fracture behavior of concrete with random aggregates," *Journal of Engineering Mechanics*, vol. 149, no. 2, article 04022114, 2023.

[5] Q.-X. Meng and W. Wang, "A novel closed-form solution for circular openings in generalized Hoek-Brown media," *Mathematical Problems in Engineering*, vol. 2014, Article ID 870835, 7 pages, 2014.

[6] D. M. Zhang, L. X. Ma, J. Zhang, P. Y. Hicher, and C. H. Juang, "Ground and tunnel responses induced by partial leakage in

saturated clay with anisotropic permeability," *Engineering Geology*, vol. 189, pp. 104–115, 2015.

[7] Y. Xie, M. Z. Hou, and C. Li, "Anisotropic characteristics of acoustic emission and the corresponding multifractal spectrum during progressive failure of shale under cyclic loading," *International Journal of Rock Mechanics and Mining Sciences*, vol. 165, article 105364, 2023.

[8] B. Y. Ni and C. Jiang, "Interval field model and interval finite element analysis," *Computer Methods in Applied Mechanics and Engineering*, vol. 360, p. 112713, 2020.

[9] A. Sofi and E. Romeo, "A novel interval finite element method based on the improved interval analysis," *Computer Methods in Applied Mechanics and Engineering*, vol. 311, pp. 671–697, 2016.

[10] L. Zhenyu and C. Qiu, "A new approach to fuzzy finite element analysis," *Computer Methods in Applied Mechanics and Engineering*, vol. 191, no. 45, pp. 5113–5118, 2002.

[11] O. Ait-Salem Duque, A. R. Senin, A. Stenti, M. de Munck, and F. Aparicio, "A methodology for the choice of the initial conditions in the model updating of welded joints using the fuzzy finite element method," *Computers and Structures*, vol. 85, no. 19-20, pp. 1534–1546, 2007.

[12] J. Zhang, Z. P. Wang, G. D. Zhang, and Y. D. Xue, "Probabilistic prediction of slope failure time," *Engineering Geology*, vol. 271, article 105586, 2020.

[13] Q.-X. Meng, H.-L. Wang, W.-Y. Xu, and Y. L. Chen, "Numerical homogenization study on the effects of columnar jointed structure on the mechanical properties of rock mass," *International Journal of Rock Mechanics and Mining Sciences*, vol. 124, article 104127, 2019.

[14] Q. Meng, H. Wang, M. Cai, W. Xu, X. Zhuang, and T. Rabczuk, "Three-dimensional mesoscale computational modeling of soil-rock mixtures with concave particles," *Engineering Geology*, vol. 277, article 105802, 2020.

[15] Q.-X. Meng, H. L. Wang, W. Y. Xu, and Q. Zhang, "A coupling method incorporating digital image processing and discrete element method for modeling of geomaterials," *Engineering Computations*, vol. 35, no. 1, pp. 411–431, 2018.

[16] Q.-X. Meng, D. Lv, and Y. Liu, "Mesoscale computational modeling of concrete-like particle-reinforced composites with non-convex aggregates," *Computers & Structures*, vol. 240, article 106349, 2020.

[17] Q.-X. Meng, W.-Y. Xu, H.-L. Wang, X. Y. Zhuang, W. C. Xie, and T. Rabczuk, "DigiSim – an open source software package for heterogeneous material modeling based on digital image processing," *Advances in Engineering Software*, vol. 148, article 102836, 2020.

[18] G. Kong, J. Fang, Z. Lv, and Q. Yang, "Effects of pile and soil properties on thermally induced mechanical responses of energy piles," *Computers and Geotechnics*, vol. 154, article 105176, 2023.

[19] D. Ren, X. Wang, Z. Kou et al., "Feasibility evaluation of CO_2 EOR and storage in tight oil reservoirs: a demonstration project in the Ordos basin," *Fuel*, vol. 331, article 125652, 2023.

[20] J. Zhang and H. W. Huang, "Risk assessment of slope failure considering multiple slip surfaces," *Computers and Geotechnics*, vol. 74, pp. 188–195, 2016.

[21] G. B. Beacher and T. S. Ingra, "Stochastic FEM in settlement predictions," *Journal of the Geotechnical Engineering Division*, vol. 107, no. 4, pp. 449–463, 1981.

[22] E. Vanmarcke and M. Grigoriu, "Stochastic finite element analysis of simple beams," *Journal of Engineering Mechanics*, vol. 109, no. 5, pp. 1203–1214, 1983.

[23] R. Suchomel and D. Mašín, "Probabilistic analyses of a strip footing on horizontally stratified sandy deposit using advanced constitutive model," *Computers and Geotechnics*, vol. 38, no. 3, pp. 363–374, 2011.

[24] D.-Q. Li, T. Xiao, L.-M. Zhang, and Z. J. Cao, "Stepwise covariance matrix decomposition for efficient simulation of multivariate large-scale three-dimensional random fields," *Applied Mathematical Modelling*, vol. 68, pp. 169–181, 2019.

[25] D. Griffiths and P. Lane, "Slope stability analysis by finite elements," *Geotechnique*, vol. 49, no. 3, pp. 387–403, 1999.

[26] S. E. Cho, "Effects of spatial variability of soil properties on slope stability," *Engineering Geology*, vol. 92, no. 3-4, pp. 97–109, 2007.

[27] S.-H. Jiang, D.-Q. Li, Z.-J. Cao, C. B. Zhou, and K. K. Phoon, "Efficient system reliability analysis of slope stability in spatially variable soils using Monte Carlo simulation," *Journal of Geotechnical and Geoenvironmental Engineering*, vol. 141, no. 2, 2015.

[28] C. Li, L. Kong, and R. An, "Evolution of cracks in the shear bands of granite residual soil," *Journal of Rock Mechanics and Geotechnical Engineering*, vol. 14, no. 6, pp. 1956–1966, 2022.

[29] G. A. Fenton, "Error evaluation of three random-field generators," *Journal of Engineering Mechanics*, vol. 120, no. 12, pp. 2478–2497, 1994.

[30] C. H. Juang, J. Zhang, M. Shen, and J. Hu, "Probabilistic methods for unified treatment of geotechnical and geological uncertainties in a geotechnical analysis," *Engineering Geology*, vol. 249, pp. 148–161, 2019.

Hindawi
Geofluids
Volume 2023, Article ID 9159098, 17 pages
https://doi.org/10.1155/2023/9159098

Research Article

The Damage Induced by Blasting Excavation and Seepage Characteristics of Deep Rock under High Seepage Pressure

Qian Dong[1,2] **Xin Liu**[3] **Hangli Gong**[3] **Yi Luo**[3,4] **Xinping Li**[3,4] **and Liangjun Wang**[5]

[1]*State Key Laboratory of Precision Blasting, Jianghan University, Wuhan 430056, China*
[2]*Hubei Key Laboratory of Blasting Engineering, Jianghan University, Wuhan 430056, China*
[3]*School of Civil Engineering and Architecture, Wuhan University of Technology, Wuhan 430070, China*
[4]*Hubei Key Laboratory of Roadway Bridge and Structure Engineering, Wuhan University of Technology, Wuhan 430070, China*
[5]*China Gezhouba Group Co., Ltd., Wuhan 430070, China*

Correspondence should be addressed to Hangli Gong; hangligong58@whut.edu.cn

Received 6 November 2022; Revised 18 December 2022; Accepted 3 April 2023; Published 18 April 2023

Academic Editor: Yiding Bao

By taking the blasting excavation of a deeply buried karst tunnel in the North Tianshan Mountains in China as research objects, the damage induced by blasting excavation and seepage characteristics of deep rock under high seepage pressure was investigated. The COMSOL Multiphysics® software was adopted to establish a simulation model for the blasting excavation of a deeply buried tunnel. By embedding the stress-damage-seepage multifield coupled constitutive relationship, the mechanism of the influences of factors including blasting load, geostress, and hydraulic pressure of karst caves on the blasting excavation-induced damage to, and seepage characteristic of, the surrounding rocks of the tunnel. The results indicate that blasting excavation in the karst tunnel triggers the damage of surrounding rocks, which consists of blasting-induced damage and unloading damage. The time-history curve of the variable for surrounding rock damage rises and consequently tends to a constant value. With the increases in blasting load, geostress, and hydraulic pressure of karst caves, the degree of damage to surrounding rocks is intensified; an increase in geostress will weaken the effect of blasting-induced damage to rock while increasing rock damage arising from unloading. Meanwhile, the degree of damage to the surrounding rock can affect the seepage velocity of water in the surrounding rock to a certain extent. A strong damage and seepage coupled effect occur in the blasting excavation process of the karst tunnel. The such coupled effect is strengthened little by little with the increases in the degree of surrounding rock damage and hydraulic pressures. The results are expected to provide theoretical guidance for hazard prevention and control of blasting excavation in karst tunnels under high geostress conditions.

1. Introduction

Generally, when the magnitude of geostress in deep rocks is above 10 MPa, a new excavation tunnel surface is formed within about 10 ms during a blasting excavation process, yielding a strain magnitude of 10^{-1}. Dynamic stresses generated by explosive blasting and transient unloading are important factors that trigger rock fracture and loosening [1–3]. However, rocks in high-pressure water-rich zones are inclined to be subjected to the effect of high-pressure seepage. Fissures of rocks, under the effect of the excavation-induced dynamic disturbance, undergo a process evolving from initiation, propagation, and coalescence. This causes deteriorating mechanical properties of surrounding rocks while inducing the enlargement of seepage channels, which promotes the seepage field to further evolve [4–6]. Under the coupled effect of seepage and dynamic loading, the transient water pressure of rock fissures will be largely increased, which enables the fissures to further propagate and leads to structural damage of rock, even directly triggers rock failure [7, 8]. Therefore, it is necessary to study the damage induced by blasting excavation and seepage characteristics of deep rock under high seepage pressure.

A series of studies on the blasting excavation-induced damage of rock under high seepage pressure and seepage problems have been investigated worldwide. Tan et al. [9]

discovered that surrounding rocks that lie between a tunnel and a karst under the excavation-induced dynamic disturbance are more prone to suffer a large deformation and even suffer failures, which calls for special attention to the stability of surrounding rocks. Li et al. [10] programmed a program for analyzing and calculating the seepage and damage of surrounding rocks under dynamic loading to obtain the law of the changes in the radius of the damage zone in surrounding rocks with varying pore water pressure under the restriction of multiple factors. Their results proved that the value of the range of the damage zone in surrounding rocks is positively correlated with pore water pressure. Liu et al. [11] believed that damage evolution is a process by which microcracks evolve from initiation, propagation, and coalescence. They constructed a stress-seepage-damage coupled model characterizing changes in permeability and damage evolution of surrounding rocks in the tunnel excavation process and used seepage theory to deduce an equation for the permeability evolution of surrounding rocks. Huang et al. [12] analyzed distributions of the stress field, seepage field, and damage field of surrounding rocks during the tunnel excavation process by taking water inrush hazards that occurred in fracture zones of a karst tunnel as a research object. Their results indicated that disturbance arising from tunnel excavation leads to the redistribution of the in situ rock stress field and causes the change in the seepage state of surrounding rocks. Zhao et al. [13] studied the influences of spatial distribution characteristics of karst caves' locations on the deformation and seepage field of rocks surrounding tunnels. Yang et al. [14] conducted three-dimensional fluid-solid coupled model tests to explore the evolution law of water inrush in karst caves which were induced by tunnel excavation and varying water pressure in the caves. Yuan et al. [15] simulated the influence of mining disturbance in mines on the faults and rivers in the surrounding area based on the rock fluid-solid coupled theory. The results showed that mining activities can cause further damage to faults and rock bridges, causing increased rock permeability, which may allow mining filed to form a coalesced seepage channel spanning from a river to faults. By considering the fluid-solid coupled effect, Guo et al. [16] investigated the evolution laws of the displacement field and seepage field of rock mass on the layer for preventing water inrush when a tunnel face was close to a high-pressure water-rich karst cavity in tunnel excavation and its critical water inrush characteristics. Huang et al. [17, 18] found the permeability of surrounding rocks after tunnel excavation was finished and increased to one or several orders of magnitudes and analyzed the influences of the thickness of damage zones on tunnel gushing and pore pressure distribution. To sum up, exploring the issues about the damage evolution of surrounding rocks under the coupled effect of dynamic loading and seepage field is of significance to surrounding rock stability as well as water inrush prevention and control of deep rock mass.

The extra-long, deeply buried karst tunnel in the North Tianshan Mountains in Xinjiang Province, China, contains rich water, with some tunnel sections containing rich water. It has a maximum burial depth of 1060 m. The tunnel crosses multiple fault fracture zones and has complex geological tectonics, and the surrounding rocks in the fracture development zone of jointed rock mass contain a large number of soluble rocks, which can lead underground water to accumulate to form a karst cave and produces high seepage pressure in surrounding rock masses. It belongs to a typical deep-buried, high-permeability rock tunnel. In this research, the stress-damage-seepage multifield constitutive model was embedded into COMSOL Multiphysics, and the damage induced by blasting excavation and seepage characteristics of deep rock under high seepage pressure were analyzed. The influence mechanism of blasting load, geostress, water pressure of karst caves on the tunnel blasting excavation-induced damage to, and seepage characteristics of surrounding rocks were discussed. The research results can provide theoretical support and reference for similar deep high-permeability rock mass blasting excavation.

2. Blasting Excavation-Induced Damage and Seepage Characteristics of Surrounding Rocks in the North Tianshan Karst Tunnel

2.1. The Stress-Seepage-Damage Coupled Model. For the deeply buried tunnel under the effect of blasting excavation, a stress-seepage-damage multifield coupled constitutive relationship was established using a Drucker-Prager (D-P) yield criterion-based elastoplastic damage model. This constitutive relationship also considered the effects of water pressure and karst water flow in surrounding rocks in karst caves surrounding the tunnel, on the damage to surrounding rocks. Once the effect of effective stress on rocks under the effect of exerted loads exceeds the strength of rocks, plastic strain tends to occur to rocks, accompanied with damage to a certain degree. An internal variable (herein referring to the equivalent plastic strain) is used to characterize the evolution of the rock damage variable based on the elastoplastic damage theory considering plastic deformation mechanism and stiffness degradation. Previous research indicates that the rock damage variable has a linear relationship with equivalent plastic strain, which can be expressed as an exponential function of equivalent plastic strain [19]. tThe equivalent plastic strain $\bar{\varepsilon}_{\mathrm{p}}$ is calculated as

$$\bar{\varepsilon}_{\mathrm{p}} = \frac{\sqrt{2}}{3}\sqrt{\left(\varepsilon_{\mathrm{p1}} - \varepsilon_{\mathrm{p2}}\right)^2 + \left(\varepsilon_{\mathrm{p2}} - \varepsilon_{\mathrm{p3}}\right)^2 + \left(\varepsilon_{\mathrm{p3}} - \varepsilon_{\mathrm{p1}}\right)^2}, \quad (1)$$

where ε_{p1} denotes the first principal plastic strain; ε_{p2} refers to the secondary principal plastic strain; and ε_{p3} is the third principal plastic strain.

The evolution equation of the corresponding damage variable D is as follows:

$$D = 1 - \exp\left[-\kappa\left(\bar{\varepsilon}^p - \bar{\varepsilon}_0^p\right)\right], \quad (2)$$

where the threshold of the equivalent plastic strain $\bar{\varepsilon}_0^p = 0$, namely, there is damage evolution when the equivalent plastic strain occurs; k represents the positive constant obtained in experiments.

There are pores and microcracks in rocks. It can be assumed that water and rock mass are incompressible material under deep high seepage pressure condition, and the weight of water is neglected, the surrounding rock seepage field control equation is written as

$$\nabla[-\delta_{\mathrm{k}}\mathrm{K}/(\rho_1 g)(\nabla \mathrm{p} + \rho_1 \mathrm{g}\nabla \mathrm{z})] = \delta_{\mathrm{Q}}\mathrm{Q_s}, \tag{3}$$

where ρ_1 denotes the density of fluids; K is the permeability of rock; $\mathrm{Q_s}$ represents the source and sink of fluids; p is the pore water pressure; and δ_{k} and δ_{Q} denote the flux and source proportion coefficient, valued as 1.0.

The change in the porosity of rock under the effects of different loads and the change in the seepage channel induced by rock damage were jointly used to characterize the change in the fluidity of fluids in rocks. On this basis, a rock stress-seepage-damage multifield coupled constitutive relationship was established [20]

$$K = K_0(\phi/\phi_0)^3 \exp(\alpha_k D), \tag{4}$$

where K_0 denotes initial permeability of rock, ϕ represents the porosity of the rock, ϕ_0 is the initial porosity of the rock, and α_k represents the coefficient of influence of damage on the permeability of solid media, which is set to 5.

The total stress of rock is jointly contributed by the effective stress borne by skeleton grains and pore water pressure. The principle for the effective stress of porous media is expressed as

$$\sigma_{ij}{}^{*} = \sigma_{ij} - \alpha\delta_{ij}p, \tag{5}$$

where $\sigma_{ij}{}^{*}$ is the effective stress tensor; σ_{ij} denotes the total stress; α is the equivalent pore water pressure coefficient; and δ_{ij} denotes the Kronecker symbol.

Hence, the constitutive relationship for the stress-strain elastoplastic damage of surrounding rocks under a high seepage pressure field is presented as follows:

$$\sigma_{ij}^{*} = C_d^e : \left(\varepsilon_{ij} - \varepsilon_{ij}^p\right), \tag{6}$$

where ε_{ij} is the total strain tensor, ε_{ij}^p denotes the plastic strain tensor, and C_d^e represents the damage elasticity matrix. In $C_d^e = 2G_d I + K_d I \otimes I$, I is a symmetric fourth-order tensor. In $I_{ijkl} = 1/2(\delta_{ik}\delta_{jl} + \delta_{il}\delta_{jk})$, G_d and K_d represent shear modulus and volume modulus of damage, respectively, which can be expressed by G_0 and K_0.

$$G_d = (1-D)G_0 = \frac{E(D)}{2(1+\mu)}\,; K_d = (1-D)K_0 = \frac{E(D)}{3(1-2\mu)}. \tag{7}$$

2.2. Numerical Model of the North Tianshan Karst Tunnel. The burial depth of a karst tunnel section for the North Tianshan Tunnel is about 1000 m. The rocks surrounding the tunnel are mainly composed of limestone mixed with clastic rock, and the groundwater is karst fracture water. The tunnel section studied is situated at the wing of the anticline. There is a karst cave with a diameter of about 10 m and a water pressure of 10 MPa located 10 m from the tunnel boundary. The tunnel face is horseshoe-shaped with dimensions of 9 m × 12 m. In the numerical calculation process, the tunnel shape was simplified into a circle. Given that the diameter of the tunnel face in practical engineering was set to 10 m, as shown on the left, and the karst cave in its natural state exhibits complex shapes, the shape of the karst cave was also simplified into a circle with a diameter of 10 m, as illustrated in the right; the distance between the karst cave and tunnel boundary was 10 m.

To analyze the coupled characteristics of damage to and seepage of surrounding rocks in the tunnel blasting excavation process, the modeling process did not consider the effect of stress concentration in the karst cave on the damage evolution of surrounding rocks and regarded the karst cave that possesses mechanical properties of surrounding rocks as the source of high-pressure water sources. The COMSOL Multiphysics was used to establish a two-dimensional model measuring 100 m × 100 m (width × height), as shown in Figure 1.

The calculations are finished in two steps: in the first step, static force calculations are conducted to derive the geostress field and water pressure field prior to tunnel excavation; in the second step, the geostress and water pressure calculated in the first step are taken as initial values to perform the dynamic calculation of blasting excavation.

(1) Seepage boundary conditions

When calculating static stress, according to practical engineering conditions and considering the karst cave bore a large water pressure, its gravity gradient was neglected; the water pressure of the karst cave was set to 10 MPa, the water pressure on the external boundaries of the model was set to 0.5 MPa so as to simulate the surrounding flow field, while dynamic stress arising from blasting excavation was calculated by setting 0 MPa water pressure on the tunnel boundary and other conditions keeping unchanged.

(2) Displacement and stress boundary conditions

Existing research on stress distribution in deep rocks of China reveals that when the burial depth was 1000 m, vertical geostress was about 20 MPa and horizontal geostress was 20 MPa [21]. During the calculation of static stress, the stresses on the right boundary and upper boundary of the model were set to 20 MPa, while the normal displacements on the left and bottom boundaries of the model were restricted. When calculating the dynamic stress induced by blasting excavation, the external boundary conditions were unchanged, but the effect of blasting on surrounding rocks was simulated using an equivalent loading mode on the

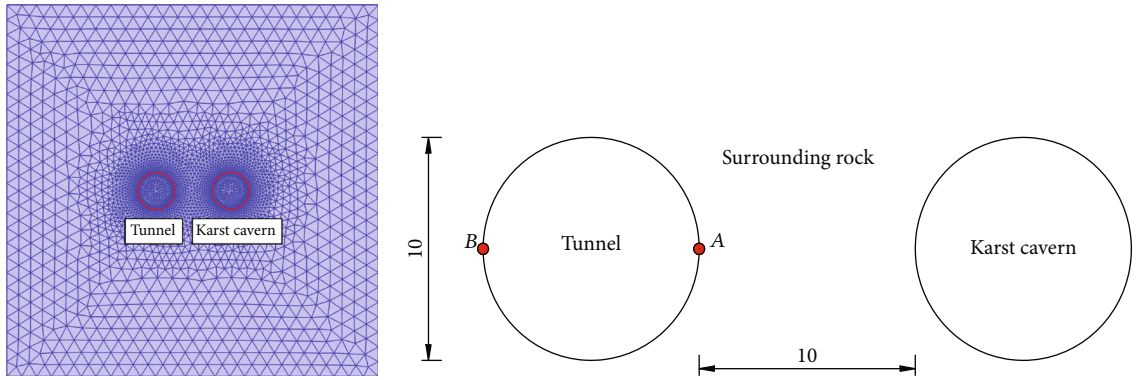

(a) Model grid division

(b) Tunnel and karst cave layout (unit: m)

Figure 1: Two-dimensional geometric model.

Table 1: Blasting parameters.

P_{ej}(kg/m^3)	D/m/s	D_{cj}mm	L_{cj}m	D_{bj}mm	L_{bj}m	L/m
1200	3600	32	2	45	2.5	0.9

tunnel boundary in the tunnel excavation section. The load was simplified into a triangular load, and the equivalent load can be calculated using the following equations [22, 23]:

$$P_0 = \frac{\rho_e D^2}{2(\gamma+1)}\left(\frac{d_c}{d_b}\right)^{2\gamma}\left(\frac{l_c}{l_b}\right)^{\gamma}\cdot n,$$
$$P_e = \frac{d_b}{L}P_0, \tag{8}$$

where P_0 is the peak load of the hole wall of the tunnel; ρ_e refers to the explosive density; D denotes the detonation velocity of explosive; d_c and l_c represent the diameter and length of the explosive package; d_b and l_b refer to the diameter and length of a blasting hole; γ is the entropy of explosive, which is set to 3; n denotes the pressure increment coefficient, valued as 8; P_e represents the equivalent peak load; and L is the distance between blasting holes. The blasting parameters are shown in Table 1.

The equivalent peak load was calculated to be 50 MPa, which was applied on the tunnel boundary. The blasting load curve is shown in Figure 2.

The material parameters of saturated limestone surrounding the karst section of the North Tianshan tunnel were chosen, as listed in Table 2.

2.3. Tunnel Blasting Excavation-Induced Damage and Seep Characteristics of Surrounding Rocks. Figure 3(a) displays the nephogram of water pressure distribution on surrounding rocks before tunnel blasting excavation (the water pressure on the boundary of the karst cave is 10 MPa). It can be found that with the increasing distance between the karst cave and the tunnel boundary, water pressure on the surrounding rock uniformly decreases. This causes uneven distribution of water pressure on the rocks surrounding the tunnel: the water pressure on the surrounding rocks on the right side of the tunnel near the karst cave is large, while the water pressure on the surrounding rocks on the left side which is far away from the karst cave is small.

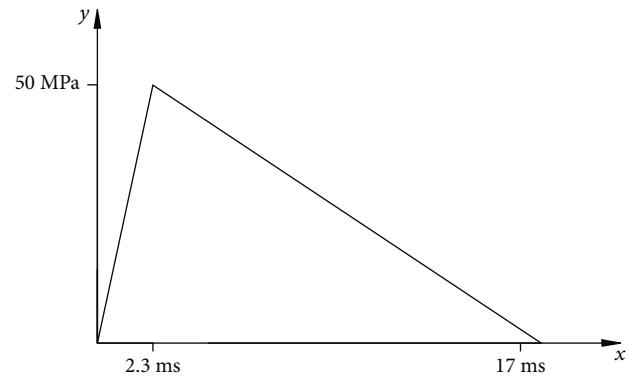

Figure 2: Time history curve of explosion load.

The distribution of the surrounding rock damage in the tunnel after stable excavation in the case of inconsistent water pressures is presented in Figure 3(b). The range of damage to surrounding rocks on the left side of the tunnel is 1.83 m, while that of the right side of the tunnel is slightly large, which is 2.23 m.

To compare the differences in the changes in the damage of surrounding rocks on the left and right sides of the tunnels as well as the influence of water pressure on the damage evolution, measurement point A in the right-side wall and measurement point B in the left side wall of the tunnel were monitored, as shown in Figure 1(b). On this basis, the time-history curve of the damage variable of surrounding rocks, and water pressure in the tunnel blasting excavation process is plotted, as illustrated in Figure 4. The damage changes in measurement points A and B implied that damage to surrounding rocks mainly occurs at the moment that tunnel

Table 2: Rock material parameters.

Density (kg/m^3)	Elastic modulus (GPa)	Compressive strength (MPa)	Poisson ratio	Force of cohesion (MPa)	Angle of internal friction (°)	Initial permeability (m^2)	Original porosity
2600	40	102	0.22	5	50	10^{-12}	0.05

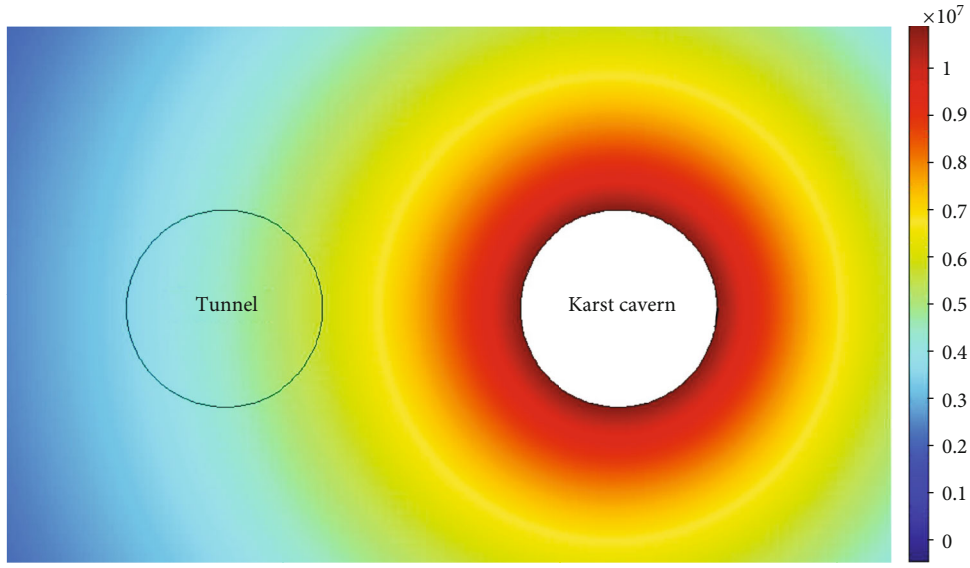

(a) Water pressure distribution (unit: MPa)

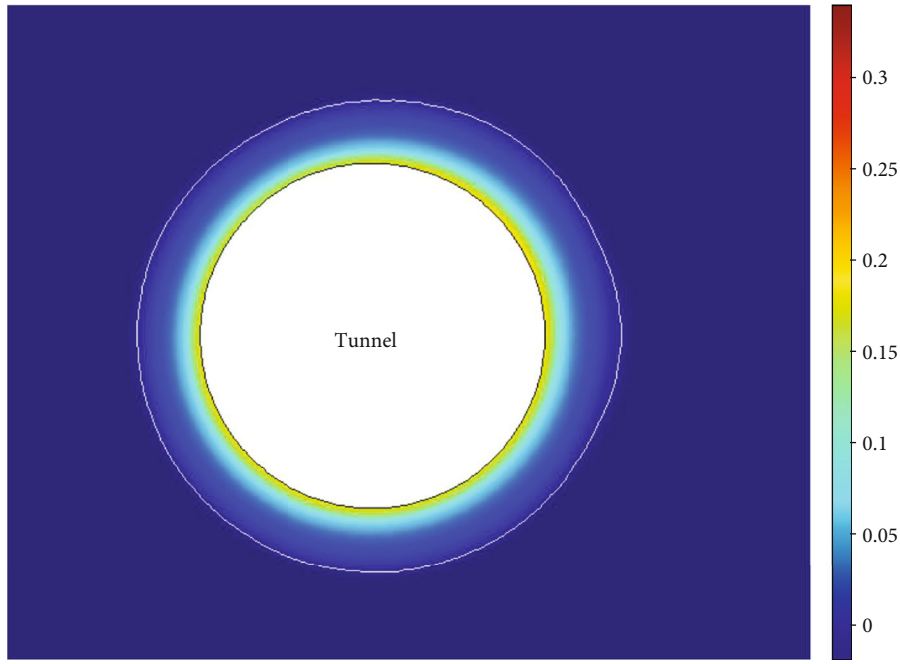

(b) Damage distributions

Figure 3: Water pressure distribution of tunnel before excavation and damage of surrounding rock in the stable stage.

excavation beings. The damage variable time-history curve shows a step-like increase: the increasing stage in the first step is found to be the blasting load impacting stage, corresponding to the peak stage of the load curve in Figure 2. The blasting load exerts a huge impact on surrounding rocks, which induces damage, namely, called blasting-induced damage; the damage at the second step occurs after the impact of the blasting load is fulfilled. At this moment, the tunnel excavation has been completed and forms a free face. The initial geostress on the tunnel profile section in

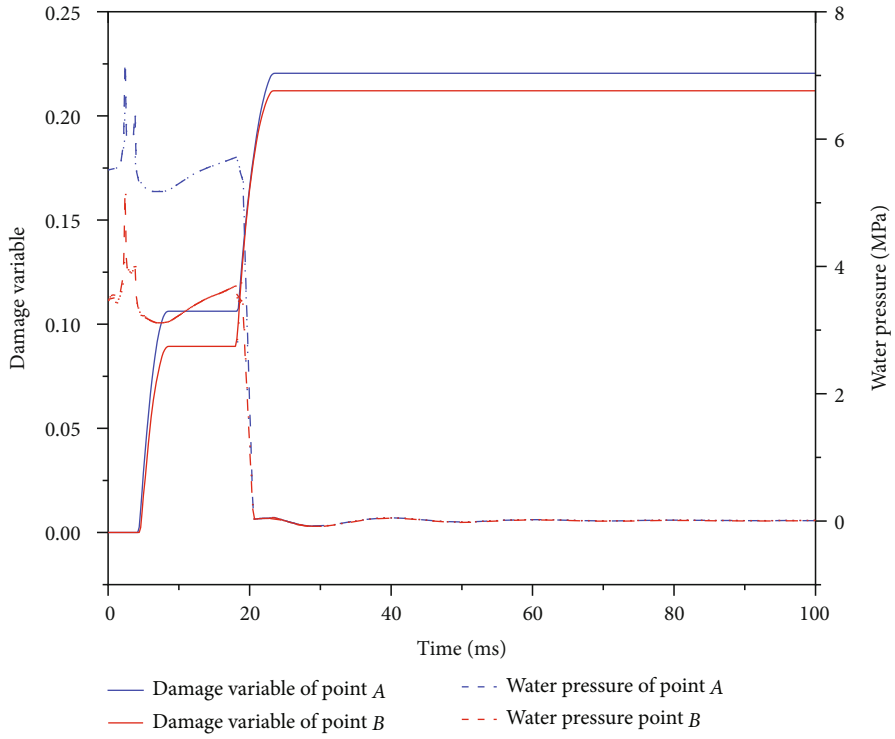

Figure 4: Time history curves of damage variable and water pressure at points A and B.

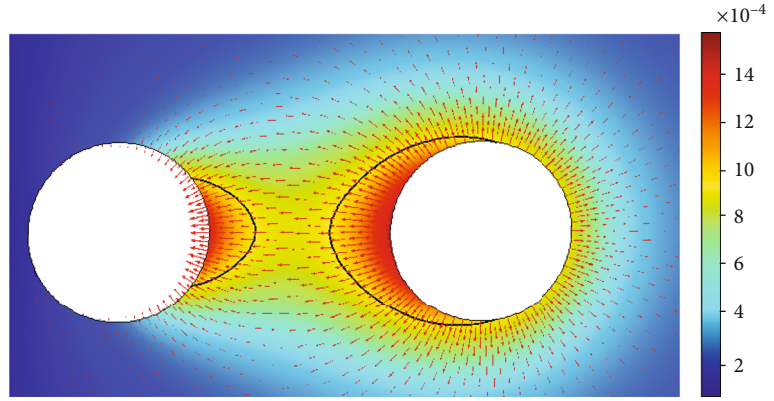

Figure 5: Velocity field distribution of surrounding rock after excavation (unit: m/s).

the normal direction and the effect of impact extrusion induced by blasting loads disappear instantly, namely, the effect of transient unloading acts, which leads to secondary damage to surrounding rocks. This consequently causes the generation of the second step, which occurs after 17 ms in the loading curve shown in Figure 2. Finally, the damage variable (called unloading-induced damage) measured at measurement point A is 0.22, while the damage variable at measurement point B is 0.21. In other words, the damage of surrounding rock is composed of two parts: explosion load and transient unloading of ground stress and the dynamic response caused by transient unloading always lags behind the explosion load, which is consistent with the research results of Lu et al. [24]. Measurement point A has larger damage than measurement point B, which is because A is subjected to a larger influence from the seepage field compared with B in the blasting excavation process. As can be seen from Figure 4, before blasting excavation, measurement point A suffers a larger water pressure, which leads the pore water pressure in rock mass to increase sharply in the blasting excavation stage. This is conducive to the propagation of cracks in rock masses, further causing damage to surrounding rocks, while the peak water pressure of measurement point A is higher than that of B at the blasting excavation stage, thus resulting in larger damage.

Figure 5 displays the nephogram of the flow velocity field distribution of surrounding rocks after excavation. Karst water seeped into the surrounding zones of the karst cave;

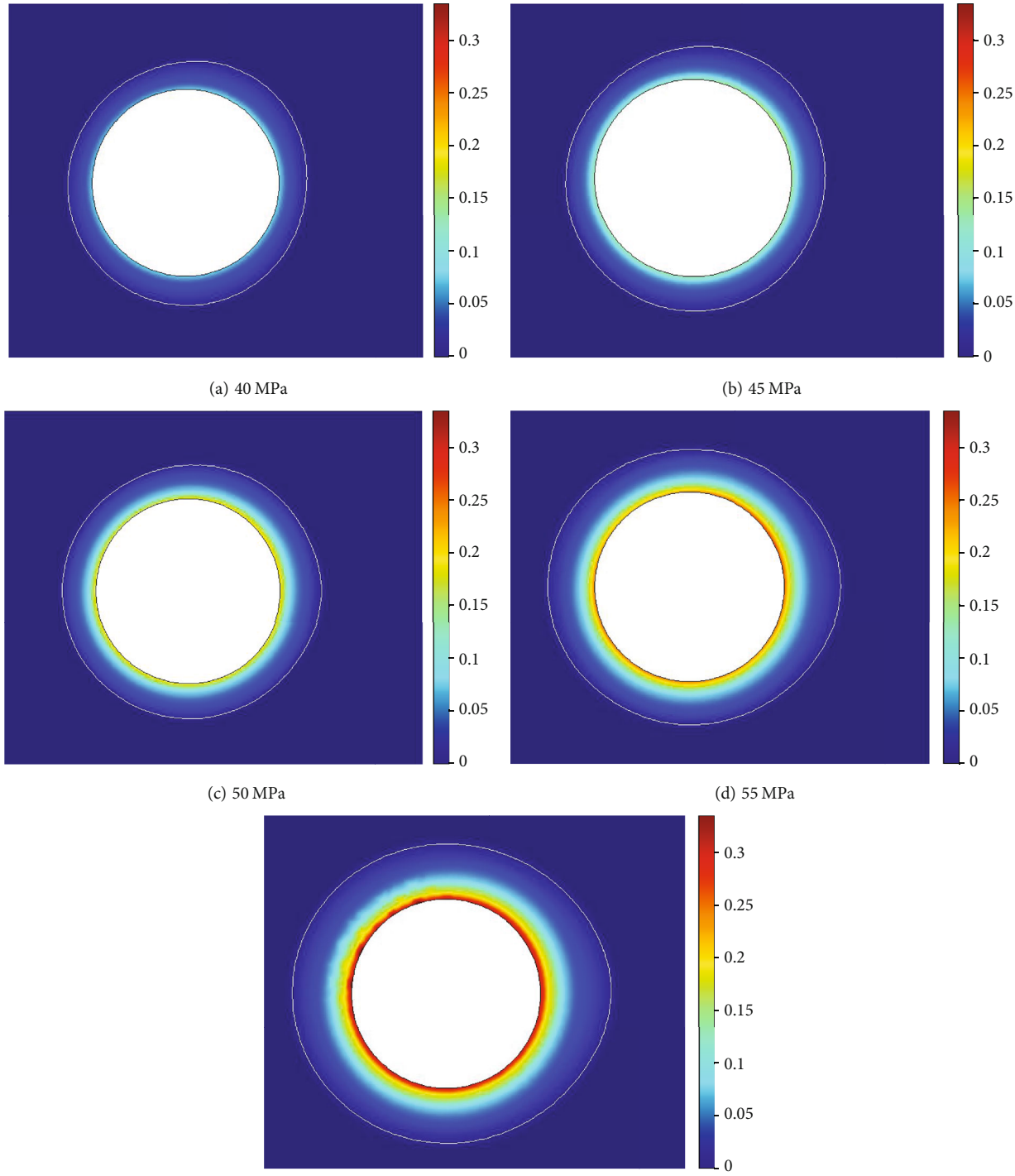

(a) 40 MPa

(b) 45 MPa

(c) 50 MPa

(d) 55 MPa

(e) 60 MPa

Figure 6: Damage of surrounding rock after excavation under different explosion loads.

however, due to the small distance between the right boundary of the tunnel and the karst cave and the larger damage caused by the coupled effects of blasting excavation and seepage field, the cracks in rock masses develop, which provides more seepage channels. The curve in the figure is the isoline at a flow velocity of 1×10^{-3} m/s. Karst water seepage is mainly concentrated on the right boundary of the tunnel. The process of crack initiation, propagation, and coalescence in the surrounding rock caused by karst tunnel excavation and finally forming a water inrush channel connecting the water source and the roadway fracture surface is basically consistent with the research results of Li et al. [25].

Based on the analysis aforementioned, the surrounding rock damage in the karst tunnel excavation process consists

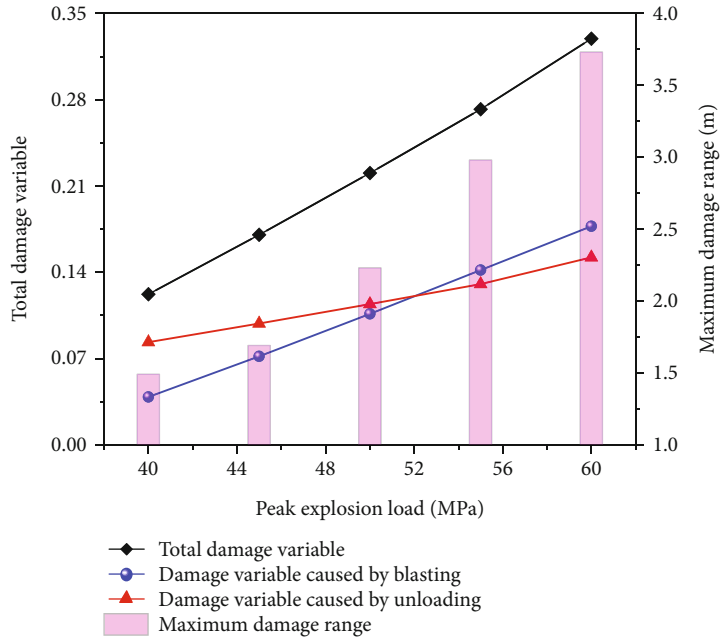

Figure 7: Damage of surrounding rock under different explosion loads.

of blasting-induced damage and unloading-induced damage. After the blasting excavation, the water pressure on the karst cave and damage state of the surrounding rocks of the tunnel also influence the distribution of the seepage field in the surrounding rocks after excavation. Furthermore, blasting load, geostress, and water pressure can directly affect the distribution of the surrounding rock damage. To expound the blasting excavation-induced damage and seepage characteristics of surrounding rocks in the tunnel under multifield coupled effects, the interactive relationship of damage field and seepage field was studied by adjusting the values of the influencing factors including blasting load, geostress, and water pressure on the karst cave.

3. Influencing Factors of the Damage and Seepage Characteristics of Surrounding Rocks

3.1. Influence of Blasting Load. As the blasting load directly acts on the excavation boundary during the tunnel blasting excavation process, the explosive loading degree can exert a direct influence on the degree of damage to surrounding rocks. The damage characteristics of surrounding rocks under different explosive loads (40, 45, 50, 55, and 60 MPa) and the relationship between the damage of surrounding rocks and the seepage field were investigated. Figure 6 displays the nephogram of damage of surrounding rocks after excavation under different explosive loads. With the increase of explosive peak load, the damage to surrounding rocks intensifies, and cracks are therefore more developed, which promotes the flow of high-pressure water in surrounding rocks. Under the effect of water pressure, the damage to surrounding rocks further increases, which makes the range of the damage zone of surrounding rocks at the right-side wall gradually exceed that at the left-side wall. The damage zone protrudes to the right.

In addition, changes in the damage variable at measurement point A and the maximum damage range of surrounding rocks on the right side of the tunnel can be used to characterize the influence of varying explosive loads, as shown in Figure 7. As illustrated in the figure, the total damage variable at measurement point A shows an approximately linear increase with increasing explosive load; the larger the explosive load, the larger the blasting-induced damage and unloading-induced damage. The damage range presents an accelerating increase.

The change in the seepage zone with a flow velocity above 1×10^{-3} m/s can be intuitively describe by the flow velocity field distribution, denoted as "seepage zone A", which is shown as the zone surrounded by isoline in Figure 8.

As the explosive load ingresses, the ranges of the tunnel and the seepage zone A located near the karst cave both show increasing enlargement and tend to coalesce; when the explosive load reaches 60 MPa, the right and left sides of seepage zone A coalesce. Figure 9 depicts the changes in flow velocity at measurement point A after excavation under different explosive loads. The explosive load increases from 40 MPa to 60 MPa. The flow velocity at measurement point A increases from 1.26×10^{-3} m/s to 1.39×10^{-3} m/s, presenting an increasing amplitude.

3.2. Influence of Geostress. The presence of the gravity effect of upper strata endows deeply buried rock mass with a larger initial geostress, which coupled with the effect of transient unloading induced by tunnel excavation to further triggers changes in the damage field and seepage field of surrounding rocks. Through establishing tunnel excavation models under different geostress conditions (10 MPa, 15 MPa, 20 MPa,

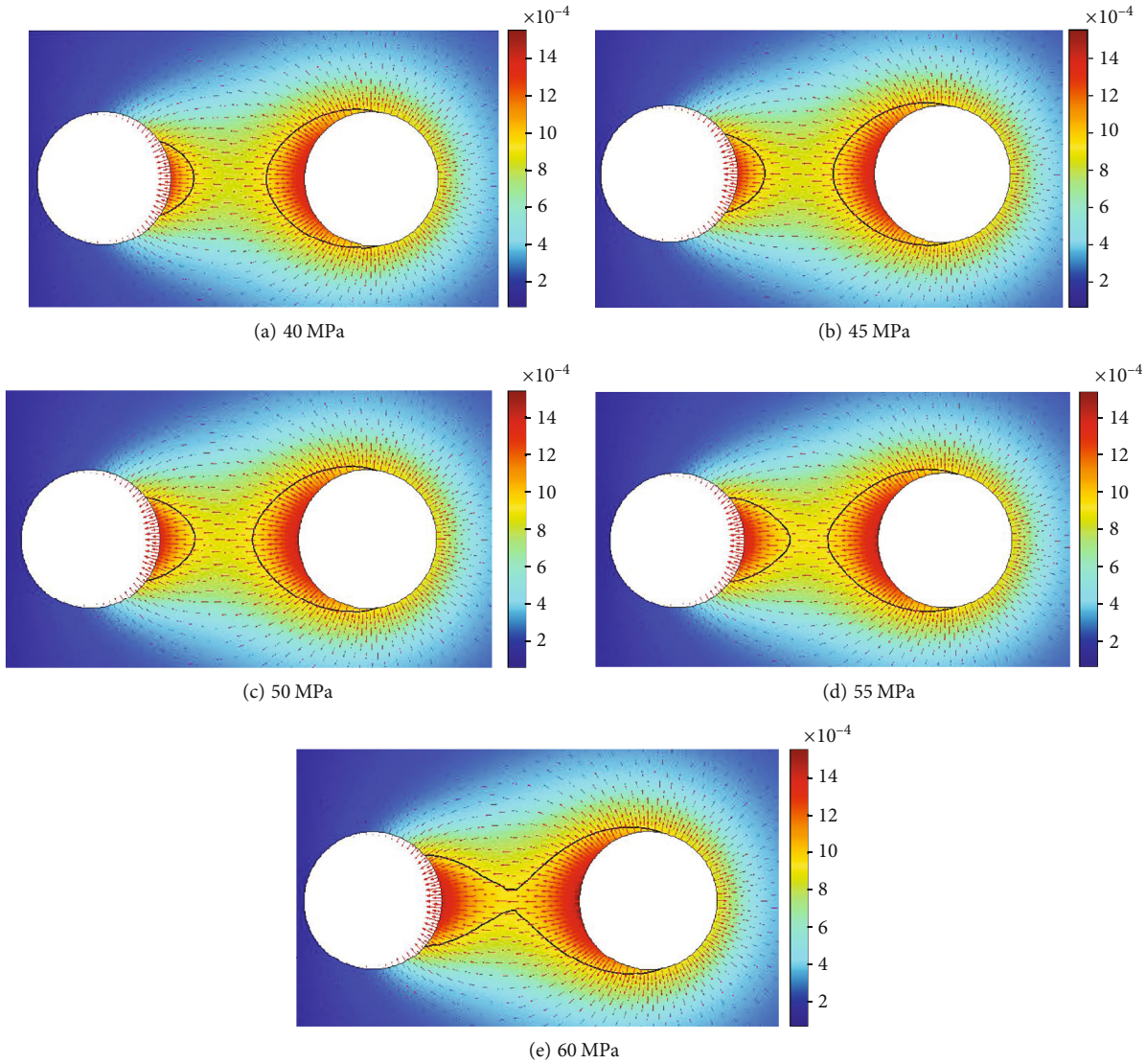

Figure 8: Velocity distribution after excavation of different explosion loads (unit: m/s).

25 MPa, and 30 MPa), the influences of geostress on the damage field and seepage field of surrounding rocks after tunnel excavation were estimated.

Figure 10 presents the nephogram of damage for surrounding rocks after blasting excavation under different geostress conditions. When geostress is too small, the damage zone protrudes towards the karst cave, while with the enhancement of geostress, surrounding rocks are located in a more compact state, and crack closure of surrounding rocks appears. Seepage pressure exerts a smaller effect compared with geostress, so the joint effect of damage and seepage reduces. The damage zone tends to be annularly distributed.

As shown in Figure 11, the change in geostress leads to obvious changes in the range of the damage zone and damage degree. The relationship between geostress, the range of the damage zone, and the damage degree can be characterized by the changes in the damage variable at measurement point A and the maximum damage range at the right side of the tunnel, as displayed in Figure 11. With the increase in

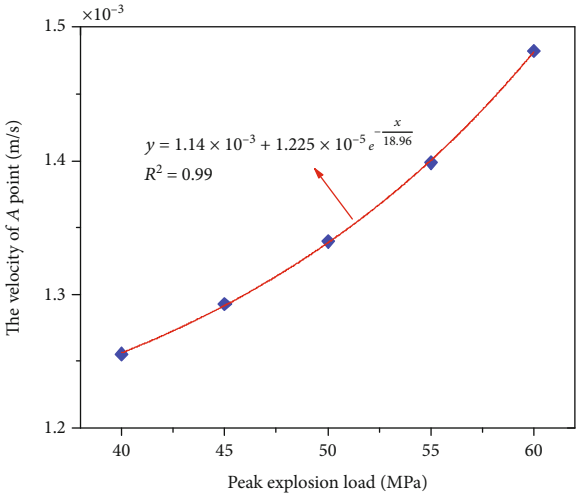

Figure 9: The relationship between the velocity change of point A and the explosion load.

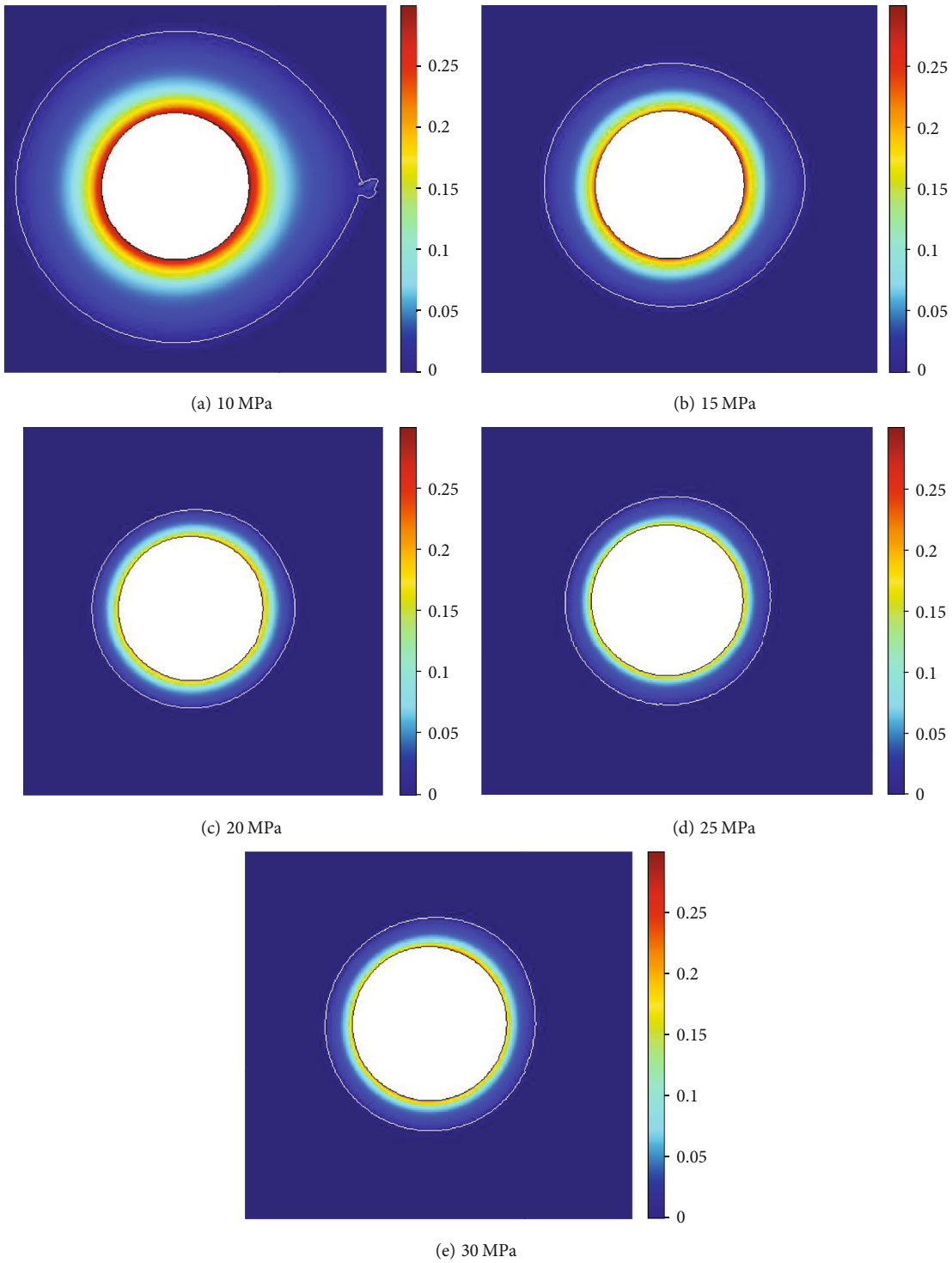

Figure 10: Distribution of surrounding rock damage after excavation under different geostress.

geostress, blasting-induced damage diminishes gradually, while unloading-induced damage increases little by little. When geostress is above 20 MPa, unloading-induced damage is higher than blasting-induced damage. In the process that geostress is increasing to 25 MPa, total damage, and damage range keep continues to increase. As geostress increases from 25 MPa to 30 MPa, total damage, and damage range show a small amplitude of increase.

Figure 12 demonstrates the nephogram of the flow velocity distribution after excavation under different geostresses. When geostress is too small, seepage zone A realizes the coalescences between the karst cave and the tunnel from left to right. With the increase of geostress, the range of seepage zone A continues to shrink. When geostress reaches 20 MPa, the left-to-right coalescence of seepage zone A is broken off. In the case that geostress increases from 25 MPa

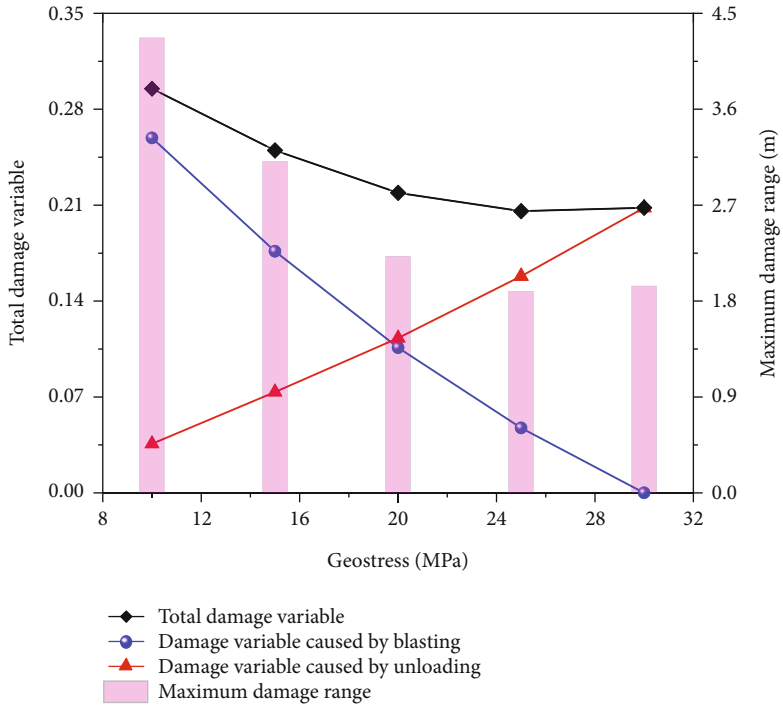

Figure 11: Damage of surrounding rock after excavation in different geostress.

to 30 MPa, the range of seepage zone A begins to enlarge in a small amplitude.

Figure 13 exhibits the change in flow velocity at measurement point A of the tunnel after excavation under various geostresses. As geostress increases from 10 MPa to 25 MPa, the flow velocity at the right-side wall of the tunnel decreases from 1.70×10^{-3} m/s to 1.30×10^{-3} m/s; when geostress increases to 30 MPa, the flow velocity again increases to 1.31×10^{-3} m/s.

3.3. Influence of Water Pressure on the Karst Cave. Different water pressures of the karst cave are prone to cause differences in seepage pressures of surrounding rocks. This affects both the damage and crack opening processes of surrounding rocks during the tunnel excavation process, finally influencing the seepage field distribution of surrounding rocks. By establishing the tunnel excavation models under different water pressures (0 MPa, 5 MPa, 10 MPa, 15 MPa, and 20 MPa) of the karst cave, the influences of the water pressure in the karst cave on damage field and seepage field distribution of surrounding rocks after excavation were investigated.

Figure 14 demonstrates the nephogram of the surrounding rock damage after excavation under different water pressures in the karst cave. When the water pressure in the karst cave is 0 MPa, the seepage conditions surrounding the left and right sides of the tunnel are the same, and the damage zone of surrounding rocks is shown to be annularly distributed; however, with the increase in the water pressure of the karst cave, the damage zone protrudes to the right side. This is because, with the increasing water pressure of the karst cave, the surrounding rocks at the right-side wall of the tunnel suffer the increasing effect of high seepage pressure, which promotes the openness and development of cracks on surrounding rocks. As a result, large damage occurs to surrounding rocks. The range and degree of the damage of surrounding rocks at the boundary of the tunnel increase with rising water pressure of the karst cave.

The relationship between the water pressure in the karst cave, the range, and the degree of damage can be characterized by the changes in the damage variable at measurement point A and the maximum damage range at the right side of the tunnel, as shown in Figure 15. Increasing water pressure in the karst cave can intensify blasting-induced damage and reduce unloading-induced damage. Its effect on the blasting-induced damage is shown to be larger, making the total damage at measurement point A, and the damage range of surrounding rocks larger.

Figure 16 is the nephogram of the flow velocity distribution after excavation under different water pressures in the karst cave. When the water pressure in the karst cave is small, there is no obvious seepage phenomenon in the surrounding rocks. As the water pressure reaches 10 MPa, seepage zone A appears, and its range rapidly enlarges with a small increase of the water pressure. When the water pressure lives up to 15 MPa, seepage zone A between the karst cave and the tunnel coalesces.

Figure 17 shows the change in flow velocity at measurement point A after excavation under different water pressures in the karst cave. When the water pressure in the karst cave increases from 0 MPa to 20 MPa, the flow velocity at measurement point A nearly increases from 0 to 3.1×10^{-3} m/s; the flow velocity exhibits an approximately linear increase with water pressure.

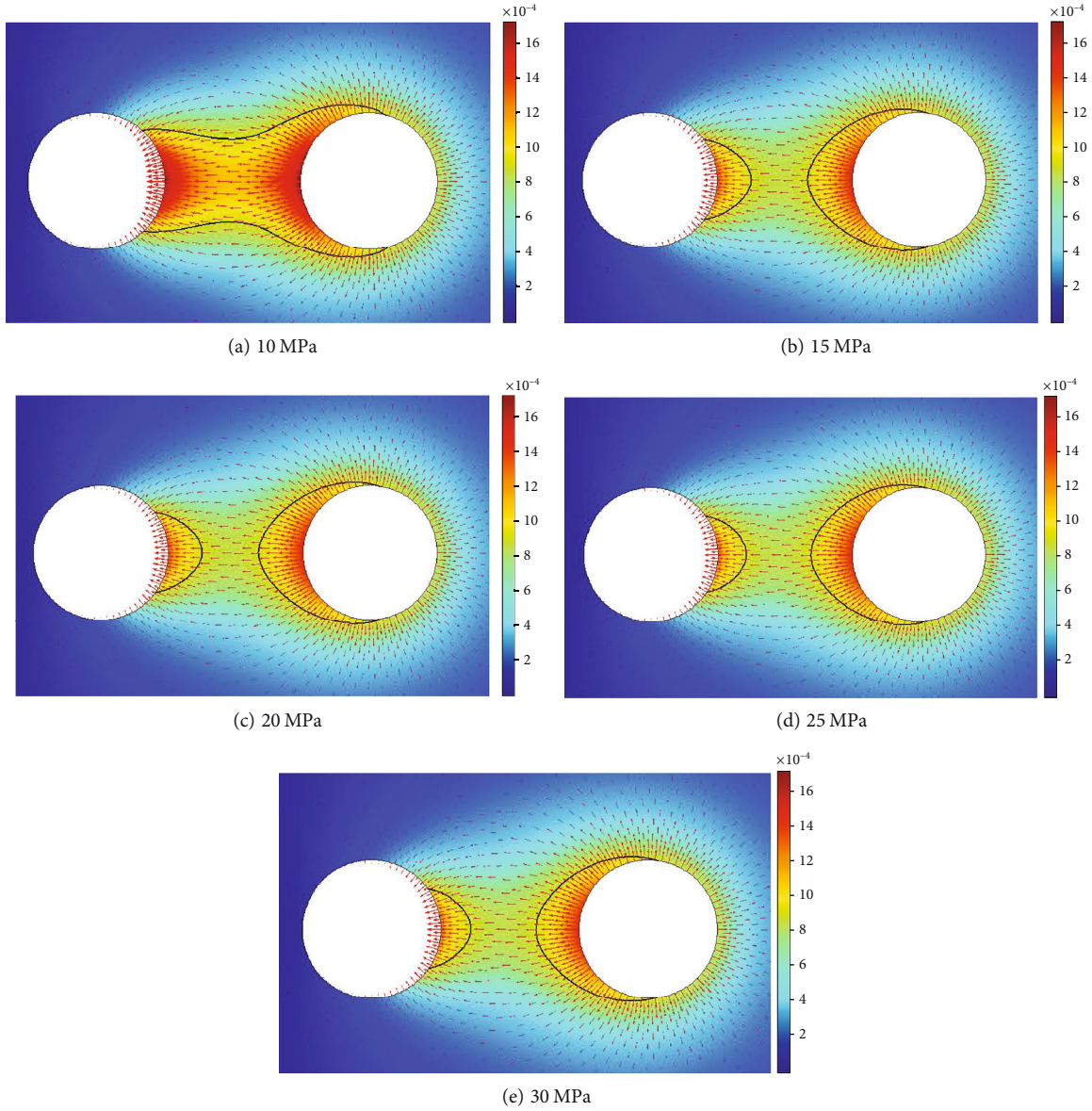

Figure 12: Velocity distribution of surrounding rock after excavation under different geostress (unit: m/s).

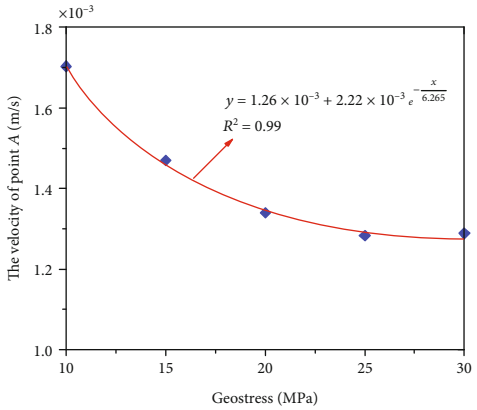

Figure 13: The relationship between the velocity change of point A and the geostress.

3.4. Interactive Relationship between the Damage Field and Seepage Field. The analysis aforementioned has demonstrated the damage field and seepage field distribution characteristics of surrounding rocks after blasting excavation under different explosive loads, geostresses, and water pressures in the karst cave. The analysis results indicate that water pressure has an important effect on the damage distribution of surrounding rocks during the excavation process. Meanwhile, the blasting excavation process can cause a change in pore water pressure and thus affect the distribution of the damage field. The damage effect will further lead the surrounding rock cracks to develop, inducing expansion of the seepage channels, and consequently changing the flow velocity in surrounding rocks. The relationship between the damage at measurement point A (and the damage range on the right sides of the tunnel) and flow velocity is shown in Figure 18.

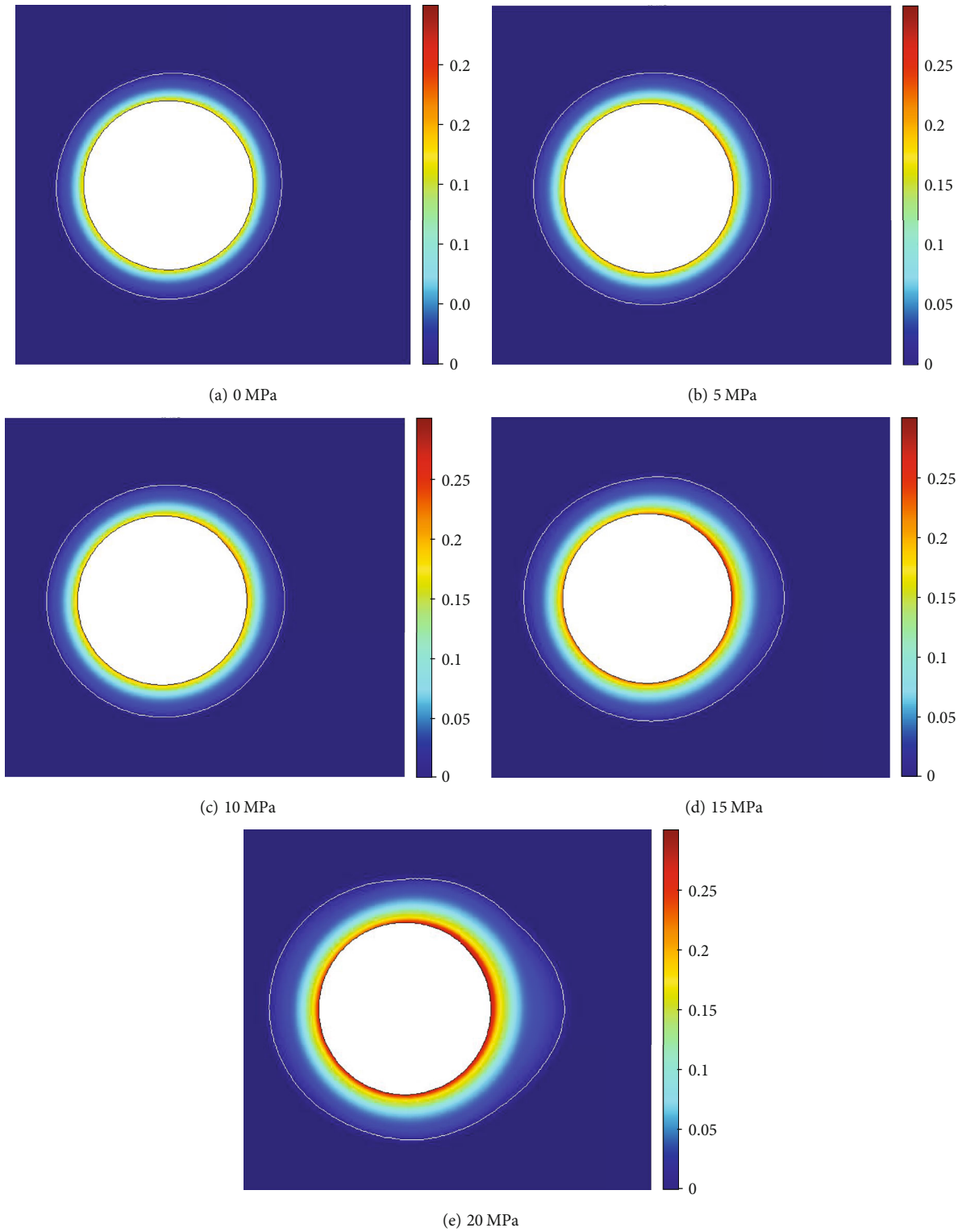

Figure 14: Damage distribution of surrounding rock after excavation under different water pressures.

The calculation results under different explosive loads and geostresses indicate that the increases in the range and degree of damage can increase the flow velocity in surrounding rocks. Under varying water pressures, according to Darcy's law, increasing water pressure in the karst cave can directly increase the flow velocity of surrounding rocks around the tunnel and cause increasing damage while indirectly inducing rising flow velocity. Meanwhile, according to Bernoulli's equation, changes in the flow velocity of surrounding rocks also cause a change in water pressure, which further affects the damage field distribution. Such a complex coupled effect leads to the formation of a seepage field and

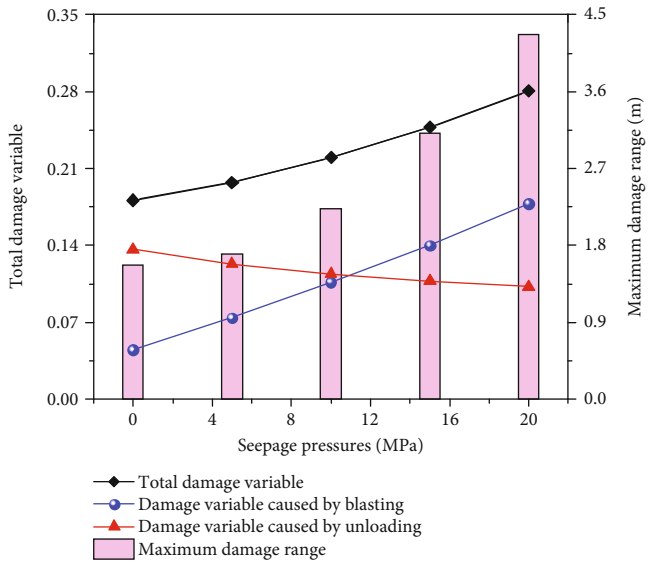

Figure 15: Damage of excavation surrounding rock under different water pressure of karst cave.

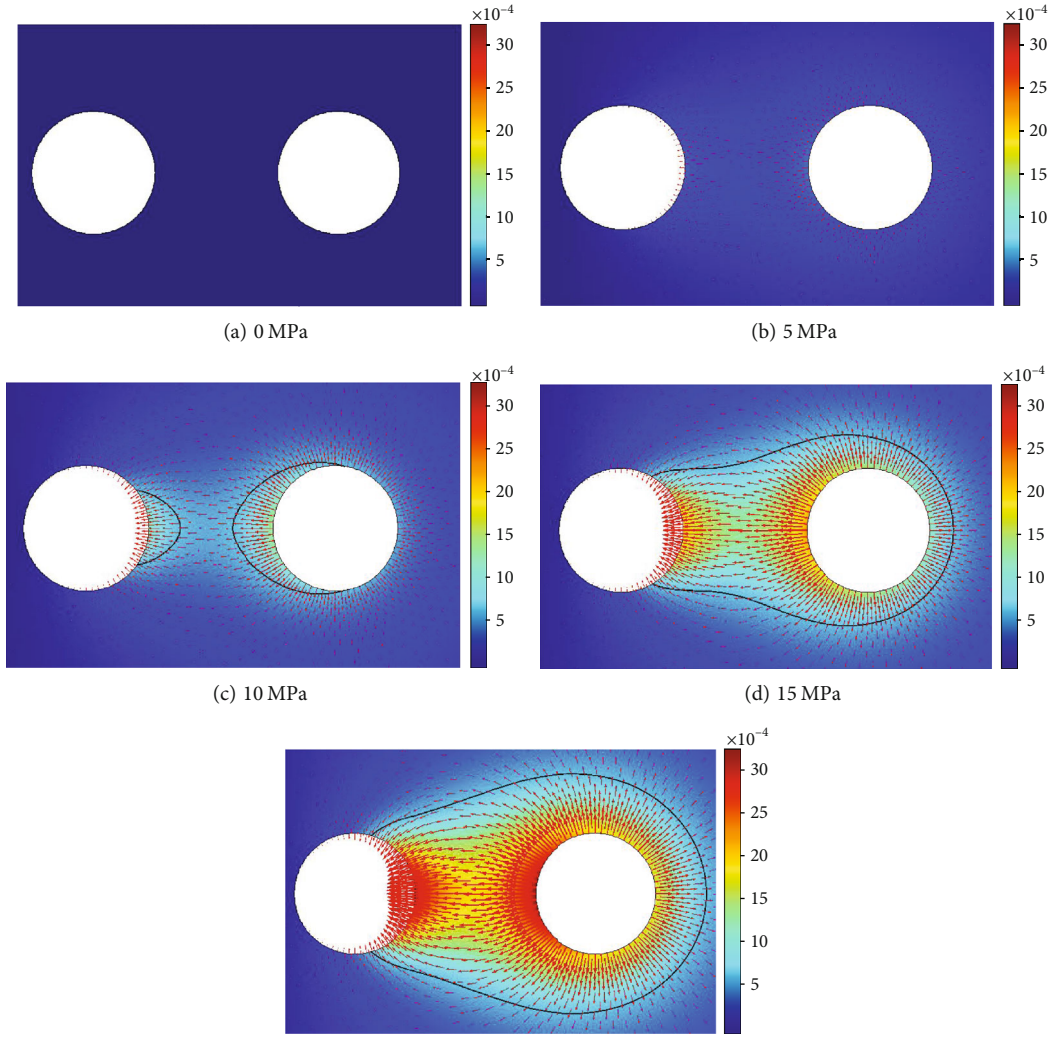

(a) 0 MPa

(b) 5 MPa

(c) 10 MPa

(d) 15 MPa

(e) 20 MPa

Figure 16: Velocity distribution of different karst caves after water pressure excavation (unit: m/s).

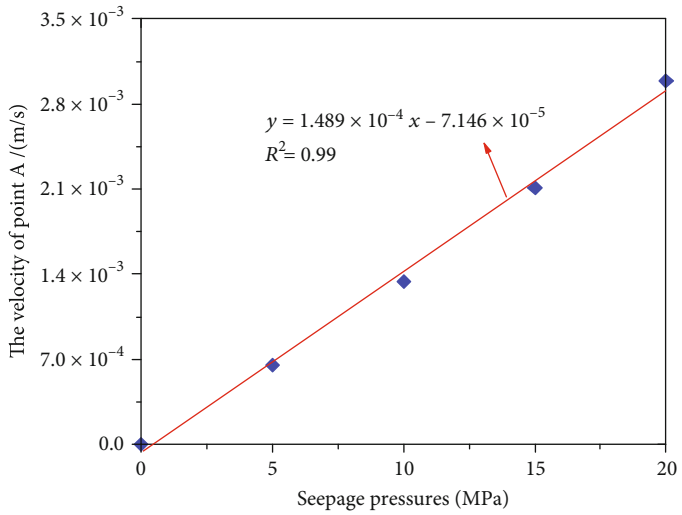

Figure 17: The relationship between the velocity change of point A and water pressure of karst cave.

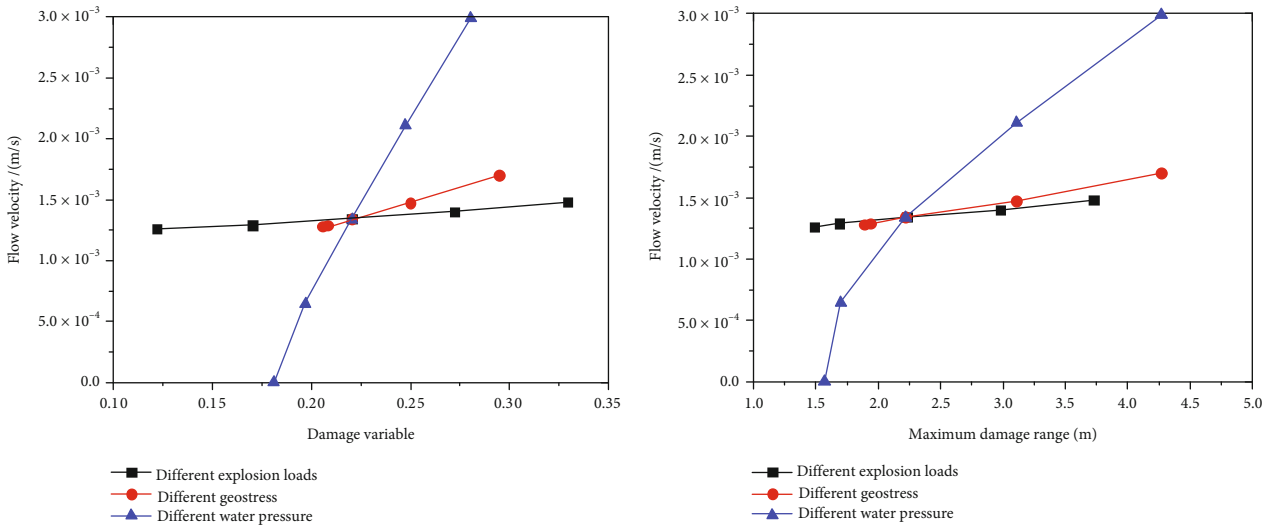

(a) Damage variable

(b) Maximum damage range

Figure 18: Relation curve between velocity and damage of measuring point A.

damages the field distribution of surrounding rocks after excavation.

4. Conclusion

This research took the blasting excavation of a deeply buried karst tunnel in the North Tianshan Mountains in China as research object. On this basis, a multifield coupled model for blasting excavation in the deeply buried rock tunnel was established to explore the damage induced by blasting excavation in the karst tunnel and the seepage characteristics of surrounding rocks under high geostress. The conclusion can be drawn as follows:

(1) Damage of surrounding rocks is attributed to the joint effects of blasting impact and transient unloading of geostress. The damage variable time-history curve shows a step-like increase: the increasing stage in the first step is found to be the blasting load impacting stage (blasting damage stage); the damage at the second step occurs after the impact of blasting load is fulfilled (unloading damage stage). The increase of geostress can weaken the blasting-induced effect on rock mass while enhancing the unloading-induced damage to rock mass; when geostress is above 20 MPa, unloading-induced damage is higher than blasting-induced damage; the increases in water pressure of karst caves can reduce unloading-induced

damage to rock while strengthening blasting-induced damage to rock

(2) The increases in blasting load and water pressure of karst caves are prone to cause increases in the degree and range of damage to surrounding rocks, while also leading to the increasing flow velocity of karst water between the tunnel and the karst cave; when geostress is below 25 MPa, the increasing geostress will decrease the damage to surrounding rocks after blasting excavation and the overall water flow velocity of karst water; however, when geostress exceeds 25 MPa, the enhancement of geostress can increase the surrounding rock damage and the overall water velocity of karst water

(3) In the blasting excavation process of the deeply-buried karst tunnel, there is a strong damage and seepage coupled effect. With further increases in the degree of damage to surrounding rocks and water pressure of karst caves, the coupled effect is enhanced gradually. Meanwhile, the right side (adjacent to the karst cave) of the tunnel exhibits a larger degree and range of damage to surrounding rocks compared with that of the left side. The damage zone protrudes to the right, leading to a greater water flow velocity of surrounding rocks after excavation, and the flow velocity increases nearly linearly with the increase of water pressure. In addition, there is a positive correlation between the damage field and seepage field of the surrounding rock under blasting

Data Availability

Data is available on request.

Conflicts of Interest

We declare that there are no known competing financial interests or personal relationships that could have appeared to influence the work reported in this paper.

Acknowledgments

This work was supported by the National Natural Science Foundation of China (No. 51979208), the Hubei Provincial Key Laboratory of Blasting Engineering, Jianghan University (HKLBEF202005), the Science and Technology Research and Development Program of China National Railway Group Corporation Limited (K2021G024), and the National Key Research and Development Project of China (2021YFC3100804).

References

[1] X. F. Huo, X. Z. Shi, X. Y. Qiu et al., "A study on raise blasting and blast-induced vibrations in highly stressed rock masses," *Tunnelling and Underground Space Technology*, vol. 123, article 104407, 2022.

[2] Y. Luo, G. Wang, X. Li et al., "Analysis of energy dissipation and crack evolution law of sandstone under impact load," *International Journal of Rock Mechanics and Mining Sciences*, vol. 132, article 104359, 2020.

[3] C. Zhu, Y. Z. Xu, Y. X. Wu et al., "A hybrid artificial bee colony algorithm and support vector machine for predicting blast-induced ground vibration," *Earthquake Engineering and Engineering Vibration*, vol. 21, no. 4, pp. 861–876, 2022.

[4] F. L. Pellet, M. Keshavarz, and M. Boulon, "Influence of humidity conditions on shear strength of clay rock discontinuities," *Engineering Geology*, vol. 157, pp. 33–38, 2013.

[5] C. Zhu, X. D. Xu, X. T. Wang et al., "Experimental investigation on nonlinear flow anisotropy behavior in fracture media," *Geofluids*, vol. 2019, Article ID 5874849, 9 pages, 2019.

[6] Q. Yin, J. Y. Wu, Z. Jiang et al., "Investigating the effect of water quenching cycles on mechanical behaviors for granites after conventional triaxial compression," *Geomechanics and Geophysics for Geo-Energy and Geo-Resources*, vol. 8, no. 2, p. 77, 2022.

[7] Y. T. Li, B. Zhang, L. Wang, Y. Wu, H. X. Wang, and Z. H. Peng, "Identification of dominant seepage channels in fractured rock masses of underground water–sealed oil storage: a case study," *Bulletin of Engineering Geology and the Environment*, vol. 81, no. 9, p. 357, 2022.

[8] S. B. Tang, J. M. Li, S. Ding, and L. T. Zhang, "The influence of water-stress loading sequences on the creep behavior of granite," *Bulletin of Engineering Geology and the Environment*, vol. 81, no. 11, p. 482, 2022.

[9] D. M. Tan, T. Y. Qi, and Y. C. Mo, "Numerical analysis and research on surrounding rock stability of lateral karst cave tunnel," *Chinese Journal of Rock Mechanics and Engineering*, vol. 28, no. S2, pp. 3497–3503, 2009.

[10] L. P. Li, W. F. Tu, Z. Q. Zhou, S. S. Shi, M. G. Zhang, and Y. X. Chen, "Dynamic unloading instability mechanism of underground cavern based on seepage-damage coupling," *KSCE Journal of Civil Engineering*, vol. 24, no. 5, pp. 1620–1631, 2020.

[11] B. Liu, J. L. Li, Q. S. Liu, and X. W. Liu, "Analysis of damage and permeability evolution for mudstone material under coupled stress-seepage," *Materials*, vol. 13, no. 17, p. 3755, 2020.

[12] C. H. Huang, W. H. Dong, Z. Z. Cao et al., "Water inrush mechanism of fault zone in karst tunnel under fluid-solid coupling field considering effective stress," *Geofluids*, vol. 2022, Article ID 4205174, 11 pages, 2022.

[13] H. L. Zhao, F. Zhang, and X. P. Yao, "Hydromechanical simulation of tunnel excavation in rock considering a nearby karst cave," *Mathematical Problems in Engineering*, vol. 2021, Article ID 7875725, 13 pages, 2021.

[14] W. M. Yang, X. Yang, Z. D. Fang et al., "Model test for water inrush caused by karst caves filled with confined water in tunnels," *Arabian Journal of Geosciences*, vol. 12, no. 24, pp. 1866–7511, 2019.

[15] H. Yuan, C. Chen, Z. He, and Y. Wang, "Numerical simulation of fluid-solid coupling in surrounding rock for river stope mining," *Shock and Vibration*, vol. 2020, Article ID 9786182, 11 pages, 2020.

[16] J. Q. Guo, J. X. Chen, F. Chen, Y. B. Luo, and Q. Liu, "Water inrush criterion and catastrophe process of a karst tunnel face with non-persistent joints," *China Journal of Highway and Transport*, vol. 31, no. 10, pp. 118–129, 2018.

[17] Z. Huang, Z. Jiang, S. Zhu, X. Wu, L. Yang, and Y. Guan, "Influence of structure and water pressure on the hydraulic

conductivity of the rock mass around underground excavations," *Engineering Geology*, vol. 202, pp. 74–84, 2016.

[18] Z. Huang, S. Y. Zhu, K. Zhao et al., "Influences of structural variation of host rock induced by engineering activities on water inrush of tunnels," *Chinese Journal of Geotechnical Engineering*, vol. 40, no. 3, pp. 449–458, 2018.

[19] J. X. Wang and A. N. Jiang, "An elastoplastic damage constitutive model of rock and its application to tunnel engineering," *Rock and Soil Mechanics*, vol. 36, no. 4, pp. 1147–1158, 2015.

[20] W. C. Zhu, C. H. Wei, J. Tian, T. H. Yang, and C. A. Tang, "Coupled thermal hydraulic-mechanical model during rock damage and its preliminary application," *Rock and Soil Mechanics*, vol. 30, no. 12, pp. 3851–3857, 2009.

[21] Y. Luo, X. P. Li, P. C. Xu, Q. Dong, and J. S. Hong, "Characteristic study of surrounding rock mass deformation considering accumulative damage effect," *Rock and Soil Mechanics*, vol. 35, no. 11, pp. 3041–3048, 2014.

[22] X. P. Li, B. Wang, and G. L. Zhou, "Reserch on distribution rule of geostress in deep stratumin in Chinese mainland," *Chinese Journal of Rock Mechanics and Engineering*, vol. 31, no. S1, pp. 2875–2880, 2012.

[23] Y. Luo, H. L. Gong, D. X. Qu et al., "Vibration velocity and frequency characteristics of surrounding rock of adjacent tunnel under blasting excavation," *Scientific Reports*, vol. 12, no. 1, p. 8453, 2022.

[24] M. Chen, W. B. Lu, P. Yan, and Y. G. Hu, "Blasting excavation induced damage of surrounding rock masses in deep-buried tunnels," *KSCE Journal of Civil Engineering*, vol. 20, no. 2, pp. 933–942, 2016.

[25] L. P. Li, S. C. Li, S. S. Shi, Z. L. Zhou, M. Guo, and Q. H. Wang, "Multi-field coupling mechanism of seepage damage for the water inrush channel formation process of coal mine," *Journal of Mining and Safety Engineering*, vol. 29, no. 2, pp. 232–238, 2012.

Hindawi
Geofluids
Volume 2023, Article ID 2455954, 10 pages
https://doi.org/10.1155/2023/2455954

Research Article

A New Mode of Visible Fracture System in Coal Seams and Its Implications for Coalbed Methane Seepage

Rui Li,[1] **Lihong Jin**,[1] **Shengwei Wang**,[2] **Heping Liu**,[3] **Zhigang Cui**,[4] **and Wenting Xiang**[1]

[1]*State Key Laboratory of Coal Mine Disaster Dynamic and Control, Chongqing University, Chongqing 400044, China*
[2]*School of Earth Resources, China University of Geosciences, Wuhan 430074, China*
[3]*Department of Geological Survey, Lu'An Chemical Group Co., LTD., Changzhi 046000, China*
[4]*Shijiazhuang Coal Mine, Lu'An Chemical Group Co., LTD., Yangquan 045000, China*

Correspondence should be addressed to Rui Li; ruilicug@hotmail.com

Received 13 November 2022; Revised 12 December 2022; Accepted 18 March 2023; Published 11 April 2023

Academic Editor: Yiding Bao

As the central flow channel for fluid seepage through rock layers, the visible fracture system (VFS) significantly affects geoenergy extraction for petroleum, natural gas, geothermal resources, and greenhouse gas sequestration. In this work, we propose a new mode of VFS in coal seams, including hydraulic fractures, exogenetic fractures, interlayer fractures, gas-expanding fractures, and cleats. The development characteristics of VFSs in coal seams are analyzed, including containing their geometry, orientation, scale, distribution, and connection between each other. Furthermore, the implications of the VFS for fluid (gas and water) and solid (coal fines) flow through coal seams are discussed. The development of the VFS determines the effective flow conductivity, affecting the flow of gas, water, and coal fines. Additionally, as the reservoir pressure transfer channel, the VFS significantly influences depressurization with reservoir depletion, determining the extension of the methane desorption range. The exogenetic fractures and interlayer fractures dominate the expansion of the primary hydraulic fractures, and gas-expanding and cleats usually control the branch of hydraulic fractures. Furthermore, we find that the daily production rate distribution of most CBM wells presents a particular banded, L-shaped, or T-shaped pattern. It is thought that the VFS dominates the productivity of CBM in coal seams. The field production data also provide evidence that the occurrence of the VFS makes the CBM reservoir heterogeneous. This study presents a recommended framework involving the characteristics of the VFS and its influences on CBM production.

1. Introduction

Coal seams are typically fractured reservoirs. The fracture system provides the central flow channels for fluid migration through rock layers, affecting geoenergy extraction for petroleum, natural gas, geothermal resources, and greenhouse gas sequestration [1]. More than 80% of coalbed methane (CBM) exists in the coal matrix pores in an adsorption state. By extracting the formation water from coal seams, the fluid pressure decreases to the critical desorption pressure. The adsorbed methane in the coal matrix pores releases and diffuses to the fracture network system and flows to the wellbore [2–4]. The visible fracture system (VFS) in coal seams provides the channels for CBM flow and plays an essential role in CBM production [5]. Therefore, it is of great significance for the efficient extraction of CBM to study the characteristics and implications of the VFS on the CBM seepage [6–8].

Along with the exploration and development of CBM, researchers have intensively studied natural fracture systems in coal seams in the last 30 years. The endogenetic fractures in CBM reservoirs, called cleats, including face cleats and butt cleats, are widely used in coal reservoir evaluation. The two cleats are nearly perpendicular to each other and perpendicular to the stratification of coal seams. Compared to butt cleats, face cleats are more developed and more continuous [9, 10]. The natural fracture system in some coal seams is complicated because of the complex tectonism, various tectonic periods, and intense deformation. Various natural fractures exist in these coal seams [11, 12]. Therefore,

the cleats used to describe the natural fracture system in coal seams are limited and cannot accurately represent the occurrence of fractures. Some researchers have investigated and proposed fracture categories based on the geological conditions of China. According to the generation and development characteristics of the fractures, fractures in coal seams can be divided into four levels: large fractures, medium fractures, minor fractures, and microfractures, as shown in Figure 1 [13]. Large and medium fractures are equivalent to exogenetic joints and are the product of the deformation of coal seams. They can develop in any position in coal seams, and the height is several meters. Minor fractures usually intersect with stratification at high angles, extending from several millimeters to several centimeters. Microfractures often develop in vitrain coal and bright coal, and the height is generally several millimeters to several centimeters.

Coal seam fractures can also be divided into horizontal fractures, vertical fractures, and oblique fractures with an angle to the coalbed, depending on the relationship between the exogenetic fractures and the stratification [14]. The inherited fractures are the retransformation of the previously formed cleats, with the mixed properties of cleats and exogenetic fractures, and belong to the transitional type. Wang et al. [15] proposed a mode of VFS based on field investigations in the Ordos Basin and Qinshui Basin, North China. The VFS includes exogenetic fractures, gas-expanding fractures, and cleats. Within the VFS, significant differences in both the geometry and spatial distribution are observed.

The VFS in coal seams controls the permeability of coal seams, which has significant implications for CBM production [8]. For example, the VFS in coal seams plays a substantial role in the design and effect of directional horizontal wells [16, 17]. The developed structural fracture system in coal seams with high connectivity has high permeability, high reservoir pressure transmission efficiency, and high productivity [18]. The heterogeneity of coal seams caused by the VFS controlled by stress is an essential factor affecting the productivity of CBM wells. The development degree and opening of natural fractures maintain heterogeneity in the permeability [19–21]. The development characteristics of macroscopic fractures in coal seams differ in different coal body structures. Although the number and density of fractures in severely broken coal are large, the fracture connectivity becomes extremely poor due to tectonism, which cannot contribute to the production of CBM [22]. Therefore, fracture development is an important reason why tectonically deformed coal cannot contribute to CBM production [23]. Although previous researchers have studied the development characteristics of VFSs with many achievements, they have not yet constructed a geological model of natural VFSs closely related to CBM development [24]. Therefore, it is necessary to closely combine CBM development and VFSs to perform further studies.

The purpose of this work is to investigate the characteristics of a new mode of VFS and its significant implications for CBM production. The VFS is proposed depending on in situ observations in the subsurface coal mines and field tests. The VFS is divided into subclasses, and the development characteristics are analyzed based on the field investigations. Then, the implications of the VFS for CBM production are discussed. This study is aimed at providing necessary theoretical guidance for exploring and developing CBM resources and coal mine gas extraction.

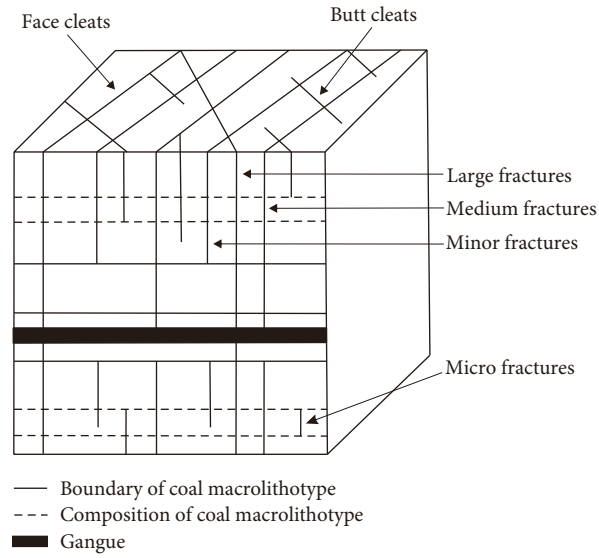

Figure 1: Classification of coal seam fractures [13].

2. A New Mode of VFS in Coal Seams

The subsurface in situ observations of coal seams in coal mines show that coal seams generally develop VFSs. The VFS can be identified by the naked eye, including exogenetic fractures, interlayer fractures, gas-expanding fractures, and cleats. Through in situ observations of coal seams, the development characteristics of VFSs are as follows.

2.1. Hydraulic Fractures. Understanding the fracture geometry, scale, and distribution of hydraulic fracturing can provide a reference for evaluating the hydraulic fracturing effect of CBM wells and optimizing the target fracturing zone and fracturing process.

In situ observation of the hydraulic fractures exposed in the coal mining process is employed to understand the occurrence of hydraulic fractures in coal seams. The results show that there are three types of hydraulic fractures in CBM reservoirs, namely, vertical fractures, horizontal fractures, and T-type fractures (Figure 1). The fracture length is generally from 10 to 30 m, and the height varies from 2 m to 5 m [22]. The width is usually less than 10 cm. In addition, the surfaces of vertical hydraulic fractures are rough and uneven. However, the surfaces of horizontal hydraulic fractures are smooth and flat.

In addition, most hydraulic fractures are only developed in undeformed coal and cataclastic coal and are rarely distributed in fragmented coal and mylonitic coal [25–27]. For undeformed coal seams, hydraulic fractures have a large scale, but the number of fractures is small. However, in tectonically deformed coal, the number of hydraulic fractures is

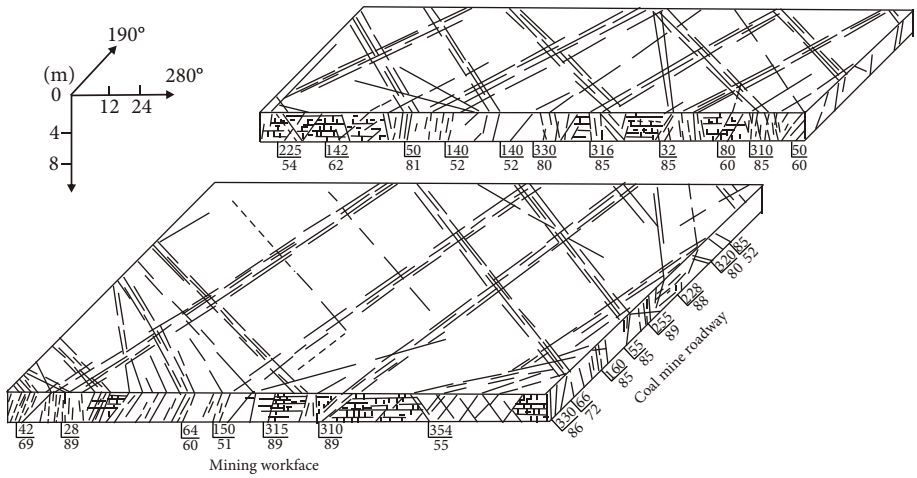

Figure 2: Exogenetic fractures in coal seams in the southern Qinshui Basin (revised from [15]).

greater than that in undeformed coal, but the size of the fractures is smaller.

2.2. Exogenetic Fractures. Exogenetic fractures are formed by tectonic stress action on coal seams, and their occurrence is usually matched with high-level faults or folds. This kind of fracture exists widely in coal seams. They intersect with the stratifications at various angles, and their occurrence generally agrees with the direction of nearby faults. Exogenetic fractures can develop in any part of coal seams [28]. The surfaces of exogenetic fractures usually have uneven sliding traces, mostly displaying feathery, wavy but also relatively smooth features. Fillings such as multistage limestone and clay minerals are often found in exogenetic fractures, which explains why these fractures are the main channels for internal and external fluid exchange. Based on in situ observations in coal mines, the distribution characteristics of exogenetic fractures in coal seams are shown in Figure 2.

2.3. Interlayer Fractures. As the sedimentary environment changes in the coal formation process, several gangue layers usually develop within coal seams. The thickness of each gangue is generally not more than 10 centimeters, and the distribution along coal seams is stable. Because of the significant difference in rock lithology between gangue and coal, the interface between gangue and coal can form a weak cohesive zone, which can develop interlayer fractures. Additionally, interlayer fractures also exist along the stratification within coal seams. False roofs can develop between the coal seam and roof, which are generally carbonaceous shale with a thickness of tens of centimeters. Due to the low mechanical strength of false roofs, interlayer fractures can be distributed in the false roofs. In the coal mining process, coal easily falls off along the interlayer, which also demonstrates that the existence of interlayer fractures makes the coal seam adhesion very weak.

2.4. Gas-Expanding Fractures. The morphology and scale of gas-expanding fractures are similar to those of exogenetic fractures, while the occurrence and surface pattern are very similar to those of cleats. Preliminary studies have shown that these kinds of fractures are tensile and formed by the outward expansion of fluids during CBM formation. Gas-expanding fractures significantly influence the rock physical properties of coal seams and have symbolic significance for the formation, enrichment, and preservation of CBM reservoirs. Gas-expanding fractures are usually seen in bright and semibright coal. The height is generally between several centimeters and tens of centimeters but is not developed or poorly developed in dull coal (Figure 3).

2.5. Cleats. Cleats in coal seams are also termed endogenetic fractures. There are apparent equal or nearly equal distances among cleats (Figure 3). Cleats are perpendicular to the bedding plane, with a flat surface pattern, and sometimes are filled with minerals. Cleats are formed by the internal tension caused by the changes in the internal structure and uniform shrinkage of the gelation material influenced by the variations in the temperature and pressure in coal during coalification. Therefore, the development of cleats is mainly restricted in vitrain coal, and cleats are commonly distributed in bright coal and semibright coal. The cleats in middle-rank coal are the most developed, with 30 to 40 cleats within 5 centimeters, sometimes up to 50 or 60. Cleats are usually not developed in low- and high-rank coal, generally less than 15 within 5 centimeters.

The categories and characteristics of the VFS in coal seams are listed in Table 1.

3. Discussion on the Implications of the VFS for CBM Production

3.1. Flow Channels of CBM, Formation Water, and Coal Fines. The development characteristics of VFSs significantly determine the difficulty of CBM seepage within reservoirs. VFSs with high density, good connectivity, large width, and long extension distance are more conducive to the seepage and output of gas and formation water. Large amounts of fractures are developed in tectonically deformed coal because of the intense stress action. However, the mechanical properties of tectonically deformed coal are sharply weakened due to damage to the coal body. The fractures

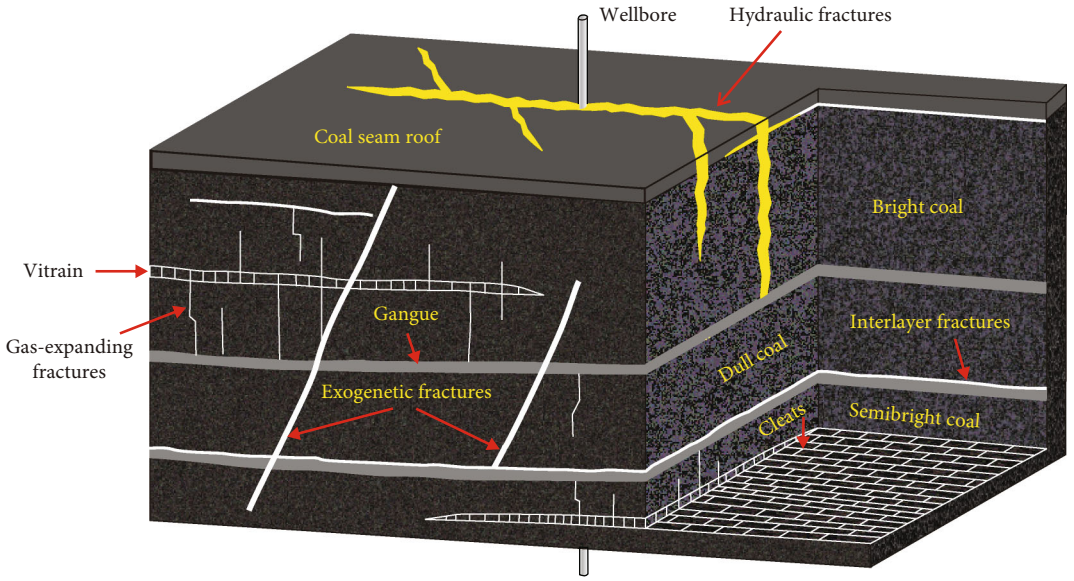

Figure 3: Sketch of the VFS in coal seams.

Table 1: VFS classification in coal seams.

Channel type	Distribution positions	Space extent range	Connection role	Level
Hydraulic fractures	Around the wellbore	A few meters to tens of meters	Wellbore, exogenetic fractures, and interlayer fractures	I
Exogenetic fractures	Any positions of coal seams	A few meters to hundreds of meters	Hydraulic fractures, interlayer fractures, and gas-expanding fractures	II
Interlayer fractures	Gangue, roof, interlayers	A few meters to hundreds of meters [29]	Connect hydraulic fractures, exogenetic fractures	III
Gas-expanding fractures	Bright coal and semibright coal [15]	Several centimeters to tens of centimeters	Connect hydraulic fractures, exogenetic fractures, and cleats	IV
Cleats	Specular coal and bright coal [30]	Several millimeters to several centimeters	Connect the microfractures in the coal matrix	V

are short and narrow and are filled with many carbonate rocks or clay minerals. Effective fractures that widely communicate with the wellbore are challenging to form. These unconnected fractures in tectonically deformed coal can hinder the seepage of coal seam fluids, which restricts the production volume of CBM wells. Therefore, although the VFS is developed in tectonically deformed coal, the flow conductivity is not strong.

The VFS is also the main channel of coal fine migration during CBM production. The precondition that coal fines migrate into the wellbore is that the fractures have good connectivity. The coal fines produced by CBM wells mainly come from the primary coal fines [31, 32]. There are two main occurrence places. One is in the stratification above the soft coalbed, and the other is in the fracture system connected with the tectonic coal inside the coal body. Most coal fines move into the wellbore through the VFS, with a small amount entering the wellbore directly [33]. Due to the tortuous characteristics of the VFS, the coal fines produced by vertical wells are from the fractures near the wellbore and the fracture channel. Whether there is a soft coalbed around the wellbore is crucial in creating coal fines. The coal fines are relatively developed and quickly produced if they pass through the tectonism-developed zone. For horizontal CBM wells, the migration channel of coal fines mainly depends on the horizontal borehole. Suppose they pass through the nearly vertical tectonism-broken area. In that case, the horizontal well can directly collapse and expand the hole, and the coal fines are relatively easy to separate and migrate through the horizontal well [17]. If the soft coalbed is located above the horizontal branch of the horizontal CBM wells, the horizontal borehole easily collapses, which will also cause the output of coal fines [34, 35]. Therefore, CBM horizontal wells produced more coal fines than CBM vertical wells.

3.2. Determination of the Reservoir Permeability and Transmission of the Reservoir Pressure and Gas Desorption Range. Permeability represents the conductivity of CBM reservoirs. Effective permeability is conducive to the output of CBM. The effective permeability of CBM reservoirs is determined by the development degree of the VFS in coal seams. As unconventional natural gas, CBM reservoirs generally have low permeability. Reservoir permeability is generally

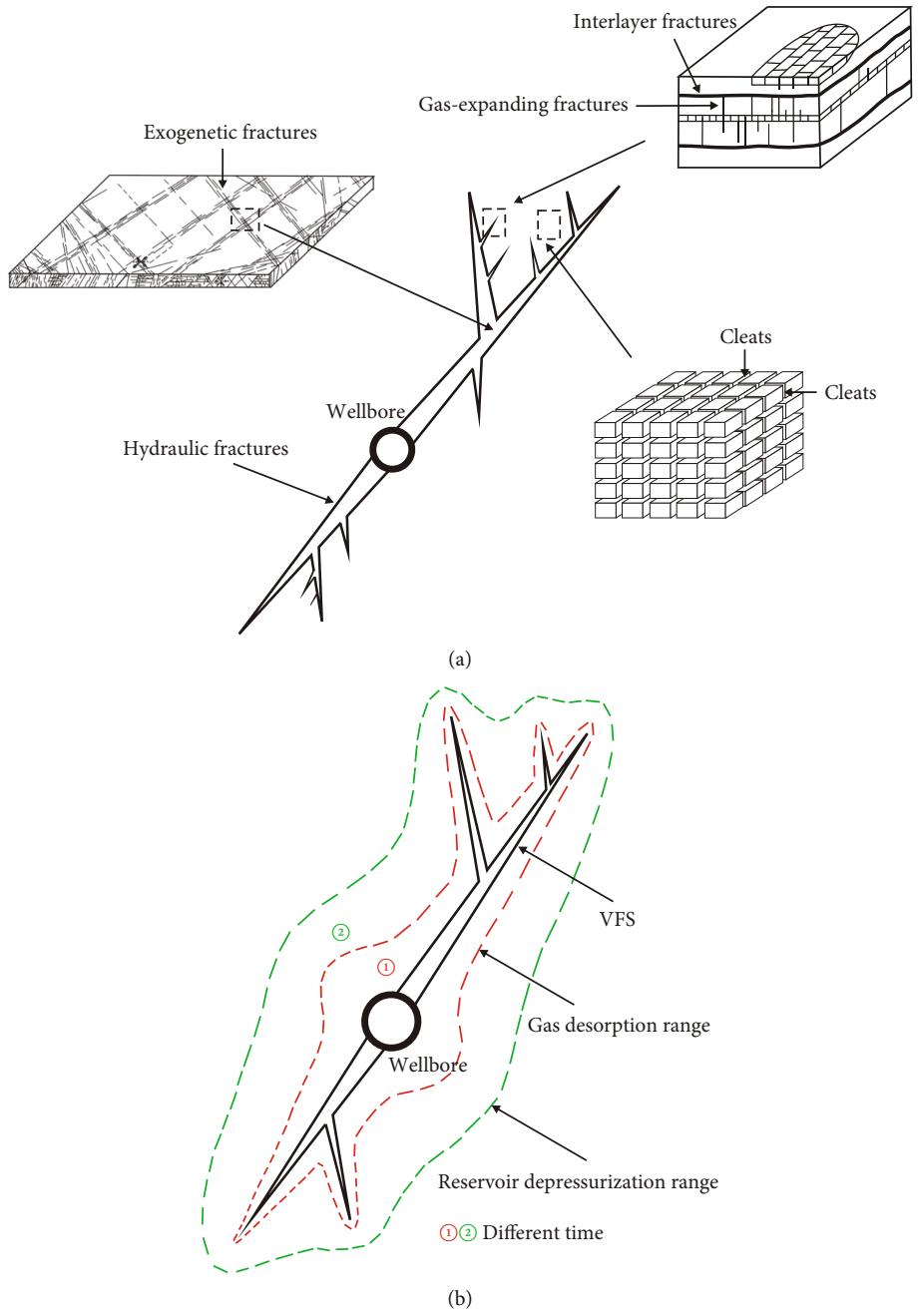

Figure 4: Transmission of reservoir pressure and gas desorption range (revised from [43]): (a) reservoir pressure transmission in VFS; (b) variations of reservoir depressurization and gas desorption range in the horizontal section.

obtained by testing coal seam samples in the laboratory. However, the sample permeability has difficulty reflecting the effective permeability of CBM reservoirs, as the laboratory conditions dramatically differ from the actual geological conditions. For areas with in situ observation conditions, coal seam permeability can be directly analyzed by observation and measurement. The relationship between the surrounding rock and VFS in coal seams can be obtained through surface structural joint mapping if the VFS cannot be directly observed. The development characteristics and permeability of the VFS in coal seams can also be analyzed [36].

In addition, the permeability of the VFS will change with the output of CBM. In the dewatering stage and gas-water two-phase flow stage, the fluid pressure in the VFS decreases. The fractures are gradually closed under effective stress, and the coal seam permeability is decreased [37–39]. In the stable gas production stage and declining gas production stage, due to the matrix shrinkage effect, the fracture width and coal seam permeability both increase [40–42].

In the process of reservoir depletion, the VFS in coal seams provides spaces for pressure transmission. Therefore, the development of the VFS, mainly hydraulic fractures and exogenetic fractures, significantly impacts the depressurization

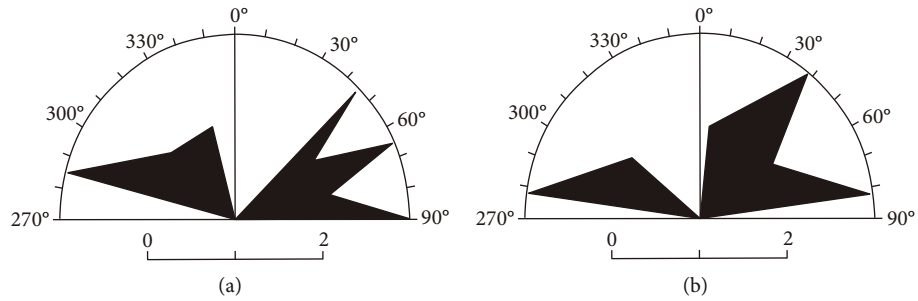

Figure 5: Relationship between the orientation of principal stress and vertical fractures in Sihe mine: (a) maximum principal stress direction; (b) vertical fracture direction.

range. The coal seam pressure drop is propagated along the VFS and changes in the temporal and spatial dimensions.

In CBM production, the basic transmission modes of the reservoir pressure include water transfer and gas transfer [43]. In the early dewatering stage, the produced water mainly comes from hydraulic fractures and exogenetic fractures (Figure 4(a)), where water transmission mainly occurs. Due to the high permeability of the VFS in coal seams and the rapid pressure drop, this stage is generally short. At the gas-water two-phase flow stage, the water production rate gradually decreases while the gas production rate gradually increases. Therefore, the water transmission in the VFS is slowly weakened, and the gas transmission is slowly enhanced. In the stable gas production stage, the pressure transmission in the VFS is almost entirely contributed by gas transmission rather than water transmission.

With the decreased reservoir pressure, the methane in the coal matrix desorbs continuously, and the gas desorption range gradually expands around the VFS, as shown in Figure 4(b). The range and degree of reservoir pressure transmission in CBM production determine the gas desorption range of CBM. Therefore, the geometry, scale, and strike of the VFS in the coal seam significantly affect the distribution of the gas desorption range.

3.3. Interaction between Hydraulic Fractures and the Natural VFS. The underground observations show that the vertical fracture orientation is generally consistent with the VFS. For example, the direction of the exogenetic fractures in the Sihe and Chengzhuang coal mines, North China, is NEE and NWW, as shown in Figure 5. This indicates that the orientation of vertical hydraulic fractures is consistent with that of the principal stress in this area, which is NEE and NWW. As the regional tectonic stress controls the development of the exogenetic fracture system, the orientation of hydraulic fractures is also generally consistent with that of the regional tectonic stress [44]. In addition, the underground observation of hydraulic fractures shows that the horizontal hydraulic fractures mainly extend along the interlayer fractures of the VFS in coal seams [45]. In our opinion, the fracturing fluids injected into the formation preferentially extend along the exogenetic fractures and interlayer fractures due to the weak cementing strength in these fractures [46, 47]. Therefore, our field observations and field test results can explain this phenomenon.

The exogenetic fractures and interlayer fractures significantly affect the expansion of the central hydraulic fractures, and the gas-expanding fractures and cleats usually control the branch of hydraulic fractures (Figure 4). In addition, if the gas-expanding fractures and cleats are very developed, fracturing fluids could leak off, and high fluid pressure is lost. This is why fracturing fluids easily leak off during fracturing in the coal seam. Furthermore, the scale of hydraulic fracture propagation is significantly limited, and the stimulation effect is obviously reduced.

3.4. Influences on the Productivity Distribution of CBM Wells. The VFS in coal seams largely determines the heterogeneity of CBM reservoirs [48, 49]. To understand the relationship between VFS development and the productivity of gas wells, the distribution characteristics of CBM well productivity are investigated. The study area is located in the Jincheng mining area, the southern Qinshui Basin, North China. Coal seams in the study area are nearly horizontal. The thickness of the coal seam is large with an average value of more than 5 m. The burial depth of the coal seam is less than 800 m. In the study area, the VFS is developed, especially the large exogenous fractures and gas-expanding fractures. There are hundreds of typical CBM production wells located in this area, which provide abundant production data for the research of productivity distribution.

The maximum daily gas production is one of the crucial parameters to characterize the productivity of CBM wells. In addition, the total gas production volume and average gas production volume are difficult to obtain, as the production time and the production stage of these CBM wells differ. Therefore, the parameter of maximum gas production was employed for the statistical analysis. Our study indicates that the maximum daily gas production of CBM wells has pronounced directivity, with a bounded-type, L-type, and T-type pattern (Figure 6). We find that the maximum daily production of adjacent wells usually differs. Furthermore, for any development area, no more than five adjacent wells will have close maximum daily gas production. Therefore, the direction of the maximum daily production distribution of wells is closely related to the development of the VFS.

We think that the types of productivity distribution of CBM wells are closely related to the geometry, scale, and orientation of VFSs with different levels. The maximum daily production distribution of a bounded-type CBM well is

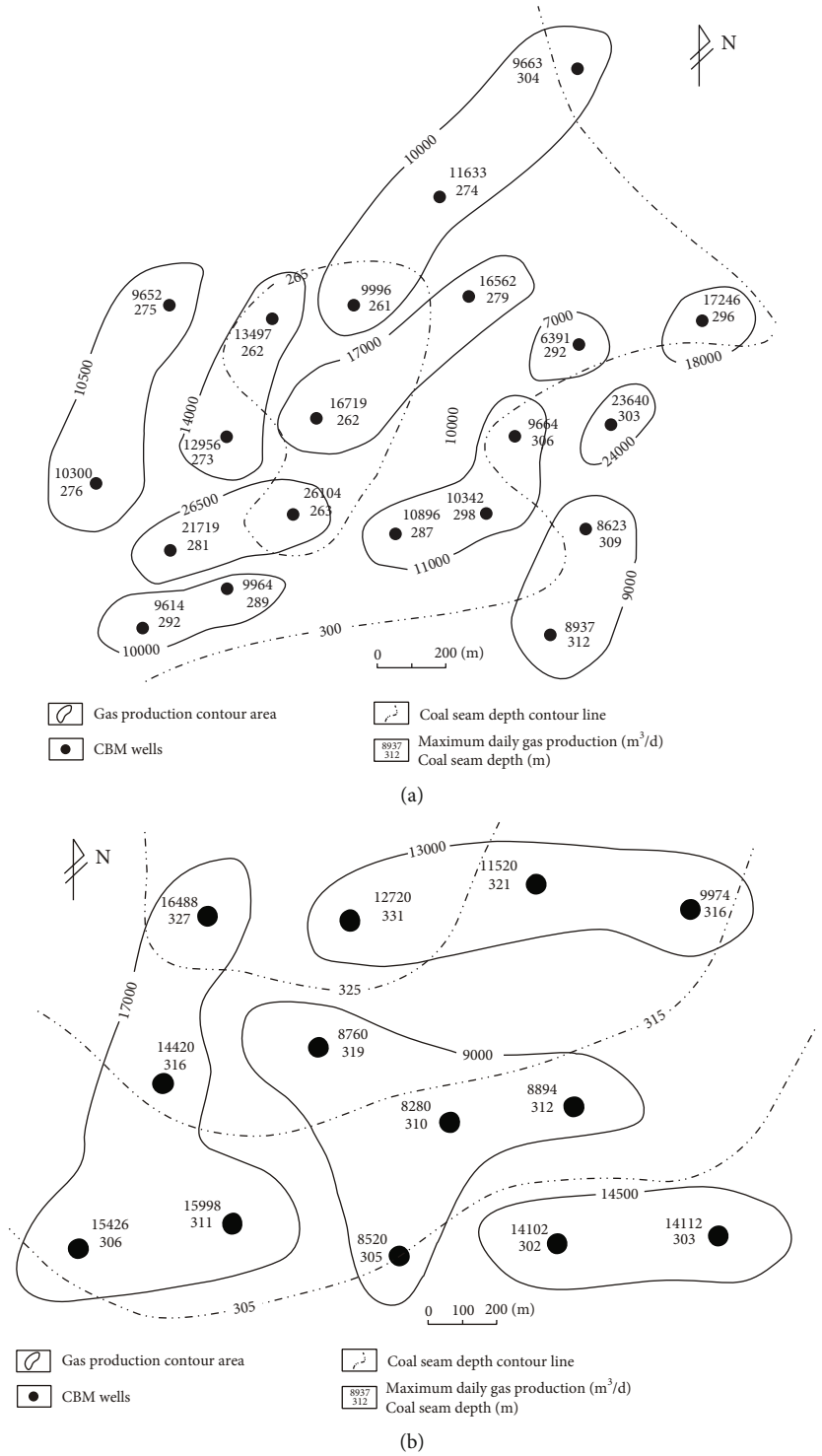

Figure 6: Coal seam maximum dairy production distribution: (a) bounded type; (b) L-type and T-type.

determined by the dominant direction of the hydraulic fractures and exogenetic fractures. The distribution of the maximum daily gas production in a T-type CBM well shows that two large-scale fractures are developed and well connected (Figure 6(b)), such as exogenetic fractures. The distribution of the maximum daily gas production in an L-type CBM well shows that gas-expanding fractures are connected in two directions (Figure 6(a)) [50]. In addition, the maximum daily production of a few CBM wells is significantly different from that of the surrounding gas wells, which means that the wellbore does not communicate with a large-scale VFS.

Therefore, drilling holes should be arranged in areas where the VFS develops, leading to good connectivity. Moreover, where there are CBM wells, infill wells enhancing gas production should be arranged in the VFS along with nearby high-yield gas wells.

4. Conclusions

According to the in situ observations and field tests, a new mode of VFS is proposed. Furthermore, the development characteristics of the VFS and its influences on CBM production are discussed. The main achievements in this work are as follows.

Depending on the geometry, orientation, scale, distribution, and connectivity characteristics, the VFS in coal seams can be divided into five subclasses, including hydraulic fractures, exogenetic fractures, interlayer fractures, gas-expanding fractures, and cleats. The VFS provides the channel for the migration of CBM, formation water, and coal fines. It determines the flow conductivity of reservoirs and controls the propagation of the reservoir pressure and the gas desorption range. The propagation of hydraulic fractures is affected by the development of exogenous fractures. We find that the exogenetic fractures and interlayer fractures dominate the expansion of the central hydraulic fractures, and gas-expanding fractures and cleats usually control the branch of hydraulic fractures. The VFS influences the productivity distribution for CBM wells, with a banded, L-shaped, or T-shaped pattern. This indicates that the development of the VFS shows the strong heterogeneity of coal seams.

This study presents a theoretical foundation for understanding the development characteristics of artificial and natural fractures in coal seams and their influences on gas flow. Furthermore, our work guides the selection of favorable CBM blocks and CBM exploitation.

Data Availability

The data used to support the findings of this study are included within the article.

Conflicts of Interest

The authors declare that they have no conflict of interest.

Acknowledgments

This research was supported by the National Natural Science Foundation of China (nos. U19B2009 and 52204125), Science and Technology Think Tank Young Talent Program (no. 20220615ZZ07110307), and the National Science and Technology Major Project of China (no. 2016ZX05067001-007). In addition, special thanks are due to PetroChina Huabei Oilfield Company for providing the production data of CBM wells. These supports are gratefully acknowledged.

References

[1] C. Zhu, X. D. Xu, X. T. Wang et al., "Experimental investigation on nonlinear flow anisotropy behavior in fracture media," *Geofluids*, vol. 2019, Article ID 5874849, 9 pages, 2019.

[2] Y. Li, C. Zhang, D. Tang, Q. Gan, X. Niu, and R. Shen, "Coal pore size distributions controlled by the coalification process: an experimental study of coals from the Junggar, Ordos and Qinshui basins in China," *Fuel*, vol. 206, pp. 352–363, 2017.

[3] Z. J. Pan and D. A. Wood, "Coalbed methane (CBM) exploration, reservoir characterisation, production, and modelling: a collection of published research (2009-2015)," *Journal of Natural Gas Science and Engineering*, vol. 26, pp. 1472–1484, 2015.

[4] A. Salmachi and Z. Yarmohammadtooski, "Production data analysis of coalbed methane wells to estimate the time required to reach to peak of gas production," *International Journal of Coal Geology*, vol. 141-142, pp. 33–41, 2015.

[5] Y. L. Liu, H. Xu, D. Z. Tang et al., "The impact of the coal macrolithotype on reservoir productivity, hydraulic fracture initiation and propagation," *Fuel*, vol. 239, pp. 471–483, 2019.

[6] I. Karakurt, G. Aydin, and K. Aydiner, "Sources and mitigation of methane emissions by sectors: a critical review," *Renewable Energy*, vol. 39, no. 1, pp. 40–48, 2012.

[7] Y. Li, Z. Wang, S. Tang, and D. Elsworth, "Re-evaluating adsorbed and free methane content in coal and its ad- and desorption processes analysis," *Chemical Engineering Journal*, vol. 428, article 131946, 2022.

[8] T. Wang, W. R. Hu, D. Elsworth et al., "The effect of natural fractures on hydraulic fracturing propagation in coal seams," *Journal of Petroleum Science and Engineering*, vol. 150, pp. 180–190, 2017.

[9] S. E. Laubach, R. A. Marrett, J. E. Olson, and A. R. Scott, "Characteristics and origins of coal cleat: a review," *International Journal of Coal Geology*, vol. 35, no. 1-4, pp. 175–207, 1998.

[10] P. Mostaghimi, R. T. Armstrong, A. Gerami et al., "Cleat-scale characterisation of coal: an overview," *Journal of Natural Gas Science and Engineering*, vol. 39, pp. 143–160, 2017.

[11] M. Q. Li, J. Lu, and S. Xiong, "Prediction of fractures in coal seams with multi-component seismic data," *Scientific Reports*, vol. 9, no. 1, p. 6488, 2019.

[12] T. A. Moore, "Coalbed methane: a review," *International Journal of Coal Geology*, vol. 101, pp. 36–81, 2012.

[13] X. H. Fu, *Physical and Numerical Simulations of Physical Properties of Multiphase Medium Coal Rocks or Reservoirs*, China University of Mining and Technology, 2001.

[14] X. B. Su, Y. L. Feng, and J. F. Chen, "The classfication of fractures in coal," *Coal Geology & Exploration*, vol. 30, pp. 21–24, 2002.

[15] S. W. Wang, G. J. Hou, M. Zhang, and Q. P. Sun, "Analysis of the visible fracture system of coalseam in Chengzhuang Coalmine of Jincheng City, Shanxi Province," *Chinese Science Bulletin*, vol. 50, no. S1, pp. 45–51, 2005.

[16] J. R. Gilman, J. L. Bowzer, and B. W. Rothkopf, "Application of short-radius horizontal boreholes in the naturally fractured Yates field," *SPE Reservoir Engineering*, vol. 10, no. 1, pp. 10–15, 1995.

[17] J. Y. Zhang, Q. H. Feng, X. M. Zhang et al., "Multi-fractured horizontal well for improved coalbed methane production in eastern Ordos Basin, China: field observations and numerical simulations," *Journal of Petroleum Science and Engineering*, vol. 194, article 107488, 2020.

[18] Y. Xue, F. Gao, Y. N. Gao et al., "Quantitative evaluation of stress-relief and permeability-increasing effects of overlying coal seams for coal mine methane drainage in Wulan coal mine," *Journal of Natural Gas Science and Engineering*, vol. 32, pp. 122–137, 2016.

[19] C. Sun, H. Zheng, W. D. Liu, and W. T. Lu, "Numerical simulation analysis of vertical propagation of hydraulic fracture in

bedding plane," *Engineering Fracture Mechanics*, vol. 232, article 107056, 2020.

[20] S. B. Tang, J. M. Li, S. Ding, and L. T. Zhang, "The influence of water-stress loading sequences on the creep behavior of granite," *Bulletin of Engineering Geology and the Environment*, vol. 81, no. 11, p. 482, 2022.

[21] Q. Yin, J. Y. Wu, Z. Jiang et al., "Investigating the effect of water quenching cycles on mechanical behaviors for granites after conventional triaxial compression," *Geomechanics and Geophysics for Geo-Energy and Geo-Resources*, vol. 8, no. 2, p. 77, 2022.

[22] R. Li, S. W. Wang, S. F. Lyu, W. Lu, G. F. Li, and J. C. Wang, "Geometry and filling features of hydraulic fractures in coalbed methane reservoirs based on subsurface observations," *Rock Mechanics and Rock Engineering*, vol. 53, no. 5, pp. 2485–2492, 2020.

[23] Y. Cheng and Z. Pan, "Reservoir properties of Chinese tectonic coal: a review," *Fuel*, vol. 260, article 116350, 2020.

[24] A. Batwara, J. Y. Wang, and I. D. Gates, "Ultrarefined model of a coal bed methane reservoir: connectivity and implications for production," *Journal of Petroleum Science and Engineering*, vol. 217, article 110901, 2022.

[25] R. Li, S. W. Wang, G. F. Li, and J. C. Wang, "Influences of coal seam heterogeneity on hydraulic fracture geometry: an in situ observation perspective," *Rock Mechanics and Rock Engineering*, vol. 55, no. 7, pp. 4517–4527, 2022.

[26] P. Tan, H. W. Pang, R. X. Zhang et al., "Experimental investigation into hydraulic fracture geometry and proppant migration characteristics for southeastern Sichuan deep shale reservoirs," *Journal of Petroleum Science and Engineering*, vol. 184, article 106517, 2020.

[27] P. Tan, X. L. Hu, Y. Jin, and S. A. Fu, "Observation of hydraulic fracture morphology for laboratory experiments by using multiple methods," *Geotechnical and Geological Engineering*, vol. 39, no. 7, pp. 4997–5005, 2021.

[28] Z. Z. Wang, J. N. Pan, Q. L. Hou, B. S. Yu, M. Li, and Q. H. Niu, "Anisotropic characteristics of low-rank coal fractures in the Fukang mining area, China," *Fuel*, vol. 211, pp. 182–193, 2018.

[29] Q. L. Le, P. Chen, and W. M. Yang, "The relation between modes of lithologic association and interlayer-gliding structures in coal mine," *Journal of Coal Science and Engineering (China)*, vol. 16, no. 1, pp. 47–52, 2010.

[30] Y. Li, S. Pan, S. Ning, L. Shao, Z. Jing, and Z. Wang, "Coal measure metallogeny: metallogenic system and implication for resource and environment," *Science China Earth Sciences*, vol. 65, no. 7, pp. 1211–1228, 2022.

[31] T. H. Bai, Z. W. Chen, S. M. Aminossadati, Z. J. Pan, J. S. Liu, and L. Li, "Characterization of coal fines generation: a microscale investigation," *Journal of Natural Gas Science and Engineering*, vol. 27, pp. 862–875, 2015.

[32] X. Z. Zhao, S. Q. Liu, S. X. Sang et al., "Characteristics and generation mechanisms of coal fines in coalbed methane wells in the southern Qinshui Basin, China," *Journal of Natural Gas Science and Engineering*, vol. 34, pp. 849–863, 2016.

[33] W. L. Han, Y. B. Wang, J. J. Fan, Y. Li, X. Wu, and Y. Yu, "An experimental study on coal fines migration during single phase water flow," *Geofluids*, vol. 2020, Article ID 3974790, 13 pages, 2020.

[34] X. Liang, S. B. Tang, C. A. Tang, L. H. Hu, and F. Chen, "Influence of water on the mechanical properties and failure behaviors of sandstone under triaxial compression," *Rock Mechanics and Rock Engineering*, vol. 56, no. 2, pp. 1131–1162, 2023.

[35] Y. B. Xu, Y. S. Zhu, and P. H. Zhang, "Application of CBM horizontal well development technology in the roof strata close to broken-soft coal seams," *Natural Gas Industry B*, vol. 6, no. 2, pp. 168–174, 2019.

[36] Z. Zhang, M. Zhou, Y. X. Cao, B. A. Xian, and D. Gao, "The prediction of structural fractures in coal seams of the Kuba coalfield, China: an application for coalbed methane (CBM) recovery development," *Geologia Croatica*, vol. 72, no. Special issue, pp. 57–69, 2019.

[37] Y. D. Bao, J. P. Chen, L. J. Su, W. Zhang, and J. W. Zhan, "A novel numerical approach for rock slide blocking river based on the CEFDEM model: a case study from the Samaoding paleolandslide blocking river event," *Engineering Geology*, vol. 312, article 106949, 2023.

[38] Z. G. Tao, Q. Geng, C. Zhu et al., "The mechanical mechanisms of large-scale toppling failure for counter-inclined rock slopes," *Journal of Geophysics and Engineering*, vol. 16, no. 3, pp. 541–558, 2019.

[39] Y. Wang, C. Zhu, M. C. He, X. Wang, and H. L. Le, "Macro-meso dynamic fracture behaviors of Xinjiang marble exposed to freeze thaw and frequent impact disturbance loads: a lab-scale testing," *Geomechanics and Geophysics for Geo-Energy and Geo-Resources*, vol. 8, no. 5, p. 154, 2022.

[40] M. C. He, Q. R. Sui, M. N. Li, Z. J. Wang, and Z. G. Tao, "Compensation excavation method control for large deformation disaster of mountain soft rock tunnel," *International Journal of Mining Science and Technology*, vol. 32, no. 5, pp. 951–963, 2022.

[41] M. Y. Wei, C. Liu, Y. K. Liu et al., "Long-term effect of desorption-induced matrix shrinkage on the evolution of coal permeability during coalbed methane production," *Journal of Petroleum Science and Engineering*, vol. 208, article 109378, 2022.

[42] R. Yang, T. R. Ma, H. Xu, W. Q. Liu, Y. Hu, and S. Sang, "A model of fully coupled two-phase flow and coal deformation under dynamic diffusion for coalbed methane extraction," *Journal of Natural Gas Science and Engineering*, vol. 72, article 103010, 2019.

[43] R. Li, S. W. Wang, W. W. Chao, J. C. Wang, and S. F. Lyu, "Analysis of the transfer modes and dynamic characteristics of reservoir pressure during coalbed methane production," *International Journal of Rock Mechanics and Mining Sciences*, vol. 87, pp. 129–138, 2016.

[44] M. Q. Qin, D. S. Yang, W. Z. Chen, and S. Q. Yang, "Hydraulic fracturing model of a layered rock mass based on peridynamics," *Engineering Fracture Mechanics*, vol. 258, article 108088, 2021.

[45] S. F. Lyu, S. W. Wang, X. J. Chen et al., "Natural fractures in soft coal seams and their effect on hydraulic fracture propagation: a field study," *Journal of Petroleum Science and Engineering*, vol. 192, article 107255, 2020.

[46] H. H. Abass, M. L. Van Domelen, and E. I. Rabaa, "Experimental observations of hydraulic fracture propagation through coal blocks," in *SPE Eastern Regional Meeting*, pp. 239–252, Columbus, Ohio, 1990.

[47] L. K. Huang, J. J. Liu, F. S. Zhang, H. F. Fu, H. Y. Zhu, and B. Damjanac, "3D lattice modeling of hydraulic fracture initiation and near-wellbore propagation for different perforation models," *Journal of Petroleum Science and Engineering*, vol. 191, article 107169, 2020.

[48] L. Tian, Y. X. Cao, S. M. Liu, B. Shi, J. Z. Liu, and D. Elsworth, "Coalbed methane reservoir fracture evaluation through the novel passive microseismic survey and its implications on permeable and gas production," *Journal of Natural Gas Science and Engineering*, vol. 76, article 103181, 2020.

[49] C. Wang and J. G. Wang, "Effect of heterogeneity and injection borehole location on hydraulic fracture initiation and propagation in shale gas reservoirs," *Journal of Natural Gas Science and Engineering*, vol. 96, article 104311, 2021.

[50] S. W. Wang, R. Li, and Y. H. Xiao, *Coalbed methane drainage Engineering*, China University of Geosciences Press, Wuhan, China, 2019.

Hindawi
Geofluids
Volume 2023, Article ID 1652890, 7 pages
https://doi.org/10.1155/2023/1652890

Research Article

Rapid and Slow Unlocking-Induced Startup Mechanisms of Locked Segment-Dominated Landslides

Hongran Chen,[1,2] **Chao Xu**,[1,2,3] **Yuan Cui**,[1,2,3] **and Siqing Qin**[1,2,3]

[1]*Key Laboratory of Shale Gas and Geoengineering, Institute of Geology and Geophysics, Chinese Academy of Sciences, Beijing 100029, China*
[2]*Innovation Academy for Earth Science, CAS, Beijing 100029, China*
[3]*College of Earth and Planetary Sciences, University of Chinese Academy of Sciences, Beijing 100049, China*

Correspondence should be addressed to Siqing Qin; qsqhope@mail.iggcas.ac.cn

Received 9 September 2022; Accepted 10 October 2022; Published 24 March 2023

Academic Editor: Yiding Bao

Locked segment-dominated landslides initiate when locked segments are sufficiently damaged to be unlocked. The evolution of such slopes toward instability displays either an exponentially or stepwise accelerated displacement pattern, but the underlying mechanisms of these patterns are elusive. We show that the displacement pattern is governed by mechanical synergy (resistance homogenization) between the ruptured locked segment and the transfixion segment. Using a mechanical model, we demonstrate that rapid and slow resistance homogenizations, which depend mainly on the brittleness of locked segments, cause two unlocking-induced startup mechanisms that lead to loss of slope stability: one occurring at the peak-stress points and the other at the residual-strength points of the locked segments. Accordingly, the evolution toward instability exhibits one of the two abovementioned patterns. External factors, such as rainwater, can deteriorate the strength of geomaterials but hardly alter the inherent mechanical rules that a locked segment adheres to. These findings provide insights into the mechanism of locked segment-dominated landslides and pave the way for reliably predicting their occurrence.

1. Introduction

Many slopes worldwide are stabilized by locked segments, i.e., geological structures with high bearing capacity (determined by scale and strength) along potential slip surfaces [1, 2]. Such a slope becomes unstable only when a locked segment becomes unlocked (fails). Rock bridges [3] are the most common locked segments in rock slopes [4–6]. An example is the Yanchihe slope in Hubei, China (E117.298°, N31.208°, Figure 1(a), [7]). Locked segments also exist in Quaternary sedimentary slopes such as the Longxi slope (E100.883°, N36.102°, Figure 1(b), [8]) in the Longyangxia Reservoir area on the Yellow River.

Gradual damage of locked segments can cause growing displacement of the corresponding slopes. Therefore, a roughly unified displacement pattern is expected, and the quite different displacement patterns of the Yanchihe and Longxi slopes as they evolved toward instability are difficult to explain. The Yanchihe slope displaced with an exponentially accelerated trend (Figure 2(a), [7]), whereas the acceleration displacement of the Longxi slope was suspended and then resumed, thus exhibiting a stepwise accelerated curve (Figure 2(b), [8]). As both patterns are widely observed in locked segment-dominated landslides, uncovering their corresponding mechanisms is crucial for reliable landslide prediction. If the formations of these patterns remain elusive, then whether displacement acceleration of a locked segment-dominated slope indicates a forthcoming landslide cannot be correctly prejudged.

The transfixion of slip surfaces is either progressive or instantaneous, depending on the physical properties of materials on the slip surfaces [9, 10]. Accelerated cracking of a locked segment can result in an exponentially accelerated displacement curve [11] but cannot explain a stepwise accelerated curve. A stepwise accelerated displacement pattern is usually assumed to be derived from the pore-water

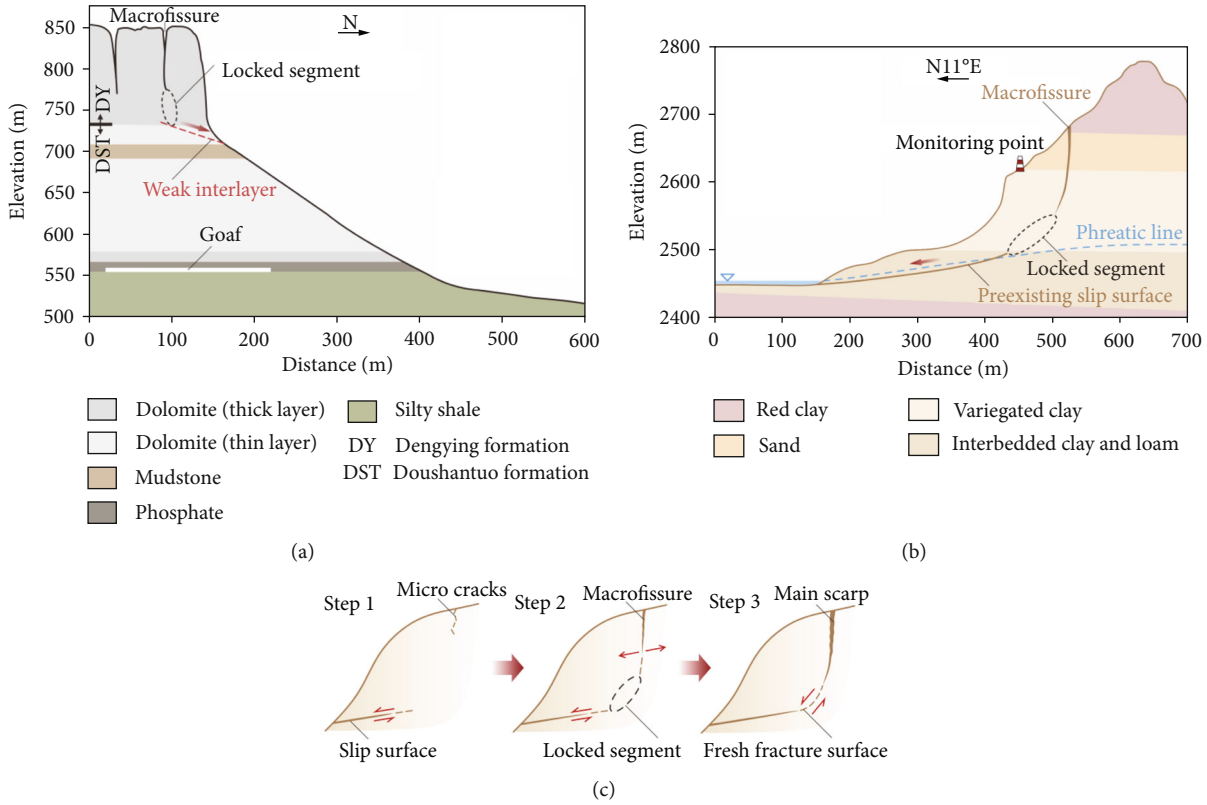

FIGURE 1: Geological profiles of the (a) Yanchihe [7] and (b) Longxi slopes [8], and (c) typical formation and failure processes of a locked segment. Step 1: a bottom slip surface develops or preexists. Step 2: tension cracks form a macrofissure with slope deformation, where the intact part between the fissure and bottom slip surface serves as a locked segment. Step 3: the locked segment becomes unlocked and landslide occurs.

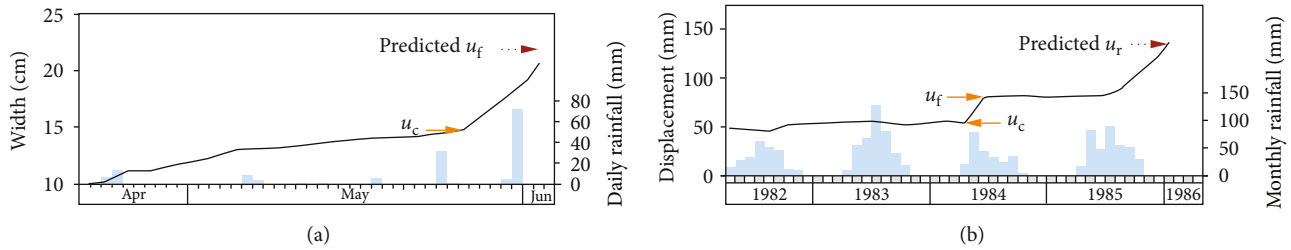

FIGURE 2: Displacement–time curves of the (a) Yanchihe [7] and (b) Longxi slopes [8]. The blue bars are the rainfall amounts.

pressure growth and strength degradation of geomaterials along a potential slip surface due to heavy rainfall [12]. However, the behavior of the Longxi slope contradicted this assumption because its displacement remained nearly unchanged under the heavy rainfall in July 1983, but substantial displacement was observed in May 1984 following less precipitation. Furthermore, the Longxi landslide occurred against the backdrop of the dry season in 1986. These paradoxes suggest that rainfall is not the key factor dominating the slope displacement patterns.

Physical modeling tests of antidip soft-hard interbedded rock slopes [13–15] show that soft-layer deformation is constrained by the hard layers until the hard layers break, suggesting that the interaction between different media on a potential slip surface is key to the displacement behavior of the slope. As the potential slip surface of a slope comprises a strong medium (locked segment) and a weak medium (transfixion segment), the mechanisms corresponding to the two patterns inherently involve mechanical synergy between the strong and weak media, which possess distinct mechanical properties [16, 17]. We will investigate this synergy on the aforementioned two slopes as typical examples.

2. Formation and Mechanical Behaviors of Locked and Transfixion Segments

The locked segments in the Yanchihe and Longxi slopes were formed by similar processes (Figure 1(c), [18]). In the Yanchihe phosphate mine, roof subsidence of the goaf caused slippage of the sliding mass along a weak interlayer of muddy dolomite affected by karstification (bottom slip

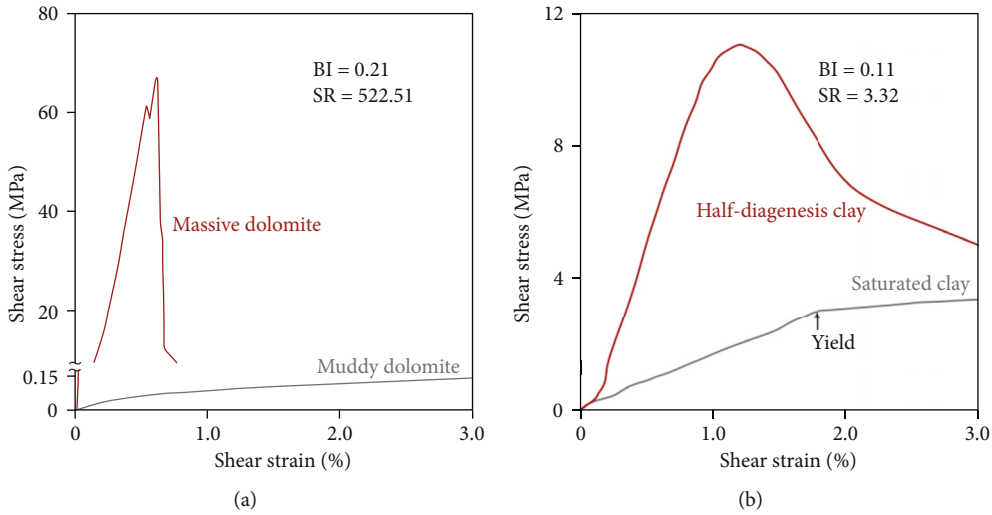

FIGURE 3: Shear stress–strain relations of the strain-softening strong media constituting locked segments (red curves) and strain-hardening weak media filling the lower transfixion segments (gray curves) on the slip surfaces of the (a) Yanchihe [21] and (b) Longxi slopes [8]. BI denotes the brittleness index [22] of the strong media (where a greater BI indicates a higher brittleness), and SR denotes the shear strength ratio of strong medium to weak medium.

surface) [19], generating tension cracks in the upper slope. As the slope deformed, the cracks connected to form a macrofissure. On its south side is the rough shovel-shaped main scarp of the landslide [1]. The relatively intact massive dolomite between the fissure and interlayer served as a locked segment. On the Longxi slope, a bottom slip is developed through strength degradation of the saturated water-sensitive clay along the phreatic line [19]. Upper tensile cracks were then produced by movement of the slope along the slip surface and gradually coalesced into a macrofissure. On its south side, the main scarp is similar to that of the Yanchihe slope. A locked segment thereby formed between the two transfixion segments.

The locked segments were gradually damaged under shear stress and external factors (e.g., rainfall). Eventually, the damage was sufficient to cause unlocking, which was quickly followed by catastrophic landslides. After the landslide events, shear striations were observed on both the middle and lower slip surfaces [20], but only the fracture surfaces at the speculated locations of the locked segments were fresh [8]. These facts confirm the existence of locked segments that underwent shear rupture and slip while the lower transfixion segments experienced shear dislocation.

Because the two lateral surfaces of an open tensile fissure (upper transfixion segment) hardly contact each other, this segment experiences negligible antisliding force. On the Yanchihe and Longxi slopes, the weak media on the lower transfixion segments are muddy dolomite and saturated clay, respectively, whereas the strong media constituting the locked segments are massive dolomite and compact half-diagenesis clay, respectively. In geotechnical tests [8, 21], the weak media with lower stiffness and strength exhibited strain-hardening properties whereas the strong media with higher strength and stiffness exhibited strain-softening properties (Figure 3).

3. Mechanical Synergy between Strong and Weak Media on Potential Slip Surface

The shear stress along a potential slip surface of slope naturally concentrates on a strong locked segment preceding its rupture at the peak-stress point. Thus, the mechanical synergy between strong and weak media is feeble in this stage, and the slope's displacement pattern is controlled by the locked segment. Under the combined effects of shear stress and external factors, the locked segment becomes damaged by crack growth. Unstable crack growth initiating from the volume-expansion point in the locked segment (point C in Figure 4) cannot be restrained even under a constant applied load [23]. Thus, the volume-expansion point corresponds to the onset of displacement acceleration of a locked segment-dominated slope. Once a damaged strain-softening locked segment reaches its peak-stress point (point D in Figure 4), it ruptures and the resulting stress drop causes partial transfer of the applied load to the weak medium on a lower transfixion segment, which subsequently yields. Such mechanical synergy between the strong and weak media homogenizes the distribution of shear resistance along a through-going slip surface; hence, it is referred to as resistance homogenization.

The massive dolomite is much stronger than the muddy dolomite on the lower transfixion segment on the Yanchihe slope. When ruptured at its peak-stress point, the massive dolomite generates a large, rapid post-peak stress drop and then it holds low residual strength, due to its high brittleness (Figure 3(a)). As a result of the large stress drop, most of its load is transferred to the weak medium, which then yields rapidly. In this context, the small resistance increase of the strain-hardening weak medium cannot offset the large resistance decrease of the locked segment during resistance homogenization, meaning that the total antisliding force decreases along the through-going slip

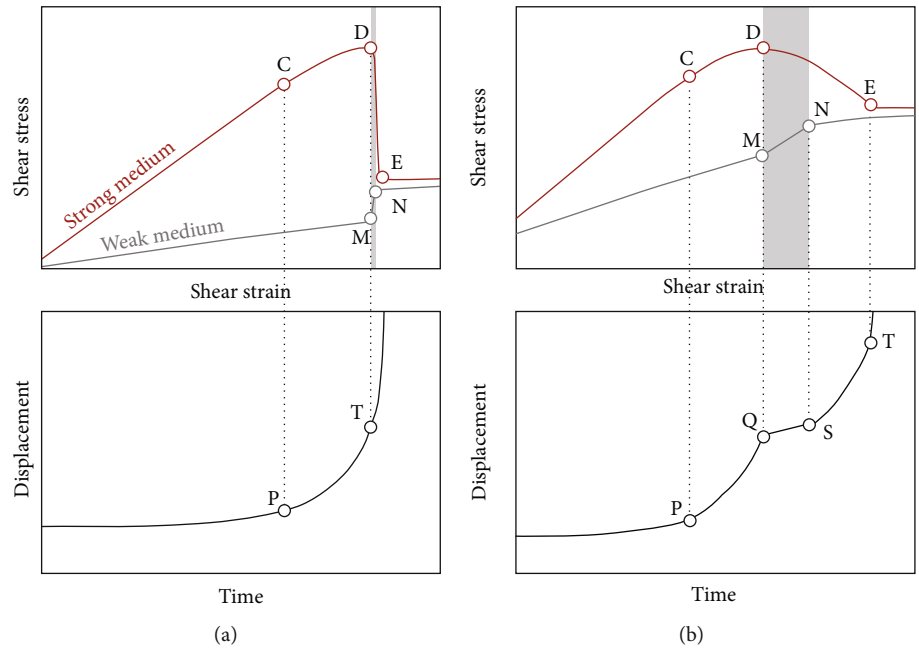

Figure 4: Shear stress–strain and displacement–time relations corresponding to (a) rapid and (b) slow unlocking-induced startup mechanisms. Points C, D, and E denote the volume-expansion, peak-stress, and residual-strength points of the locked segments, respectively. Points M and N denote the onset and termination, respectively, of the resistance homogenization process (gray shaded area). Points P and T denote the startups of displacement acceleration and landslide, respectively. In (b), points Q and S denote the suspension and resumption of displacement acceleration, respectively.

surface. Consequently, the displacement acceleration cannot be restrained, and the evolution of the Yanchihe slope tends toward instability. Between the peak-stress and residual-strength points of the locked segment, the displacement increase during the transient-unloading phase is minimal and slope instability develops; therefore, the peak-stress point can be viewed as the unlocking point of the locked segment. Such a mechanism following rapid homogenization is referred to as rapid unlocking-induced startup (Figure 4(a)).

Compared to the strong and weak media on the Yanchihe slope, the compacted half-diagenesis clay (locked segment) on the Longxi slope has lower brittleness and smaller strength and stiffness differences between the strong and weak media (Figure 3(b)). Therefore, when the locked segment ruptures, a small and gentle post-peak stress drop and a correspondingly slow and steady load transfer to the weak medium are expected. The weak medium should respond to this load transfer with a modest shear stress growth rate. In addition, given the much larger scale of the lower transfixion segment than the locked segment, the larger resistance increase of the weak medium can slightly overcompensate the smaller resistance decrease of the ruptured locked segment until the end of resistance homogenization, thereby achieving equilibrium between the resistance increase and decrease. Under this circumstance, the slow homogenization can suspend the displacement acceleration over an extended period. After homogenization, the displacement acceleration resumes because the resistance decrease of the locked segment is no longer offset by the resistance increase of the weak medium. When the total resistance reaches its minimum at the residual-strength point of the locked segment, slope instability will quickly follow. As such, if the displacement is stepwise accelerated, a locked segment might be unlocked at its residual-strength point. Such a mechanism following slow homogenization is here called slow unlocking-induced startup (Figure 4(b)).

4. Analysis and Results

The peak-stress and residual-strength points are two key characteristic points that indicate the instability of locked segment-dominated slopes following the rapid and slow unlocking-induced mechanisms, while displacement acceleration at the volume-expansion point preceding the two points can serve as their discernible precursor. If the mechanical relationships among these points are established, the displacement values at the first two points can be obtained based on those at the volume-expansion point. This will help in quantitatively determining the unlocking-induced mechanism of a locked segment-dominated slope.

By coupling a damage-constitutive model based on the Weibull distribution with the one-dimension renormalization group model, we obtained the theoretical expressions of displacements u_c, u_f, and u_r corresponding to the volume-expansion, peak-stress, and residual-strength points of the locked segment along the slip surface, respectively [2], and the displacement ratios of u_f/u_c and u_r/u_c exclusively depend on the parameter m and are formulated as [2, 24, 25]

$$\frac{u_f}{u_c} = \left(\frac{2^m - 1}{m \ln 2}\right)^{1/m}, \quad (1)$$

$$\frac{u_r}{u_c} = \left[\frac{(m+1)(2^m - 1)}{m \ln 2}\right]^{1/m}. \quad (2)$$

The parameter m characterizes the shapes of the stress–strain curves of geomaterials under various conditions (e.g., heterogeneity, loading rate, and moisture content), and a high m value corresponds to a sharp shape suggesting high brittleness. Therefore, it can comprehensively reflect the effect of various internal and external factors on the damage behavior of a locked segment. Because a locked segment contains massive joints and fissures serving as rainwater flow channels [26], it is with a certain water content. Furthermore, the locked segment is subjected to an extremely slow shear loading rate. Under these circumstances, the shape of its stress–strain curve can be gentle with a slow and small post-peak stress drop (Figure 5) [27, 28], which corresponds to a low m value. The specific reasonable range of m value, as Yang et al. [29] demonstrated, is 1.0–4.0. Because the two displacement ratios are insensitive to variations in the m value, they can be approximately expressed in terms of their average values within the range [25, 30]. Thus, Eqs. (1) and (2) are simplified as [2, 24, 25]

$$u_f = 1.48 u_c, \quad (3)$$

$$u_r = 2.49 u_c. \quad (4)$$

The reliability of this model has been validated in retrospective analyses of several locked segment-dominated landslides [24, 25]. Drawing on this model and on monitored displacement data, we can reveal the evolutionary mechanisms of the Yanchihe and Longxi landslides and test the hypothesis that the exponentially and stepwise accelerated displacement curves correspond, respectively, to rapid and slow unlocking-induced startup mechanisms.

The displacement of the Yanchihe locked segment along the slip surface is represented by the macrofissure width (Figure 1(a)). The width began exponentially increasing from May 24 of 1980, causing minor rockfalls [19]. This finding suggests that the volume-expansion point of the locked segment was attained at this time. The width at the peak-stress point of the locked segment determined by Eq. (3) approximately equals the value measured on June 2 of 1980 (Figure 2(a)), when rock-cracking noises were heard throughout the night [19]. Therefore, the locked segment was unlocked on that day and was succeeded by a 1 Mm^3 landslide at dawn on the following day. These results confirm that the peak-stress point of the locked segment corresponded to the startup of the Yanchihe landslide, and that an exponential evolution of the slope toward instability followed the rapid unlocking-induced startup mechanism.

The displacement of the Longxi slope, recorded at a monitoring point above the locked segment, began accelerating on April 1 of 1984 (Figure 2(b)) and was suspended from June 2 of 1984, as evidenced by the deflection of the displacement curve at that time. The sliding mass then rotated and began moving along the slip surface, accompanied by ground upheaval at the slope foot [20]. These phenomena suggest that the locked segment was damaged to reach its peak-stress point, from which the applied load was partially transferred to the weak medium on the lower transfixion segment, thereby causing slow resistance homogenization and displacement acceleration suspension. The displacement acceleration following the homogenization termination resumed from July 1 of 1985 and was followed by a 1.5 Mm^3 landslide. Therefore, the displacement before the landslide manifested a stepwise accelerated profile. The displacement value at the residual-strength point calculated by Eq. (4) approximates the measured value one week prior to the landslide (Figure 2(b)), confirming that the Longxi slope instability followed the slow unlocking-induced startup mechanism.

5. Discussion

Large-scale locked segment-dominated slopes have been widely reported worldwide. For example, ruptured locked segments caused major rockslides in the Canadian Rocky Mountains [31], Alps Mountains [5], and Tibet Plateau [1]. Because locked segments with high bearing capacity can accumulate abundant elastic strain energy, their unlocking often induces devastating high-speed and long-runout landslides [18, 32]. Therefore, uncovering the unlocking-induced startup mechanisms of such slopes has global implications for mitigating landslide hazards.

As explained above, the brittleness of locked segments crucially influences the magnitude and duration of the post-peak stress drop. Higher brittleness usually corresponds to higher strength and a larger stress drop. Thus, the unlocking-induced startup mechanism and displacement pattern of a slope are governed mainly by the brittleness of the locked segment. This understanding is mainly supported by site observations and mechanical analyses. To further consolidate the relationships between displacement patterns and unlocking-induced startup mechanisms and to discover essential factors governing these mechanisms, more evidence needs to be acquired via other methods, such as physical modeling experiments and numerical simulations.

Displacement of a locked segment-dominated slope usually follows damage accumulation in the locked segment. Damages are sourced from the self-weight of the slope mass and from external factors, especially rainfall. Water can strongly deteriorate the strength of geomaterials through the fatigue effect [33] and chemical alteration [34]. Moreover, water can raise the pore pressure on slip surfaces [35], thereby reducing their intergranular frictional resistance and structural stability. For instance, karstification can spread etch pits on dolomite cleavage and cause its disintegration [36]; the dissolution of the inorganic salt can decline the cohesion of the saturated clay on the Longxi slope by 27–50% [8]. Under these effects, the damage of a locked segment can reach certain mechanical characteristic points, each corresponding to a specific mechanical behavior. For instance, displacement begins accelerating at the

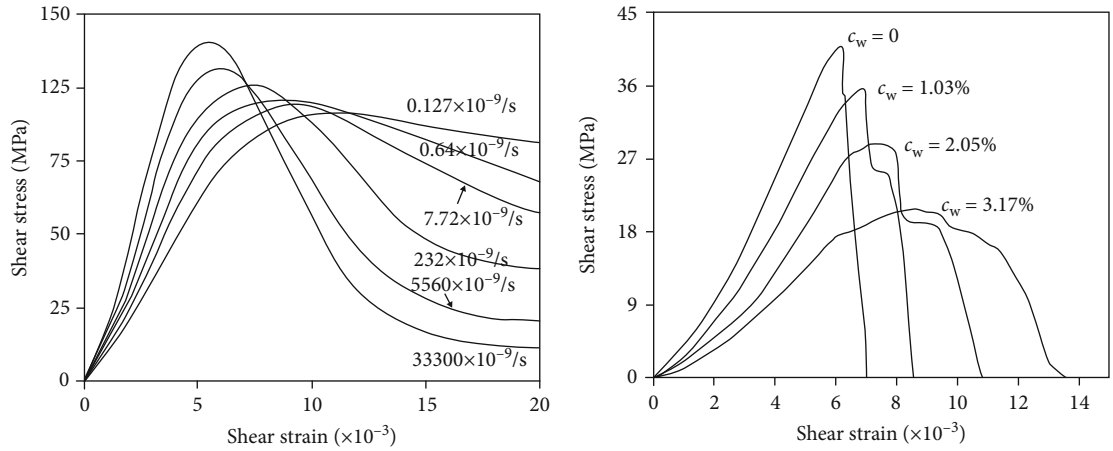

Figure 5: Shear stress–strain curves of rocks for various (a) strain rates [27] and (b) water contents (c_w) [28]. Slower loading rates and higher water contents result in less sharp curves, which correspond to lower m values.

volume-expansion point, and catastrophic slip begins at the peak-stress point or residual-strength point. Once these points are reached, the corresponding behaviors are inevitable even without the effects of external factors, because the locked segment can spontaneously crack from its volume-expansion point under the self-weight of a slope. Thus, the displacement of the Longxi slope began speeding up when the volume-expansion point of the locked segment was reached in May of 1984, although the precipitation was below the maximum precipitation in 1983; the Longxi slope evolved uncontrollably toward instability, and its catastrophic slip occurred during a three-month-long rainless period (total precipitation < 4 mm from November 1985 to January 1986) rather than during a wet season. Indeed, the damage behavior of the locked segment governs the evolution of a locked segment-dominated slope toward instability, as described by the constant displacement ratios. Therefore, locked segment-dominated landslides are predictable based on firm physical principles.

To reliably assess the stability of a locked segment-dominated slope, one must investigate the distributions of the locked and transfixion segments and the mechanical properties of media on a potential slip surface. The unlocking-induced startup mechanism of a slope can be prejudged on this basis. Moreover, we highlight that damage should be reliably detected by setting monitoring points on the locked segment.

6. Conclusions

Large-scale locked segment-dominated slopes are extensively distributed worldwide. Governed by their brittleness, locked segments are unlocked at either their peak-stress or residual-strength points, causing impending landslides. Accordingly, the startup mechanism of the landslides can be rapid with an exponentially accelerated displacement pattern or slow with a stepwise accelerated displacement pattern. However, as mentioned above, further insights into the relationships between the unlocking process, displacement pattern, and startup behavior are still required.

The results of this study demonstrate that locked segment-dominated landslides obey certain mechanical rules and can, thus, be reliably predicted.

Data Availability

The precipitation data were downloadable for registered members of the China Meteorological Data Service Centre (http://data.cma.cn/en). The displacement and mechanical experimental data were derived from published literatures.

Conflicts of Interest

The authors declare that they have no conflicts of interests.

Authors' Contributions

S. Qin initiated the study. S. Qin and H. Chen developed the structure of the study. H. Chen, C. Xu, and Y. Cui analyzed the data and interpreted the results. H. Chen wrote the original manuscript. All authors discussed the results and revised the manuscript.

Acknowledgments

This work was supported by the National Natural Science Foundation of China (nos. 42090052 and 42107184).

References

[1] R. Huang, "Mechanisms of large-scale landslides in China," *Bulletin of Engineering Geology and the Environment*, vol. 71, no. 1, pp. 161–170, 2012.

[2] S. Qin, Y. Wang, and P. Ma, "Exponential laws of critical displacement evolution for landslides and avalanches," *Chinese Journal of Rock Mechanics and Engineering*, vol. 29, no. 5, pp. 873–880, 2010.

[3] K. Terzaghi, "Stability of steep slopes on hard unweathered rock," *Géotechnique*, vol. 12, no. 4, pp. 251–270, 1962.

[4] D. Elmo, D. Stead, B. Yang, G. Marcato, and L. Borgatti, "A new approach to characterise the impact of rock bridges in stability analysis," *Rock Mechanics and Rock Engineering*, vol. 55, pp. 2551–2569, 2021.

[5] M. Frayssines and D. Hantz, "Failure mechanisms and triggering factors in calcareous cliffs of the subalpine ranges (French Alps)," *Engineering Geology*, vol. 86, no. 4, pp. 256–270, 2006.

[6] C. Lévy, L. Baillet, D. Jongmans, P. Mourot, and D. Hantz, "Dynamic response of the Chamousset rock column (Western Alps, France)," *Journal of Geophysical Research: Earth Surface*, vol. 115, no. F4, 2010.

[7] Y. Sun and B. Yao, "Study on mechanism of the rockslide at Yanchihe phosphorus mine," *Hydrogeology and Engineering Geology*, vol. 1, pp. 1–7, 1983.

[8] Z. Zhang, S. Wang, D. Nie, H. Liu, Y. Li, and J. Xu, *Study on Major Engineering Geological Problems of Longyangxia Hydropower Station*, Chengdu University of Science and Technology Press, Chengdu, 1989.

[9] C. Zhu, M. He, M. Karakus, X. Cui, and Z. Tao, "Investigating toppling failure mechanism of anti-dip layered slope due to excavation by physical modelling," *Rock Mechanics and Rock Engineering*, vol. 53, no. 11, pp. 5029–5050, 2020.

[10] D. P. Adhikary and A. V. Dyskin, "Modelling of progressive and instantaneous failures of foliated rock slopes," *Rock Mechanics and Rock Engineering*, vol. 40, no. 4, pp. 349–362, 2007.

[11] D. N. Petley, M. H. Bulmer, and W. Murphy, "Patterns of movement in rotational and translational landslides," *Geology*, vol. 30, no. 8, pp. 719–722, 2002.

[12] A. L. Handwerger, E. J. Fielding, M.-H. Huang, G. L. Bennett, C. Liang, and W. H. Schulz, "Widespread initiation, reactivation, and acceleration of landslides in the northern California coast ranges due to extreme rainfall," *Journal of Geophysical Research: Earth Surface*, vol. 124, no. 7, pp. 1782–1797, 2019.

[13] M. Dong, F. Zhang, J. Lv, M. Hu, and Z. Li, "Study on deformation and failure law of soft-hard rock interbedding toppling slope base on similar test," *Bulletin of Engineering Geology and the Environment*, vol. 79, no. 9, pp. 4625–4637, 2020.

[14] M. Dong, F. Zhang, M. Hu, and C. Liu, "Study on the influence of anchorage angle on the anchorage effect of soft-hard interbedded toppling deformed rock mass," *KSCE Journal of Civil Engineering*, vol. 24, no. 8, pp. 2382–2392, 2020.

[15] Z. Tao, Q. Geng, C. Zhu et al., "The mechanical mechanisms of large-scale toppling failure for counter-inclined rock slopes," *Journal of Geophysics and Engineering*, vol. 16, no. 3, pp. 541–558, 2019.

[16] D. N. Petley, D. J. Petley, and R. J. Allison, "Temporal prediction in landslides-understanding the Saito effect," in *Presented at The Tenth International Symposium on Landslides and Engineered Slopes, Xi'an, China*, pp. 886–892, CRC Press, London, 2008.

[17] S. Qin, J. Jiao, and Z. Li, "Nonlinear evolutionary mechanisms of instability of plane-shear slope: catastrophe, bifurcation, chaos and physical prediction," *Rock Mechanics and Rock Engineering*, vol. 39, no. 1, pp. 59–76, 2006.

[18] X. Wang, "Geological properties of large-scale highspeed landslides and their mechanism models," *Bulletin of Engineering Geology and the Environment*, vol. 43, no. 1, pp. 93–99, 1991.

[19] C. Liu and R. Xiao, "Mechanism analysis on Yanchihe avalanche disaster in Yuan'an, Hubei," *Journal of Catastrophology*, vol. 36, no. 2, pp. 130–133+150, 2021.

[20] H. Liu and Z. Zhang, "The mechanism of hugh landslides in overconsolidated clay near Longyang gorge damsite," *Journal of Chengdu College of Geology*, vol. 13, no. 3, pp. 94–104, 1986.

[21] T. Li, *Research on the Mechanism of Mountainous Landslide Geohazrds Induced by Underground Mining*, University of Chinese Academy of Sciences, 2014.

[22] F. Meng, H. Zhou, C. Zhang, R. Xu, and J. Lu, "Evaluation methodology of brittleness of rock based on post-peak stress–strain curves," *Rock Mechanics and Rock Engineering*, vol. 48, no. 5, pp. 1787–1805, 2015.

[23] F. Renard, J. McBeck, N. Kandula, B. Cordonnier, P. Meakin, and Y. Ben-Zion, "Volumetric and shear processes in crystalline rock approaching faulting," *Proceedings of the National Academy of Sciences*, vol. 116, no. 33, pp. 16234–16239, 2019.

[24] H. Chen, S. Qin, L. Xue, and C. Xu, "Why the Xintan landslide was not triggered by the heaviest historical rainfall: mechanism and review," *Engineering Geology*, vol. 294, article 106379, 2021.

[25] H. Chen, S. Qin, L. Xue, B. Yang, and K. Zhang, "A physical model predicting instability of rock slopes with locked segments along a potential slip surface," *Engineering Geology*, vol. 242, pp. 34–43, 2018.

[26] C. Zhu, X. Xu, X. Wang et al., "Experimental investigation on nonlinear flow anisotropy behavior in fracture media," *Geofluids*, vol. 2019, Article ID 5874849, 9 pages, 2019.

[27] Z. T. Bieniawski, "Time-dependent behaviour of fractured rock," *Rock Mechanics*, vol. 2, no. 3, pp. 123–137, 1970.

[28] H. Li, Y. Qiao, R. Shen et al., "Effect of water on mechanical behavior and acoustic emission response of sandstone during loading process: phenomenon and mechanism," *Engineering Geology*, vol. 294, article 106386, 2021.

[29] B. Yang, S. Qin, L. Xue, and H. Chen, "The reasonable range limit of the shape parameter in the Weibull distribution for describing the brittle failure behavior of rocks," *Rock Mechanics and Rock Engineering*, vol. 54, no. 6, pp. 3359–3367, 2021.

[30] L. Xue, S. Qin, X. Pan, H. Chen, B. Yang, and K. Zhang, "Mechanism and physical prediction model of instability of the locked-segment type slopes," *Journal of Engineering Geology*, vol. 26, no. 1, pp. 179–192, 2018.

[31] D. M. Cruden, "Major rock slides in the rockies," *Canadian Geotechnical Journal*, vol. 13, no. 1, pp. 8–20, 1976.

[32] R. Huang, G. Chen, F. Guo, G. Zhang, and Y. Zhang, "Experimental study on the brittle failure of the locking section in a large-scale rock slide," *Landslides*, vol. 13, no. 3, pp. 583–588, 2016.

[33] K. Hall and A. Hall, "Weathering by wetting and drying: some experimental results," *Earth Surface Processes and Landforms*, vol. 21, no. 4, pp. 365–376, 1996.

[34] R. A. L. Wray and F. Sauro, "An updated global review of solutional weathering processes and forms in quartz sandstones and quartzites," *Earth-Science Reviews*, vol. 171, pp. 520–557, 2017.

[35] D. K. Keefer, R. C. Wilson, R. K. Mark et al., "Real-time landslide warning during heavy rainfall," *Science*, vol. 238, no. 4829, pp. 921–925, 1987.

[36] M. Urosevic, C. Rodriguez-Navarro, C. V. Putnis, C. Cardell, A. Putnis, and E. Ruiz-Agudo, "In situ nanoscale observations of the dissolution of dolomite cleavage surfaces," *Geochimica et Cosmochimica Acta*, vol. 80, pp. 1–13, 2012.

Hindawi
Geofluids
Volume 2023, Article ID 1743305, 10 pages
https://doi.org/10.1155/2023/1743305

Research Article

Propagation Mechanism of Deep-Water Impulse Waves Generated by Landslides in V-Shaped River Channels of Mountain Valleys: Physical Model of Regular Rigid Block

Rubin Wang,[1,2] **Yunzi Wang**,[1] **Jianxin Wan**,[2] **Weiya Xu**,[1] **Yue Yang**,[2] **and Huanling Wang**[1]

[1]*Key Laboratory of Ministry of Education for Geomechanics and Embankment Engineering, Hohai University, Nanjing, China*
[2]*Research Institute of Geotechnical Engineering, Hohai University, Nanjing, China 210098*

Correspondence should be addressed to Rubin Wang; rbwang@hhu.edu.cn

Received 30 September 2022; Revised 1 November 2022; Accepted 24 November 2022; Published 8 February 2023

Academic Editor: Yiding Bao

Landslide-induced impulse waves in alpine valleys are a significant risk to large-scale dam and reservoir engineering projects in the surrounding area. In this study, a 1 : 200-scale physical model of landslide-induced impulse waves in a V-shaped river channel was established, and 18 groups of tests were conducted to evaluate the influence of different parameters, such as the volume and shape of the landslide body, water entry velocity, and water depth of the reservoir. Based on the test results, a dimensionless formula was established for the first wave height of impulse waves caused by a deep-water landslide in a V-shaped channel. An energy conversion law was determined for the impact of landslide-induced impulse waves on the reservoir bank. Finally, a distribution law was obtained for the initial maximum pressure caused by landslide-induced impulse waves along the water depth on the opposite bank. The theoretical predictions of the dimensionless formula showed good agreement with the experimental results, and the energy conversion rate of the landslide-induced impulse waves initially increased and then decreased with an increasing Froude number. The maximum dynamic water pressure showed a triangular distribution with increasing water depth below the surface of the still water body. The impact pressure of the impulse waves on the slope on the opposite bank increased with the water entry velocity. This study provides a scientific basis for the risk prevention and control of landslide-induced impulse waves in river channels feeding into reservoirs.

1. Introduction

High-velocity landslides in alpine areas and gorges produce huge impulse waves that feature short generation and propagation times, fast velocities, and a wide disaster range. Around major hydropower projects, they can not only wash away hydraulic structures and block river channels but may also cause serious accidents such as dam failure. In 1963, a landslide at Vajont Dam in Italy caused a huge wave with a height of up to 175 m, which destroyed a 70 m high concrete dam, washed away the town of Longaroni and five nearby villages, and claimed nearly 2000 lives. In 1985, a landslide in Xintan, Zigui, near China's Three Gorges Dam, induced impulse waves that climbed up to a height of 54 m. The impulse waves overturned four fishing boats 2 km upstream and spread 42 km upstream and downstream to cause more than ten deaths. Therefore, research on landslide-induced impulse waves in alpine areas can provide a crucial reference for early warning and risk prevention of disasters in high dams and large reservoirs.

Various methods have been used in the research and analysis of landslide-induced impulse waves, e.g., analytical solutions [1–4], numerical simulations [5–8], physical models [9–14], and field data analysis [15, 16]. Because the location and time that a landslide enters the water cannot be accurately predicted in advance, obtaining original data on landslide-induced impulse waves is difficult. Thus, physical models are used to simulate landslide-induced impulse

waves and obtain characteristic parameters such as the first wave height, propagation process, and impact pressure. This approach is widely used to research landslide-induced impulse waves in alpine areas.

Previous models of landslide-induced impulse waves have considered the influence of the water entry velocity, volume, angle, and density of the landslide body. However, these models mostly used rectangular or trapezoidal channels to represent rivers. Few studies have considered the propagation process and impact pressure distribution of landslide-induced impulse waves in V-shaped river channels, which are common in alpine areas. The slopes of the banks on both sides of a V-shaped channel significantly affect the formation and propagation of landslide-induced impulse waves. Compared with rivers in plains and flat lands, impulse waves in V-shaped river channels in alpine areas have a more obvious disaster chain. The narrow river channel means that the landslide body can easily block it upon entry, which would greatly increase the overall water depth and may even form a dam that threatens the downstream area. In addition, the opposite bank confines the huge kinetic energy generated by the landslide-induced impulse waves and does not let it dissipate. This increases the impact pressure on the banks and dam bodies, which affects the stability and safety of the facilities. Even worse, the impulse waves may strike the opposite bank directly, which would damage infrastructure along the riverfront and threaten the safety of people and property.

In this study, a 1 : 200-scale physical model was established to reveal the characteristics of deep-water landslide-induced waves in V-shaped river channels. Experiments were performed to consider the influence of the volume, shape, and velocity of the landslide body and the water depth of the reservoir. A dimensionless formula was derived for the first wave height in the V-shaped channel. An energy conversion law was obtained for the impulse waves, and a distribution law was obtained for the initial maximum dynamic water pressure on the opposite bank along the water depth. This study provides a scientific reference for the risk prevention and control of landslide-induced impulse waves in the alpine areas of major hydropower projects.

2. Materials and Methods

A 1 : 200-scale physical model was established based on the gravity similarity criterion and Froude similarity criterion, as shown in Figure 1. A high-definition camera was installed on one side of the tank to capture the landslide body as it slid into the water and the resulting impulse waves. Wave height gauges N.1, N.2, and N.3 were set in the channel at a spacing of 1.2 m. Wave height gauge N.4 was installed on the opposite bank to record the rise of impulse waves. The wave height gauges measured the wave height at a frequency of 50 Hz and a resolution of 0.1 mm. Eight water pressure sensors (P1–P8) were arranged on the opposite bank to measure the impact pressure of the impulse waves at a collection frequency of 50 Hz and resolution of 0.01 kPa. The pressure sensor P1, which was 73 cm away from the bottom of the river channel, was arranged at the central axis of the opposite bank. The positions of other sensors are shown in Figure 1.

In the experimental model, the inclination of the sliding bed was 34°, the inclination of the opposite bank was 43°, and the fall height of the center of mass of the block was 1.8 m. The water depth of the V-shaped channel was between 0.86 and 1.26 m. According to the geotechnical characteristic of landslides, they are divided into two types: loose earth landslides and rock landslides. This experiment studied rock landslides [17–19]. As shown in Figure 2, the landslide body was represented by concrete blocks of different shapes that had a density of 2300 kg/m^3, length of 0.45–0.55 m, width of 0.3–0.4 m, and thickness of 0.1–0.27 m. The width of the experimental slot was 0.66 m. All landslide bodies were narrower than the width of the slot, and the generated impulse waves propagated in the lateral direction. The velocity of the landslide body was controlled by a sliding control device. The sliding velocity was measured by a Hall velocity sensor connected to the landslide body at a resolution of 0.01 m/s.

An orthogonal design was adopted for the experiments with the physical model. The maximum wave amplitude, which corresponded to the maximum water entry velocity, was assumed to be the first wave amplitude. After the landslide-induced impulse waves propagated, the distance between the first two crests was measured and was taken as the wavelength. Table 1 presents the experimental design and results. The test parameters included the length (l), width (w), and thickness (s) of the landslide body, as well as the still water depth (h_0), sliding bed inclination angle (α), and water entry velocity of the landslide body (u). The results were represented by the Froude number (F), first wave amplitude (a), and wave celebrity (c).

3. Results and Discussion

3.1. Generation and Propagation Characteristics. The velocity at which a landslide body enters the water is an important factor that affects the generation and propagation of impulse waves. However, the difficulty of measuring the water entry velocity has limited the number of related studies. Fritz et al. [10] and Heller et al. [20] used particle image velocimetry and a laser distance sensor to track and measure the vector field for the near-field impulse wave velocity. To analyze the impact velocity of the landslide, they used the calculation formula presented by Körner [21].

$$u = \sqrt{2g\Delta z(1 - f\cot\alpha)}, \tag{1}$$

where u is the water entry velocity of the center of mass of the landslide body (m/s), g is the acceleration of gravity (m/s^2), Δz is the height between the original center of the mass and the static water depth (m), f is the friction coefficient, and α is the inclination angle of the sliding bed (°). Equation (1) ignores the effects of air resistance, underwater friction, and water resistance, so the water entry velocity u increases with an increase in any of the other terms.

The sliding velocity control device was used to increase the sliding velocity of the landslide body before entering

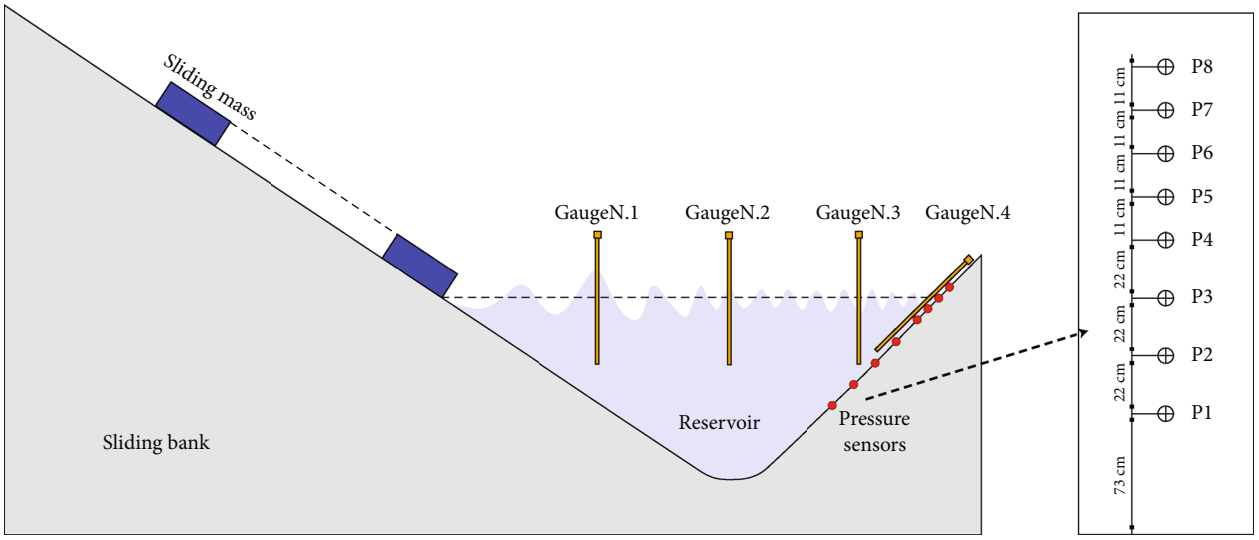

Figure 1: Schematic diagram of the physical model.

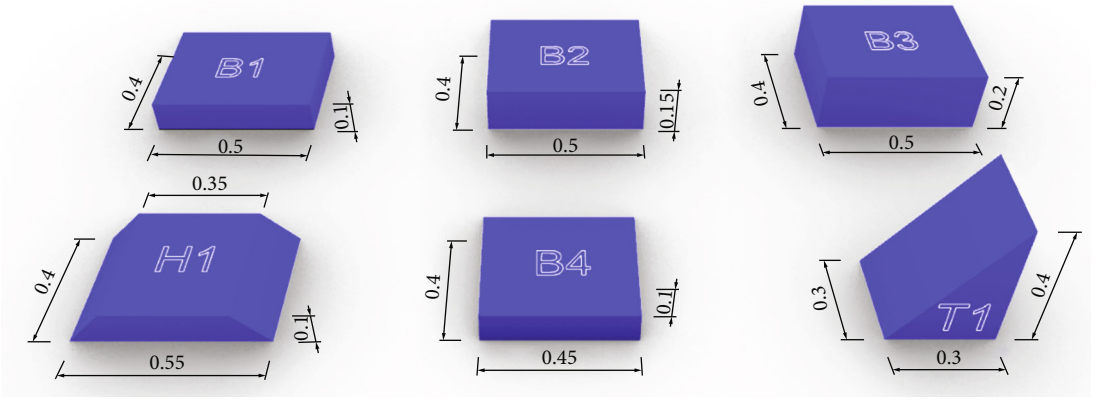

Figure 2: Schematic diagram of regular rigid blocks representing the landslide body (dimensions: m).

the water to 0.67, 1.16, and 1.67 m/s. The changes in the sliding velocity and acceleration as the landslide body entered the water were obtained. As shown in Figure 3, the landslide body initially showed an approximately linear increase in velocity followed by a slow acceleration or deceleration and a rapid deceleration to a final stop. These three stages corresponded to the landslide body sliding in air, sliding in water, and bottoming out, respectively. The duration of the second stage (i.e., slow acceleration or deceleration) differed with the water depth.

Figure 4 shows the three stages of the sliding acceleration for each sliding velocity. Because the sliding bed and landslide body were controlled by a mechanical transmission device, the initial velocity of the landslide body was provided by the control device. Before the landslide body reached the still water surface, the reduction in acceleration was mainly caused by the friction between the sliding bed surface and the landslide body. After the block entered the water, the acceleration was affected by the friction from the sliding bed surface and the viscous resistance of the water, so it became negative. The resistance reached its maximum when the front end of the landslide body reached the bottom of the river, which caused the landslide body to quickly decelerate and stop.

Based on the results of the physical model, the generation and propagation of landslide-induced impulse waves in a V-shaped river channel can be summarized into three stages. In the first stage, the landslide body entered the water body quickly; the front edge of the landslide body hit and displaced part of the water body. A small part of the displaced water body jumped from the water surface to form a water tongue, and most of the water body near the water entry point was compressed and increased in height, which formed the first wave. In the second stage, the landslide body slid into the water body and transferred energy continuously. It displaced more of the water body, which caused the leading edge of the rising wave to move forward, while the trailing edge moved toward the impact crater that was generated by the landslide body when it struck the water body because of gravity. The water tongue formed by the impact then began to splash back into the water. In the third stage, the landslide body stopped moving and completed the process of transferring energy to the water. Then, water converted the kinetic energy to form impulse waves that spread to the opposite bank.

Table 1: Experimental design and test results.

No.	Landslide body	Test parameters						Test results		
		l (m)	w (m)	s (m)	h_0 (m)	α (°)	u (m/s)	F	a (m)	c (m/s)
1	B1	0.50	0.40	0.10	0.86	34	1.16	0.40	0.037	2.89
2	B1	0.50	0.40	0.10	1.10	34	1.67	0.51	0.064	3.33
3	B1	0.50	0.40	0.10	1.26	34	0.67	0.19	0.014	2.95
4	B2	0.50	0.40	0.15	0.86	34	1.67	0.58	0.098	3.42
5	B2	0.50	0.40	0.15	1.10	34	0.67	0.20	0.026	3.03
6	B2	0.50	0.40	0.15	1.26	34	1.16	0.33	0.059	2.97
7	B3	0.50	0.40	0.20	0.86	34	0.67	0.23	0.052	2.77
8	B3	0.50	0.40	0.20	1.10	34	1.16	0.35	0.088	2.94
9	B3	0.50	0.40	0.20	1.26	34	1.67	0.47	0.107	3.23
10	B4	0.45	0.40	0.10	0.86	34	0.67	0.23	0.028	2.60
11	B4	0.45	0.40	0.10	1.10	34	1.16	0.35	0.036	3.10
12	B4	0.45	0.30	0.10	1.26	34	1.67	0.48	0.070	3.42
13	T1	0.50	0.30	0.27	0.86	34	1.67	0.58	0.111	3.57
14	T1	0.50	0.30	0.27	1.10	34	0.67	0.20	0.030	3.10
15	T1	0.50	0.30	0.27	1.26	34	1.16	0.33	0.061	3.33
16	H1	0.55	0.40	0.10	0.86	34	1.16	0.40	0.048	3.20
17	H1	0.55	0.40	0.10	1.10	34	1.67	0.51	0.075	3.42
18	H1	0.55	0.40	0.10	1.26	34	0.67	0.18	0.017	3.09

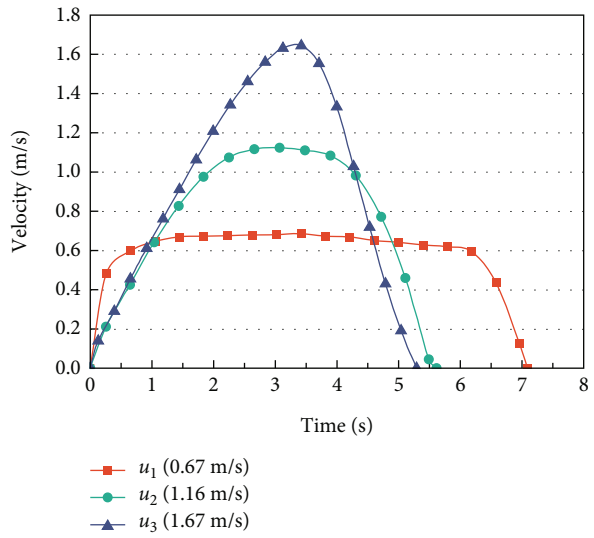

Figure 3: Changes in velocity before and after the landslide body entered the water at three sliding velocities.

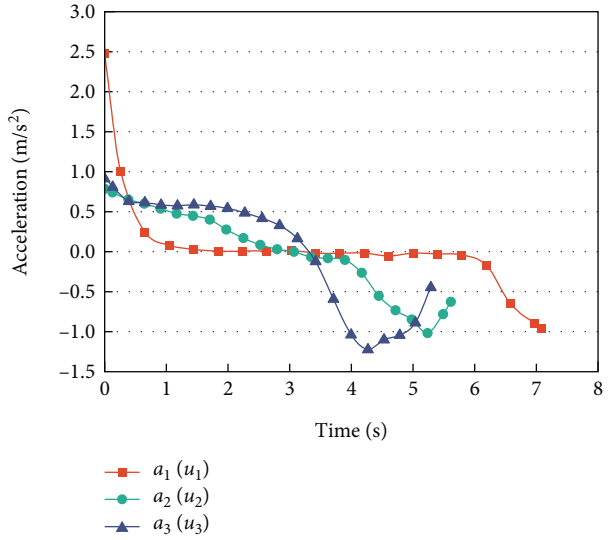

Figure 4: Changes in acceleration before and after the landslide body entered the water at three sliding velocities.

To reveal the influence of the shape and water entry velocity of the landslide body on the propagation of impulse waves, the monitoring data of key wave height gauges were selected, and 18 groups of time history curves for the amplitudes of the landslide-induced impulse waves were obtained, as shown in Figure 5. The impulse waves featured the formation of an advancing wave train dominated by waves with positive amplitudes (i.e., wave crests). The first or second wave crests had the largest amplitude, followed by oscillating waves of smaller amplitude. The largest trough occurred before the highest crest. In general, the different shapes of the landslide bodies generated similar impulse waves on the opposite bank, but the amplitude and period differed.

3.2. Waveform Characteristics. According to the experimental results of Noda [3] and Fritz et al. [1], the waveforms of landslide-induced impulse waves in the near-field region can be divided into weakly nonlinear oscillatory waves ($F < 4 - 7.5S$), nonlinear transition waves ($4 - 7.5S \le F < 6.6 - 8S$), solitary waves ($6.6 - 8S \le F < 8.2 - 8S$), and dissipative transient bores ($F \ge 8.2 - 8S$). Each waveform, which was dependent on the Froude number ($F = u/\sqrt{gh_0}$) of

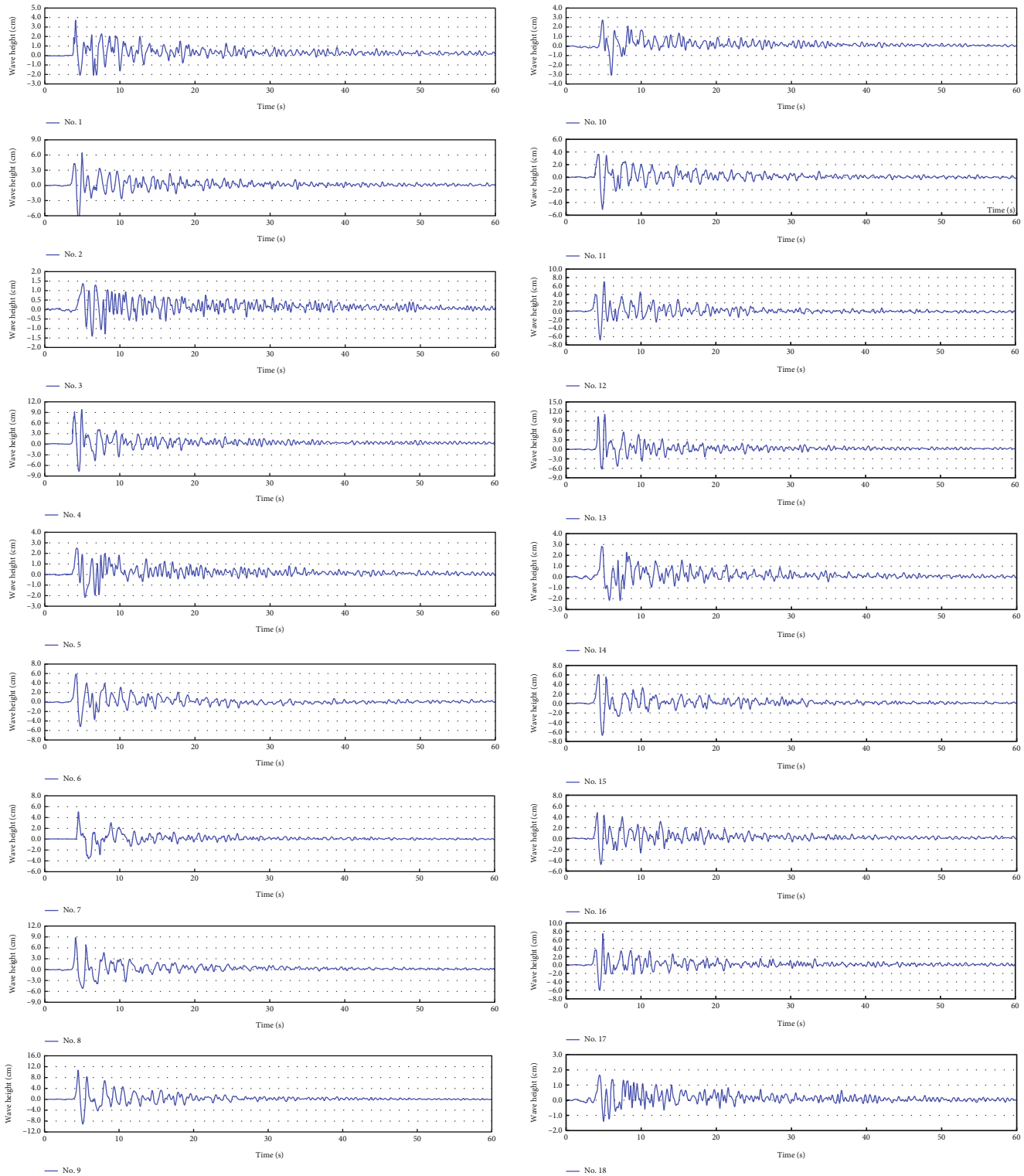

Figure 5: Time history curves of 18 groups of wave amplitudes measured by wave height gauge no. 1.

the landslide body, struck the water body and the relative thickness of the landslide body ($S = s/h_0$). F was less than ($4 - 7.5S$) in all 18 groups of tests, so the impulse waves were all weakly nonlinear oscillatory waves.

The wave amplitude and velocity are important characteristics of landslide-induced impulse waves. Previous studies have shown that the geometric size of the landslide body, water depth, and water entry velocity are the controlling factors of the first wave amplitude. In this study, nonlinear regression analysis was used to identify the correlation between the geometric dimensions of the landslide body, water depth in front of the slope, and water entry velocity

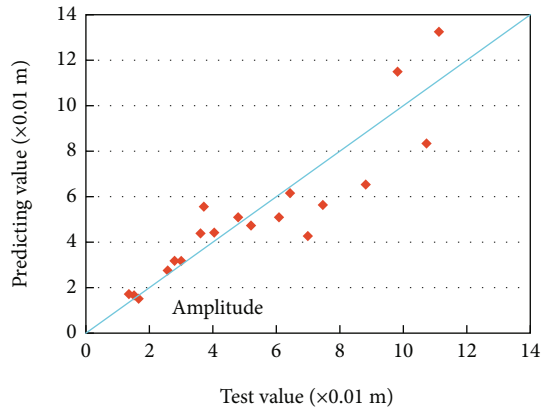

Figure 6: Predicted and experimental values of the first wave amplitude.

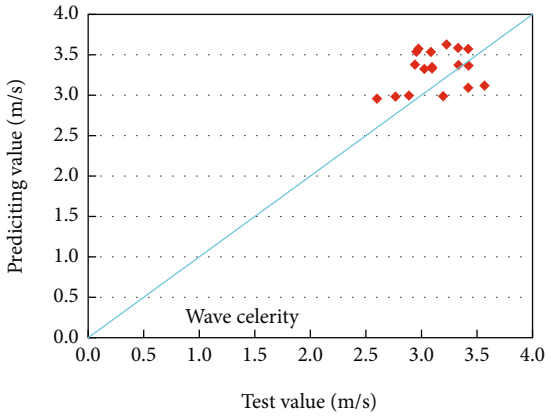

Figure 7: Calculated and experimental values of the wave celerity.

of the landslide body. A dimensionless formula was obtained for the first wave amplitude in a V-shaped river channel:

$$\frac{a}{h_0} = 0.951\left(\frac{u}{\sqrt{gh_0}}\right)^{1.197}\left(\frac{l}{h_0}\right)^{-1.013}\left(\frac{w}{h_0}\right)^{0.990}\left(\frac{s}{h_0}\right)^{0.717}, \quad (2)$$

where $(u/\sqrt{gh_0})$ is the relative water entry velocity, (l/h_0) is the relative length, (w/h_0) is the relative width, and (s/h_0) is the relative thickness of the landslide body. Figure 6 compares the predicted first wave amplitude via Equation (2) with the test results. A correlation coefficient of 0.82 was obtained.

The wave velocity describes the propagation distance of a waveform per unit time, and it is an important parameter for calculating the propagation of landslide-induced impulse waves. The following empirical formula for nonlinear waves is usually used for prediction.

$$c = \sqrt{g(h_0 + a)}. \quad (3)$$

Figure 7 compares the prediction results of Equation (3) with the measured test data. The correlation coefficient was 0.551, with a maximum error of 16.8% and an average error

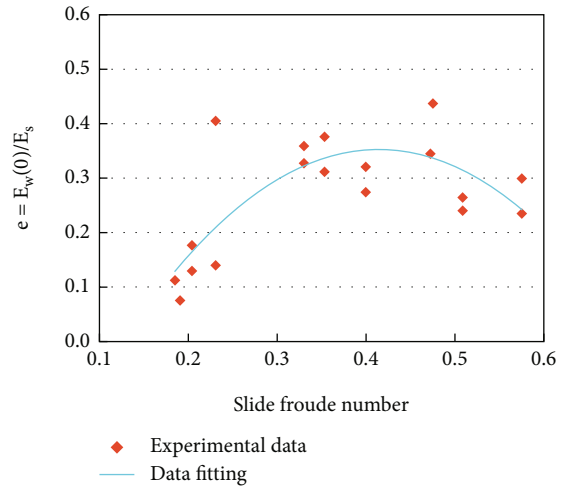

Figure 8: Energy conversion rate at different Froude numbers.

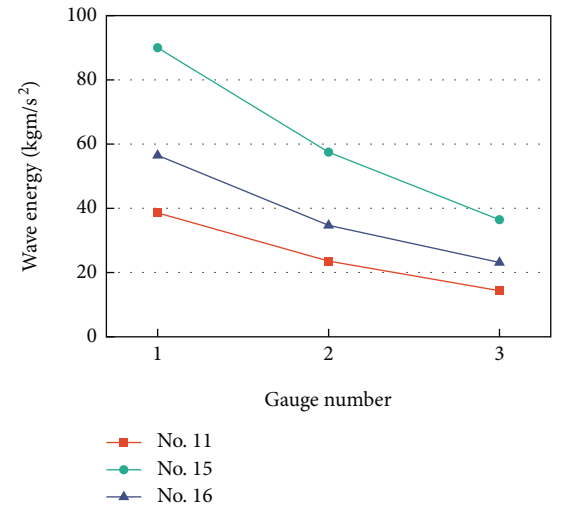

Figure 9: Wave energy of different shapes for the landslide body measured by different wave height gauges.

of 9.1%. The error can be attributed to the frame rate of the camera. Although the correlation was low, it was numerically close. Therefore, the theoretical formula of wave celerity can be used to predict the celerity of the impulse wave [22].

Dimensionless functions are commonly used in regression analysis for prediction. Similar to Equation (2), a series of dimensionless power exponents are multiplied, which are usually specific values of the same controlling factor. Different scholars have used different controlling factors for regression analysis. Noda [3] proposed the method of calculating the maximum impulse wave height based on a linear relationship with the Froude number. Fritz et al. [1] proposed the method of calculating the maximum impulse wave height based on the Froude number and relative thickness. Ataie-Ashtiani and Nik-khah [9] proposed the method of calculating the maximum impulse wave height by considering factors such as the dimensionless sliding volume, Froude number, inclination angle of the sliding surface, and underwater sliding time. Zweifel et al. [23] proposed another method of calculating the maximum impulse wave height

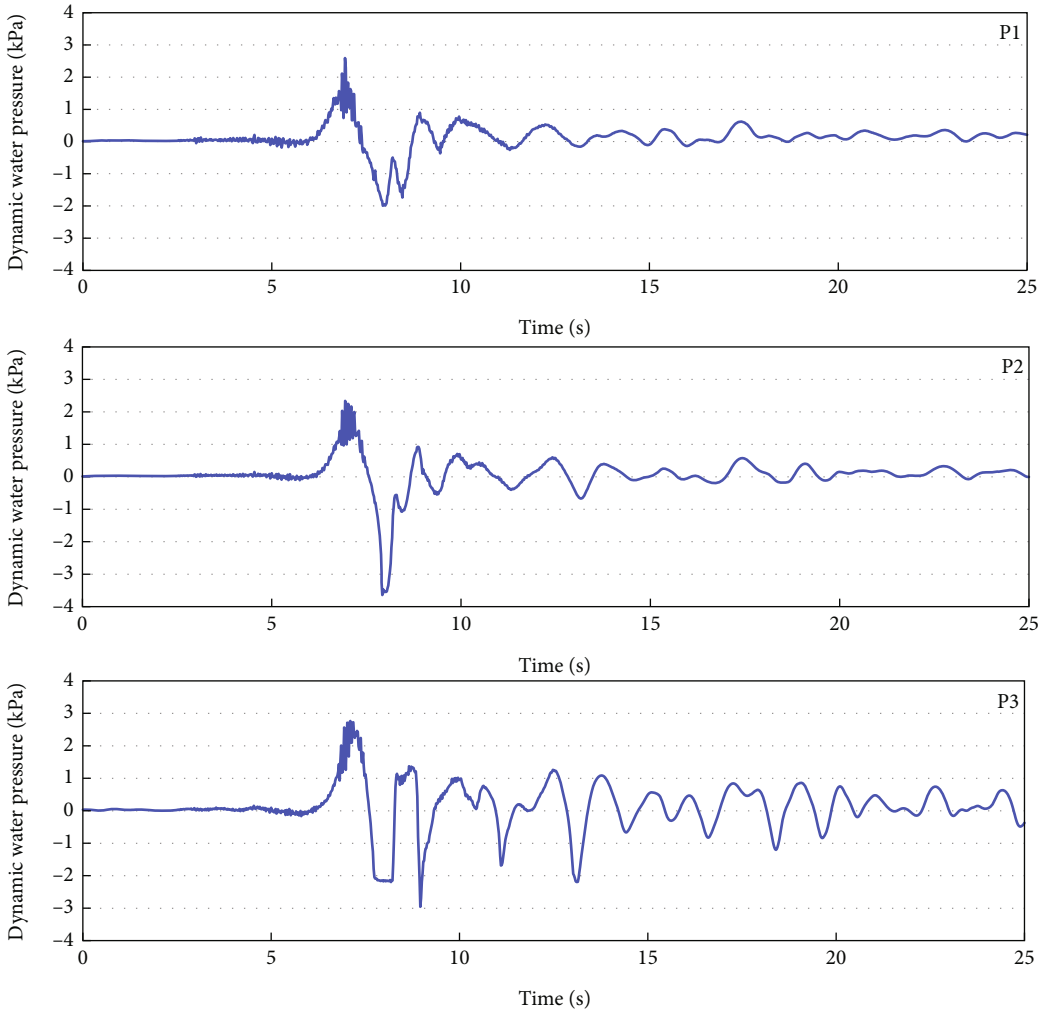

Figure 10: Time history curves of the dynamic water pressure with landslide body T1 at measurement points P1–P3.

by considering the Froude number, relative thickness, and relative mass. The power exponents of each variable in the equations proposed by the above researchers varied substantially; in particular, the power exponent of the Froude number was between 0.2 and 1.4. A larger power exponent for the Froude number indicated a greater influence of the relative velocity on the wave height and vice versa. For V-shaped channels, the wave height of landslide-induced impulse waves increased significantly with the water entry velocity of the landslide body. The dimensionless formula proposed for the first wave amplitude of the V-shaped channel (i.e., Equation (2)) confirmed this cognition, which reflected its applicability and rationality.

3.3. Energy Characteristics. The main characteristics of landslide-induced impulse waves are closely related to the law of energy transfer of the landslide mass. The time history curves of the wave heights collected by the wave height gauges were used to calculate the wave energy as follows according to Ataie-Ashtiani and Nik-khah [9]:

$$E_w = 2E_{\text{pot}} = \rho_w g c \int \eta^2 dt, \tag{4}$$

where E_w is the wave energy per unit width (kg m/s^2), E_{pot} is the wave potential energy per unit width (kg m/s^2), ρ_w is the density of water (1000 kg/m^3), g is the acceleration of gravity (9.8 m/s^2), c is the wave velocity (m/s), η is the water surface elevation when the water body is still (m), and t is the time (s).

The energy of the landslide body can be calculated by using the Watts [24] formula:

$$E_s = \rho_s u^2 A, \tag{5}$$

where E_s is the energy of the landslide body per unit width (kg m/s^2), ρ_s is the density of the landslide body (kg/m^3), u is the water entry velocity of the landslide body (m/s), and A is the cross-sectional area of the landslide body (m^2). The wave energy conversion rate of the impulse waves is expressed by [25]

$$e_0 = \frac{E_w(0)}{E_s}, \tag{6}$$

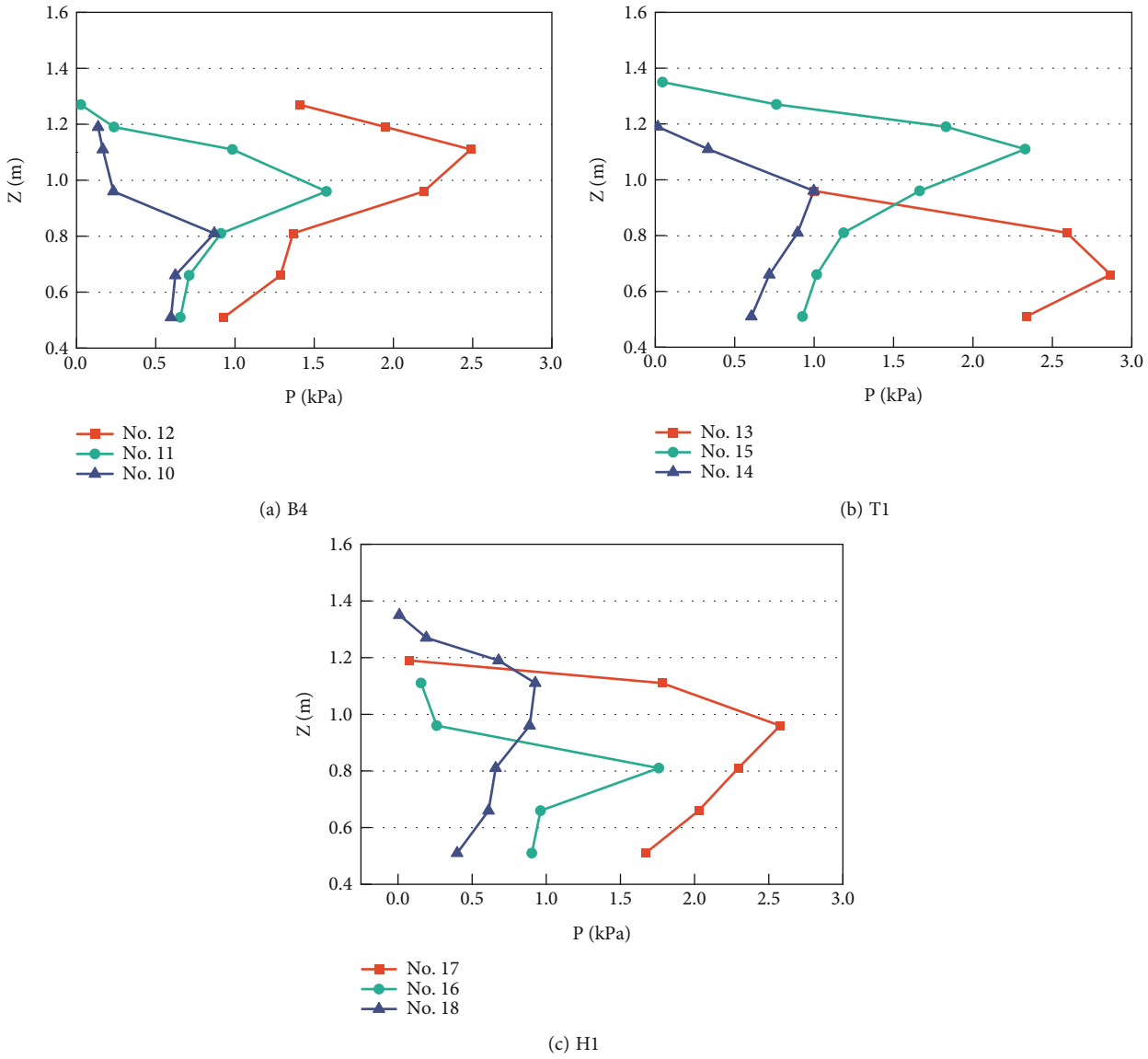

Figure 11: Impact pressure distributions from the impulse waves of landslide bodies B4, T1, and H1 on the opposite bank (Nos. 10–18).

where $E_w(0)$ is the wave energy in the near-field area of impulse wave generation. Figure 8 shows the changes in the energy conversion rate of the landslide-induced impulse waves at different Froude numbers according to the measurements of the wave height gauges. The energy conversion rate initially increased and then decreased as the Froude number F increased.

Figure 9 shows the changes in the wave energy according to the position of the wave height gauges for landslide bodies with different shapes. Tests 11, 15, and 16 all had the same water entry velocity and corresponded to landslide bodies with the shapes of B4, T1, and H1, respectively. T1 had the greatest wave energy, followed by H1 and then B4. Similarly, T2 showed the greatest propagation decay in the wave energy, followed by H1 and then B4. Therefore, landslide bodies with different shapes followed a similar law of energy propagation; however, the attenuation of the wave energy during the propagation process differed.

3.4. Impact Pressure Characteristics. The formation and propagation of landslide-induced waves in V-shaped river channels in alpine valleys are significantly affected by the slopes of the banks on both sides. The slope on the opposite bank constrains the huge kinetic energy generated by the impulse waves induced by the entry of the landslide body, so it cannot dissipate in time. This produces higher impulse waves that propagate to the opposite bank, which poses a huge threat to the safety of the local infrastructure and residents. Studying the impact pressure of landslide-induced waves on the banks of river channels is of great significance for preventing and controlling disasters.

In the physical model, eight pressure sensors were installed on the opposite bank. Impulse waves propagated to the opposite bank, and the impact pressure was measured by the sensors. Figure 10 shows the time history curve of the hydrodynamic pressure measured by sensors P1–P3 in test 13, which used landslide body T1. The waves reflected,

superimposed, and oscillated after they propagated to the opposite bank. The hydrodynamic pressure curves had the same wave amplitude, and the maximum value was affected by the water depth of the channel and the water entry velocity of the landslide body.

The influence of the shape of the landslide body, the water depth of the river channel, and the water entry velocity of the landslide body on the impact pressure distribution were investigated: three typical shapes of landslide bodies were selected—B4, T1, and H1. The water depth was set to 0.86, 1.10, and 1.26 m. The water entry velocity was set to 0.67, 1.16, and 1.67 m/s. Figure 11 shows the impact pressure distributions generated by landslide-induced waves. The impact pressure distributions generated by different shapes of landslide bodies generally had the same pattern. The main difference among the landslide bodies was in the frontal area that entered the water. For a given water entry velocity, a larger frontal area increased the impact pressure. The increase in the water entry velocity reduced the time for the landslide body to reach the bottom, which increased the amplitude of the waves that caused the impact pressure. At different water depths, the distributions of the maximum impact pressure on the opposite bank and the maximum amplitude of the impulse waves were generally the same. However, with the increasing water depth, the impact pressure distribution fluctuated at lower depths, indicating the complexity of the energy transfer when a landslide struck deep water.

The results indicate that the maximum dynamic water pressure is caused by the initial wave and that it follows an approximately triangular distribution along the water depth. The potential energy of the landslide body is instantaneously converted into kinetic energy after it enters the water, which applies a huge impact pressure on the water body. This pressure acts on the water body along the entire depth and generates impulse waves at the surface of the water body. The impulse waves propagate to the opposite bank as the potential energy is converted to kinetic energy. Because of the narrow dimensions of the V-shaped channel, the energy cannot dissipate in time, which increases the pressure transmitted to the opposite bank.

4. Conclusion

A physical model was used to perform 18 tests under different conditions to characterize the propagation of landslide-induced waves and the impact pressure distribution in V-shaped river channels in alpine valleys that contain major hydropower projects. The main conclusions are as follows:

(1) The impulse waveforms were all weakly nonlinear oscillatory waves. The waves generally formed an advancing wave train with positive amplitudes (wave crest) followed by oscillating waves with smaller amplitudes

(2) The results of the nonlinear regression analysis were used to propose a dimensionless equation for the amplitude of the first wave induced by a landslide in a V-shaped river channel. The prediction results obtained using the proposed equation showed a strong correlation with the observed results of the physical model at a correlation coefficient of 0.82

(3) An energy transformation law was obtained for landslide-induced impulse waves in a V-shaped river channel. The wave energy conversion rate initially increases and then decreases with an increasing Froude number. The shape of the landslide body does not significantly affect the energy propagation law but significantly affects the degree of wave energy attenuation

(4) The distribution of the maximum dynamic water pressure caused by landslide-induced waves in a V-shaped river channel on the opposite bank was obtained. The distribution is approximately triangular along the water depth; the pressure reaches a maximum value near the surface of the still water body and gradually decreases from the surface downward

Data Availability

An orthogonal design was adopted for the experiments with the physical model. The maximum wave amplitude, which corresponded to the maximum water entry velocity, was assumed to be the first wave amplitude. After the landslide-induced impulse waves propagated, the distance between the first two crests was measured and was taken as the wavelength. Table 1 presents the experimental design and results. The test parameters included the length (l), width (w), and thickness (s) of the landslide body, as well as the still water depth (h_0), sliding bed inclination angle (α), and water entry velocity of the landslide body (u). The results were represented by the Froude number (F), first wave amplitude (a), and wave velocity (c).

Conflicts of Interest

The authors declare no competing interests.

Acknowledgments

This work is supported by the National Natural Science Foundation of China (No. 51939004) and the Fundamental Research Funds for the Central Universities (No. B200204008). We are also deeply indebted and grateful and owe our thanks to the Guiyang Engineering Corporation Limited of PowerChina for assistance in the collection of engineering geological exploration data.

References

[1] H. M. Fritz, W. H. Hager, and H. E. Minor, "Landslide generated impulse waves," *Experiments in Fluids*, vol. 35, no. 6, pp. 505–519, 2003.

[2] S. T. Grilli and P. Watts, "Tsunami generation by submarine mass failure. I: modeling, experimental validation, and sensitivity analyses," *Journal of Waterway Port Coastal & Ocean Engineering*, vol. 131, no. 6, pp. 283–297, 2005.

[3] E. Noda, "Water waves generated by landslides," *Journal of the Waterways Harbors & Coastal Engineering Division*, vol. 96, no. 4, pp. 835–855, 1970.

[4] S. A. Rzadkiewicz, C. Mariotti, and P. Heinrich, "Modelling of submarine landslides and generated water waves," *Physics & Chemistry of the Earth*, vol. 21, no. 1, pp. 7–12, 1996.

[5] B. Ataie-Ashtiani and G. Shobeyri, "Numerical simulation of landslide impulsive waves by incompressible smoothed particle hydrodynamics," *International Journal for Numerical Methods in Fluids*, vol. 56, no. 2, pp. 209–232, 2010.

[6] H. Ersoy, M. Karahan, K. Gelili, A. Akgün, and B. K. Yahi, "Modelling of the landslide-induced impulse waves in the Artvin Dam reservoir by empirical approach and 3D numerical simulation," *Engineering Geology*, vol. 249, pp. 112–128, 2019.

[7] J. J. Wang, L. L. Xiao, S. N. Ward, and J. Du, "Tsunami squares modeling of the 2007 Dayantang landslide generated waves considering the effects in slide/water interactions," *Engineering Geology*, vol. 284, no. 1-2, article 106032, 2021.

[8] M. Rauter, L. Hoße, R. P. Mulligan, W. A. Take, and F. Løvholt, "Numerical simulation of impulse wave generation by idealized landslides with OpenFOAM," *Coastal Engineering*, vol. 165, article 103815, 2021.

[9] B. Ataie-Ashtiani and A. Nik-khah, "Impulsive waves caused by subaerial landslides," *Environmental Fluid Mechanics*, vol. 8, no. 3, pp. 263–280, 2008.

[10] H. M. Fritz, W. H. Hager, and H. E. Minor, "Landslide generated impulse waves. 2. Hydrodynamic impact craters," *Experiments in Fluids*, vol. 35, no. 6, pp. 520–532, 2003.

[11] V. Heller, W. H. Hager, and H. E. Minor, "Scale effects in subaerial landslide generated impulse waves," *Experiments in Fluids*, vol. 44, no. 5, pp. 691–703, 2008.

[12] B. L. Huang, Y. P. Yin, S. C. Wang et al., "A physical similarity model of an impulsive wave generated by Gongjiafang landslide in Three Gorges Reservoir, China," *Landslides*, vol. 11, no. 3, pp. 513–525, 2014.

[13] J. W. Kamphuis and R. J. Bowering, "Impulse waves generated by landslides," *Coastal Engineering*, vol. 1, pp. 575–588, 1971.

[14] S. B. Yue, M. J. Diao, and L. Wang, "Research on the initial shape and attenuation law of landslide surge," *Journal of Hydraulic Engineering*, vol. 47, no. 6, pp. 816–825, 2016.

[15] B. Ataie-Ashtiani and S. Malek-Mohammadi, "c," *Dam Engineering*, vol. 17, no. 4, pp. 197–222, 2007.

[16] B. L. Huang, Y. P. Yin, and J. M. Tan, "Risk assessment for landslide-induced impulse waves in the Three Gorges Reservoir, China," *Landslides*, vol. 16, no. 3, pp. 585–596, 2019.

[17] Z. G. Tao, Q. Geng, C. Zhu et al., "The mechanical mechanisms of large-scale toppling failure for counter-inclined rock slopes," *Journal of Geophysics and Engineering*, vol. 16, no. 3, pp. 541–558, 2019.

[18] Q. Yin, J. Y. Wu, Z. Jiang et al., "Investigating the effect of water quenching cycles on mechanical behaviors for granites after conventional triaxial compression," *Geomechanics and Geophysics for Geo-Energy and Geo-Resources*, vol. 8, no. 2, pp. 1–28, 2022.

[19] C. Zhu, X. D. Xu, X. T. Wang et al., "Experimental investigation on nonlinear flow anisotropy behavior in fracture media," *Geofluids*, vol. 2019, Article ID 5874849, 9 pages, 2019.

[20] V. Heller, W. H. Hager, and H. E. Minor, *Landslide generated impulse waves in reservoirs-basics and computation*, Editorial Aranzadi, 2009.

[21] H. J. Körner, "Reichweite und geschwindigkeit von bergstürzen und fließschneelawinen," *Rock Mechanics*, vol. 8, no. 4, pp. 225–256, 1976.

[22] B. L. Huang, S. C. Wang, and Y. B. Zhao, "Impulse waves in reservoirs generated by landslides into shallow water," *Coastal Engineering*, vol. 123, pp. 52–61, 2017.

[23] A. Zweifel, D. Zuccala, and D. Gatti, "Comparison between computed and experimentally generated impulse waves," *Journal of Hydraulic Engineering-ASCE*, vol. 133, no. 2, pp. 208–216, 2007.

[24] P. Watts, "Wavemaker curves for tsunamis generated by underwater landslides," *Journal of Waterway Port Coastal and Ocean Engineering*, vol. 124, no. 3, pp. 127–137, 1998.

[25] J. S. Walder, P. Watts, O. E. Sorensen, and K. Janssen, "Water waves generated by subaerial mass flows," *Journal of Geophysical Research: Solid Earth*, vol. 108, no. 5, pp. 2236–2255, 2003.

Hindawi
Geofluids
Volume 2022, Article ID 5201061, 13 pages
https://doi.org/10.1155/2022/5201061

Research Article

An Experimental Study on Mechanical Properties and Fracture Characteristics of Saturated Concrete under Coupling Effect of Low Temperature and Dynamic Load

Mengxiang Wang,[1,2] **Qi Zong**,[1] **and Haibo Wang**[1]

[1]*School of Civil Engineering and Architecture, Anhui University of Science and Technology, Huainan, 232001 Anhui, China*
[2]*Fujian Provincial Colleges and University Engineering Research Canter of Engineering Quality Testing and Safety Assessment, Longyan 364000, China*

Correspondence should be addressed to Mengxiang Wang; mxwang@aust.edu.cn

Received 21 July 2022; Revised 17 August 2022; Accepted 22 August 2022; Published 20 September 2022

Academic Editor: Yiding Bao

Concrete is widely used in bridge foundation, water supply, and drainage engineering. On the one hand, the saturated concrete is always in the saturated state. In the cold winter, northeast China and the alpine region suffer from freezing disaster. On the other hand, it has to continue to bear the dynamic load action of vehicles and running water, which makes the stress state of saturated concrete more complicated under the coupling action of low temperature and dynamic load. In order to study the mechanical properties and fracture characteristics of saturated concrete under the coupling effect of low temperature and dynamic load, the impact compression tests of concrete under normal temperature 20°C, -5°C, -10°C, and -15°C were carried out with a diameter of 74 mm split Hopkinson pressure bar (SHPB). The stress-strain characteristics, energy dissipation, and failure modes of specimens under different low temperatures were studied. From a detailed point of view, the failure mechanism of low-temperature water-saturated concrete is expounded. The results show that under the same dynamic load, the dynamic stress-strain curve of saturated concrete changes obviously with the change of low temperature. The dynamic compressive strength of the natural specimen at room temperature is high while that of the water-saturated specimen is low, and the dynamic compressive strength is opposite at low temperature. At the same temperature, the energy time-history curves of concrete in the saturated state are different from those in the natural state, mainly in the plastic section. The energy time-history curves of saturated concrete are different at different temperatures, and the energy dissipation rate of saturated concrete increases linearly with the decrease of temperature. Under the experimental conditions, the dynamic strength of saturated concrete increases linearly with the decrease of temperature, and the peak strain of saturated concrete decreases linearly with the increase of temperature. With the decrease of temperature, the fragmentation of saturated concrete under the impact of the same air pressure gradually increases, and the integrity of the specimen gradually improves. Low temperature can improve the impact resistance of saturated concrete, which is consistent with the failure law of natural state concrete. The water-saturated low-temperature state of the concrete void is filled with ice crystal particles; for low-temperature water-saturated concrete in the impact of the dynamic load, the microstructure is affected by the ice crystal structure which is not easy to change; the specimen along the axial force direction microdefect development produces a crack, the crack along the parallel to the pressure direction of cracking, through the two ends of the specimen, and finally produces axial splitting tensile damage. The research results have important theoretical significance for the safety design of low temperature saturated concrete structures.

1. Introduction

Concrete is a typical nonuniform material, widely used in the construction field, bridge foundation, water supply, and drainage engineering; concrete mechanical properties are greatly affected by temperature and humidity. During the construction of Qinghai-Tibet railway, the influence of low temperature environment on the mechanical properties of

concrete cannot be ignored [1–6]. The Nazixia Dam is located in a cold climate, and its concrete slabs are required to be stable at low temperatures [7]. In bridge foundation, water supply and drainage project, immersed concrete faces with frost heaving dangerous under low temperature state, while the structure should continue to bear the dynamic load of vehicles, running water, and so on. Therefore, it is of theoretical and engineering significance to study the mechanical properties and fracture characteristics of saturated concrete under the coupling action of low temperature and dynamic load.

Wang et al. carried out tests on the compressive strength of concrete cubes at -60°C~20°C, and the results showed that the compressive strength of concrete cubes increased linearly with the decrease of temperature within the test range [8]. Zhang e al. tested the compressive strength of concrete under -165°C~0°C and found that the growth was obvious between -40°C and -80°C, while the growth was slow after -120°C [9]. Dahmani et al. found that the properties of concrete at low temperatures are determined by porosity, and the strength of concrete decreases when subjected to freeze-thaw cycles [10]. Domestic scholars also tested the low temperature compressive strength of concrete mixed with different additives (such as rubber, polypropylene fiber, and asphalt) [11–13]. Fang et al. carried out bending-tension tests on ultrahigh performance concrete with discrete short fine steel fibers at -20°C and 20°C. It was found that with the decrease of temperature, the bond between steel fibers and concrete became stronger, the slip between them decreased, and the ductility became smaller [14].

The research on concrete performance at low temperature is mainly limited to static performance and freeze-thaw cycle. There are abundant research achievements on concrete impact test [15–18]. Zhu et al. cured basalt fiber concrete at -30°C and carried out a drop hammer test on the specimens at room temperature. It was found that basalt fiber could improve the impact resistance of concrete at low temperature, and there was a linear relationship between the fiber content and the impact resistance [19]. Huang and Xiao used a 155 mm large-diameter SHPB device to conduct impact compression tests on φ150 mm × 300 mm lightweight high-strength concrete. The failure of concrete specimens is mainly brittle failure. With the increase of impact velocity, the failure degree of specimens will gradually become higher [20]. Yan et al. conducted dynamic compression experiments on concrete with different initial damage degrees and found that the dynamic compressive strength of concrete decreased gradually with the increase of initial damage degrees. When the injury degree is less than 20%, the influence is more significant than 40% [21]. Many experts have also done a lot of research on water saturated concrete [22–24]. Sun et al. conducted acoustic emission test on rock, concrete, and rock concrete as one medium under uniaxial load under dry and saturated conditions and found that the peak value of impact number of saturated specimens was slightly behind that of stress [25]. Wang et al. on natural drying condition studied the water quality change of geological polymer concrete, ultrasonic wave velocity, compressive strength, flexural strength, and splitting strength and analyzed the saturated state of geological polymer (GC) basic physical and mechanical properties of concrete; the influence of saturated state of the GC static mechanics performance has obvious negative impact. Its compressive strength, flexural strength, and splitting strength are lower than those of dry condition [26].

In order to study the mechanical properties and fracture characteristics of saturated concrete under the coupling effect of low temperature and dynamic load, low temperature and saturated concrete were taken as the research object. Impact compression tests of concrete under normal temperature (-5°C, -10°C and -15°C), saturated water, and natural state were carried out by using a diameter of 74 mm split Hopkinson pressure bar (SHPB). The dynamic stress-strain characteristics and failure modes of saturated concrete in different low temperature states were studied, and the dynamic strength, peak strain, absorption energy, and fracture characteristics of specimens were analyzed with low temperature. Compared with natural concrete, the research results have important theoretical significance for the safety design of low temperature saturated concrete structures.

2. Test Design

2.1. Specimen Making and Scheme. Ordinary Portland cement was chosen to cast C40 concrete in the test. The cement is P·O 42.5 ordinary Portland cement produced by Huainan Bagongshan Cement Factory. Gravel for artificial gravel has a nominal particle size of 5~15 mm (continuous grading). Sand is medium fine sand, and particle grade is good, with over 1 mm sieve. Use ordinary tap water. The water-cement ratio of concrete is 0.46, and the mixing ratio C : W : S : G = 1 : 0.46 : 1.48 : 2.20. Concrete was poured with a rectangular template and vibrated with a shaking table. According to the GB/50081-2002 standard, concrete curing is done at temperature of 20 ± 2°C, and relative humidity of >95%. After standard curing for 28 days, the cylinder was taken out, cut, and polished by ZS-100 vertical drilling core machine, and a cylinder specimen of φ 74 mm × 37 mm was obtained, as shown in Figure 1.

In this experiment, two kinds of concrete in saturated and natural state were adopted, and low water-saturated concrete was taken as the main object of study. After 28 days of maintenance, the specimen is treated with water, and in order to ensure that the specimen is in a full state, it is soaked under negative pressure for 72 hours. The freeze-thaw box (as shown in Figure 2) was used to deal with the temperature of the two kinds of concrete at room temperature (-5°C, -10°C, and -15°C). Due to the large discreteness of dynamic experiment, in order to ensure the repeatability of experimental results, five concrete test blocks were selected under the same curing condition during the impact compression test of the sample. Because concrete is thermal inert material, in order to ensure that the temperature of the specimen does not change too much in the test process, a simple insulation box is made, together with the sample into the low-temperature curing box. The test block is then placed into a sealed bag, then put into salt water, and frozen;

Figure 1: Partial sample.

Figure 2: Freeze-thaw box.

the test block is put into the refrigerator; the internal temperature stabilization of the refrigerator requires a process; when the specimen reaches the set temperature, it needs to be stable for 24 hours, so the freezing time is set to 48 hours. During the experiment, it was taken out together with the foam box, and the impact test was carried out quickly to reduce the heat loss inside the concrete specimen and to ensure that the temperature was kept in the effective range during the experiment as far as possible. Before the experiment, the temperature in the simple foam box was measured to meet the requirements of the test temperature.

2.2. Test Device and Test Method. The 74 mm diameter variable section SHPB test device of Anhui University of Science and Technology was used in the impact test, as shown in Figure 3. The length of the impact bar was 0.60 m, and the lengths of the incident bar and transmission bar were 2.40 m and 1.20 m, respectively. The impact bar, incident bar, transmission bar, and absorption bar are all alloy steel with a density of 7.8 g/cm^3, elastic modulus of 210 GPa, and p-wave velocity of 5190 m/s. The type of resistance strain gauge used to collect voltage signals on the incident bar and transmission bar is BX120-2AA, and the strain gauge grid length is 2 mm, which can meet the requirements of dynamic measurement accuracy. CS-1D dynamic strain gauge and TST 3406 dynamic test analyzer were used for data signal acquisition.

Based on one-dimensional stress wave propagation theory, a two-wave method is used to calculate the stress, strain, and strain rate of specimen under impact [27].

$$\begin{cases} \dot{\varepsilon}(t) = \dfrac{2C_0}{l_s}\varepsilon_r(t), \\ \varepsilon(t) = \dfrac{2C_0}{l_s}\displaystyle\int_0^t \varepsilon_r(t)dt, \\ \sigma(t) = \dfrac{A_0E_0}{2A_S}\varepsilon_t(t). \end{cases} \tag{1}$$

The energy carried by incident, reflected, and transmitted waves can be expressed by the following formula [27]:

$$\begin{cases} W_i(t) = AEC_0\displaystyle\int_0^t \varepsilon_i{}^2(t)dt, \\ W_r(t) = AEC_0\displaystyle\int_0^t \varepsilon_r{}^2(t)dt, \\ W_t(t) = AEC_0\displaystyle\int_0^t \varepsilon_t{}^2(t)dt. \end{cases} \tag{2}$$

The dissipated energy of the specimen is expressed as [27]

$$W_A(t) = W_i(t) - W_r(t) - W_t(t). \tag{3}$$

Under different environments, the energy dissipation rate of specimens directly reflects the strength of energy dissipation. The energy dissipation rate can be defined as the ratio of the dissipated energy of specimens to the incident energy [27].

$$\eta = \frac{W_A(t)}{W_i(t)}, \tag{4}$$

where $\varepsilon_i(t)$, $\varepsilon_r(t)$, and $\varepsilon_t(t)$ are the incident strain, reflected strain, and transmitted strain at time t, respectively, dimensionless; l_s is the thickness of specimen (m); C_0, E are the compressional wave velocity and elastic modulus of the compression bar (m/s and MPa), respectively; A, A_S are the cross-sectional area of the pressure bar and the cross-sectional area of the specimen (m^2); and W_i is incident energy, W_r is reflected energy, W_t is transmitted energy, and W_t is dissipated energy (J).

3. Test Results and Analysis

3.1. Stress-Strain Curves of Specimens. In order to control the variables and study the influence of low temperature on the dynamic mechanical properties of saturated concrete, 0.25 MPa air pressure was used to impact the specimen in the test. The stress-strain curve of low-temperature and saturated concrete is shown in Figure 4, and that of low-temperature and natural concrete is shown in Figure 5.

In order to better explain the characteristics of saturated water concrete under the coupling action of low temperature and dynamic load, the dynamic stress-strain curve of low-temperature concrete specimen (natural) in Figure 5 is

Figure 3: SHPB test device with variable cross section of 74 mm diameter.

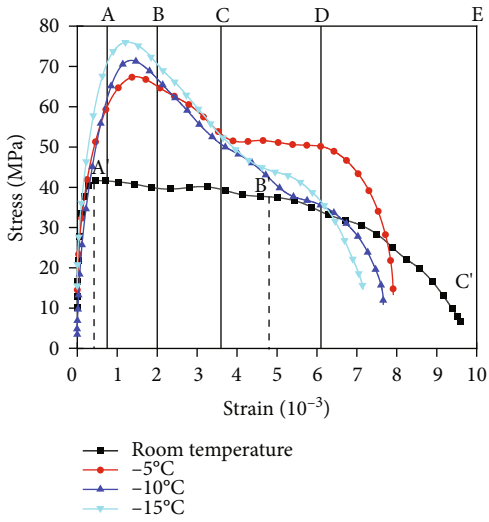

Figure 4: Dynamic stress-strain curve of frozen concrete elements (saturated).

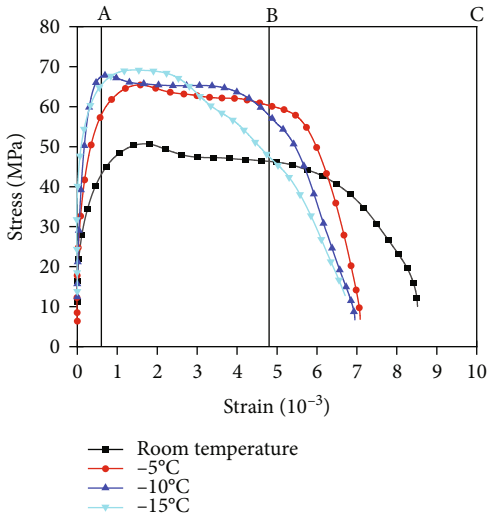

Figure 5: Dynamic stress-strain curve of frozen concrete elements (natural).

compared. It can be seen that under the condition of the same coupling value of low temperature and dynamic load, the dynamic stress-strain curve of saturated concrete changes obviously from that under natural state. The most significant difference can be seen from the stress peak value. At normal temperature, the dynamic strength peak value of saturated concrete is lower than that of natural state, while at low temperature, the strength peak value of saturated concrete is higher than that of natural state. It can also be seen from the stress-strain curve that concrete under different temperatures in the natural state has obvious dynamic yield platform stage, while concrete under normal temperature under saturated state and concrete under natural state both have obvious yield platform stage. However, at low temperature, the platform at the yield stage of saturated concrete is not obvious and becomes "steeper." In order to further reveal the characteristics of saturated concrete under the coupling action of low temperature and dynamic load, the dynamic stress-strain curve of low-temperature and saturated concrete in Figure 4 was analyzed in detail.

It can be seen from Figure 4 that the dynamic stress-strain curve of low-water-saturated concrete mainly includes three stages. (1) The OA stage in Figure 4 is stress-increasing stage, where the stress-strain curve is linear elastic stage. The crack in concrete gradually develops. When approaching to elastic limit, the strain increases fast. (2) In the second stage of stress decline, the stress plateau gradually decreases at normal temperature, while the stress rapidly decreases at low temperature and then decreases slowly at CD. The main reason is that with the penetration of microcracks, the internal integrity of the specimen structure is aggravated, the load transfer route is constantly reduced, and the bearing capacity decreases. At room temperature, the water particles in saturated concrete play a lubricating role in the bite force and friction between concrete and aggregate, so that the force is more uniform. For low-water-saturated concrete, the crack is filled with ice, which makes the strength of concrete increases. Hence, the strength of the concrete specimen with decreasing of temperature. Due to the increase of ice body, the original porous concrete medium is filled with brittle ice body, but after the late decline, there is a small area of slow decline. The analysis of the reason mainly considers that in the process of crack propagation, the occluded and frictional energy generated between aggregates will weaken the freezing effect of ice body and produce certain deformation under the action of stress. (3) In the DE section of specimen stress rapid decline stage, as the specimen cracks, the specimen is broken and the cohesion of the structure is almost exhausted.

3.2. Energy Time History Curve of Concrete Specimens with Low Water and Sufficient Water. Dynamic mechanical properties and energy calculation results of impact specimens are

Table 1: Test conditions and calculation results.

No.	Water content	Temperature (°C)	Height (mm)	Diameter (mm)	Dynamic compressive strength (MPa)	Strain rate (s^{-1})	Peak strain (10^{-3})	Incident energy (J)	Reflected energy (J)	Transmission energy (J)	Absorbed energy (J)	Energy dissipating rate-η (%)
5-1	Saturated	Room temperature	38.02	75.51	40.16	40.05	9.60	33.87	22.70	0.38	10.79	31.86
5-2			38.49	75.69	42.70	40.15	9.12	33.88	22.14	0.42	11.32	33.41
5-3			38.12	75.44	41.59	40.29	9.54	33.45	21.98	0.46	10.89	32.56
6-1		-5°C	38.28	75.77	67.44	38.57	7.91	33.19	15.86	0.93	16.4	49.41
6-2			38.56	75.46	68.50	38.41	8.01	33.46	15.79	0.95	16.72	49.97
6-3			38.99	75.66	65.20	38.65	7.95	33.52	16.01	0.99	16.52	49.28
7-1		-10°C	38.48	75.39	71.49	37.54	7.66	33.61	14.2	0.83	18.58	55.28
7-2			38.18	75.89	73.16	37.23	7.81	33.63	14.92	0.85	17.86	53.11
7-3			38.96	75.46	69.23	37.46	7.58	33.24	13.98	0.86	18.4	55.35
8-1		-15°C	38.28	75.61	76.02	36.99	7.15	33.38	12.79	0.85	19.74	59.14
8-2			38.56	75.69	75.42	37.05	7.49	33.94	12.06	0.82	21.06	62.05
8-3			38.46	75.44	78.12	36.95	7.12	33.78	12.86	0.81	20.11	59.53
1-1	Natural	Room temperature	38.48	75.67	50.69	39.96	8.51	33.04	18.65	0.51	13.88	42.01
1-2			38.20	75.78	49.15	39.04	8.01	33.44	19.04	0.49	13.91	41.60
1-3			38.94	75.98	51.20	39.55	7.89	33.64	18.05	0.47	15.12	44.95
2-1		-5°C	38.44	75.47	65.41	37.57	7.08	33.42	14.13	0.96	18.33	54.85
2-2			38.23	75.46	64.13	38.01	7.14	33.41	14.88	0.94	17.59	52.65
2-3			38.41	75.66	63.21	38.12	7.35	33.59	14.56	0.95	17.76	52.87
3-1		-10°C	38.82	75.28	67.85	37.05	6.94	33.80	13.40	0.96	19.44	57.51
3-2			38.16	75.14	69.12	36.85	6.82	33.45	13.12	0.92	18.64	55.72
3-3			38.51	75.29	65.33	36.97	7.01	33.94	13.89	0.91	19.14	56.39
4-1		-15°C	38.44	75.39	69.17	36.85	6.70	33.05	11.88	0.90	20.27	61.33
4-2			38.65	75.44	68.24	36.47	6.65	33.46	11.99	0.89	20.58	61.51
4-3			38.21	75.02	70.94	36.59	6.59	33.01	12.24	0.88	19.89	60.25

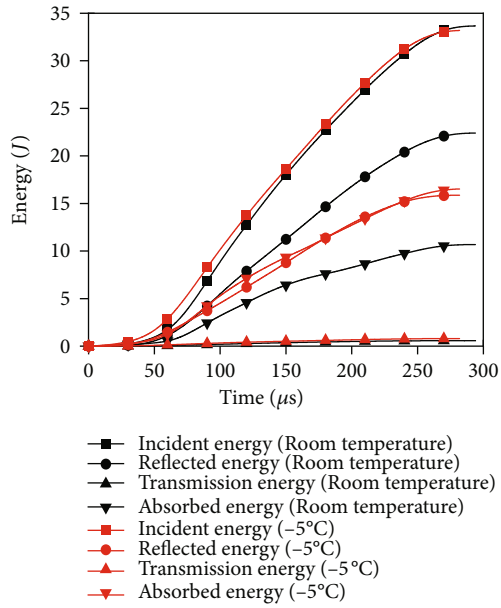

Figure 6: Energy distribution of saturated concrete.

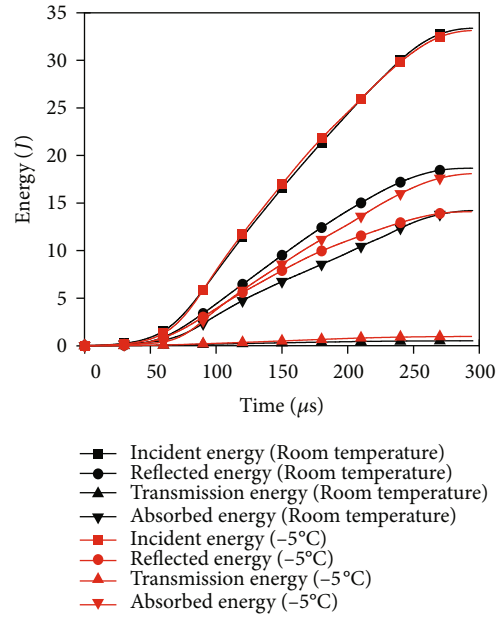

Figure 7: Energy distribution of natural concrete.

shown in Table 1 through data processing and theoretical calculation. Under the action of the same impingement air pressure, the relationship between incident energy, reflected energy, transmitted energy, and time of saturated concrete and natural concrete at room temperature and -5°C is shown in Figures 6 and 7.

It can be seen from Figures 6 and 7 that the initial kinetic energy obtained by bullets under the action of the same air pressure is the same, so the impact incident energy of the specimen is approximately the same, which also indicates the reliability of the test equipment. It can be seen from the figure that all kinds of energies increase with the increase of acting time, and the energy changes are not obvious between 0 and 50 μs. After 50 μs, the growth slope of absorbed and reflected energy is faster than that of transmitted energy. For saturated concrete at normal temperature, the reflected energy is higher than that at -5°C, and the transmitted energy is lower than that at -5°C, as shown in Figure 6 according to the conservation of energy. Satisfying the water absorption of low-temperature concrete is greater than the normal temperature condition, the natural conditions at room temperature, and low temperature state energy time history curve with a similar pattern, size is not the same, but the energy difference is also different. The difference between the reflected energy and absorbed energy of water-saturated concrete at room temperature is large, but the maximum absorbed energy of water-saturated concrete at -5°C is slightly larger than the reflected energy. However, for the same temperature, the value of reflected energy is greater than that of absorbed energy. The above results show that the saturated state has significant influence on the energy dissipation of concrete at both room temperature and low temperature.

3.3. Relationship between Temperature and Dynamic Compressive Strength and Peak Strain of Water-Saturated Specimens. From the analysis of Section 2.2 and Table 1, it can be seen that the water-saturated state has a greater impact on the strength of concrete, and it can be seen from the table that the ratio of the strength of the water-saturated concrete to the strength of the natural state is 0.82, indicating that the water-saturated water molecules have a deteriorating effect on the dynamic strength of the concrete, and when the temperature reaches -15°C, the strength ratio of the water-saturated concrete to the strength in the natural state is 1.10, indicating that the transformation of water molecules into ice molecules has a certain enhancement effect on the dynamic strength of the concrete. There is a certain low temperature state that can compensate for the deterioration effect of saturation. In order to further reveal the relationship between the dynamic strength of water-saturated concrete under low temperature and dynamic load and the relationship between peak strain and low temperature of water-saturated concrete under low temperature and dynamic load, the law of concrete under water-saturated state is more detailed, and the relationship between low-temperature dynamic compressive strength and peak strain of natural concrete is compared and analyzed, and the relationship between dynamic compressive strength and peak strain and temperature of water-saturated concrete is obtained as shown in Figures 8 and 9.

It can be seen from Figure 8 that under test conditions, the dynamic strength of saturated concrete increases linearly with the decrease of temperature. After linear fitting of data, the linear correlation coefficient between dynamic strength of saturated concrete and temperature is $R^2 = 0.998$. The dynamic compressive strength of saturated concrete increases by 34.37 MPa when it drops from normal temperature to -15°C. Compared with the natural state, state full water dynamic compressive strength of concrete under normal temperature is low, the analysis reason mainly is a kind

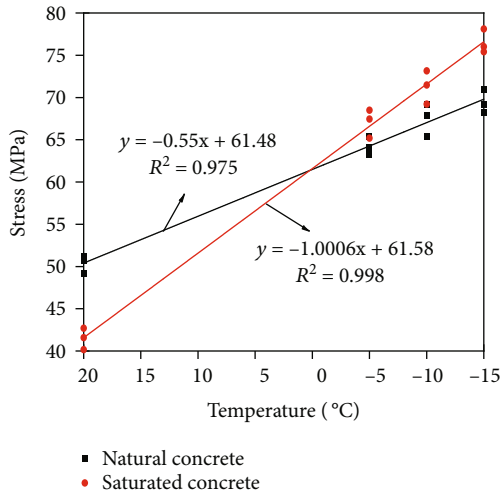

Figure 8: Relationship between dynamic strength and temperature of saturated concrete.

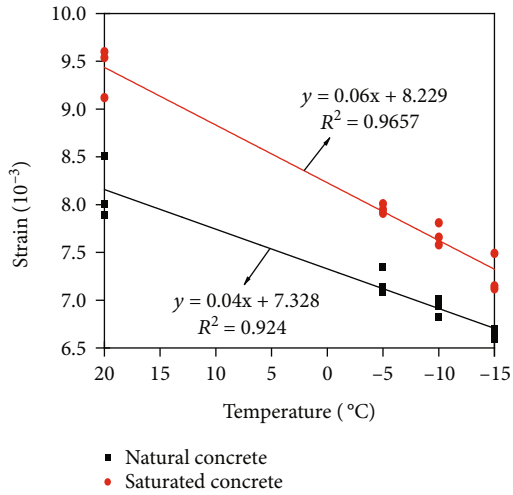

Figure 9: Relationship between peak strain and temperature of saturated concrete.

of porous concrete is hydrophilic material, feed water condition of concrete softening of water particles and lubrication, and creep tendency, so that normal temperature state full of water dynamic compressive strength of concrete material has weakened a lot. As the temperature decreases, it can be seen from the fitting curve that the dynamic compressive strength of concrete under saturated water is equivalent to that under natural state between 0°C~-2°C. However, the effect of temperature is not considered in the test, but the results are reliable combined with theoretical analysis. When the temperature is lower than 0°C, the free water in concrete turns into ice crystal. On the one hand, the crystal has a certain strength to fill the void of concrete; on the other hand, the process of freezing water into ice under the effect of low temperature increases the cohesion and internal friction angle of the specimen itself, which weakens the softening and lubrication effect of water together. Within the test range, when the temperature reaches lower temperature, the dynamic strength of saturated concrete increases, and the main reason can be explained by the model of friction crack slip [28–35]. Concrete is subject to impact load, cracks will develop and extend from the microcracks in the specimen, and for this moment, the concrete can still withstand a large load; cracks in the development and extension of the original cracks will produce friction slip between the cracks that have been generated. Concrete friction slip needs to overcome the following aspects of resistance: (1) the adhesion force between the two friction surfaces and (2) the resistance encountered when the concave and convex particles cross each other, which is closely related to the roughness of the friction surface, and for the destruction of low-temperature water-saturated concrete, the ice crystal structure will increase the adhesion of the friction face and will also increase the roughness of the friction surface. In the crack propagation, the friction resistance of ice crystal structure slip is the most important factor. The lower the temperature is, the greater the friction resistance of slip is, and the higher the stress of crack initiation and growth is, and the compressive strength also increases. The schematic diagram of the slip model is shown in Figure 10.

Considering the linear increase of concrete with temperature decrease in natural state, the correlation coefficient of fitting is $R^2 = 0.991$. At -15°C, the peak value dynamic compressive strength of concrete increases by 18.48 MPa. It can be seen that the effect of peak compressive strength of saturated concrete changing with temperature is significantly higher than that of dry concrete. According to Figure 10, the concrete material itself has many holes in the natural state. Under the impact load, the crack propagation in the concrete preferentially passes through the weak surface and holes of the specimen, and the crack penetrates the weak surface and holes along the stress direction. For saturated concrete, due to lubrication and softening, the energy consumed by cracks running through concrete is weakened. For the same crack, the energy required is smaller, and the overall bearing capacity of saturated concrete specimens is reduced. However, at low temperature, the water in the holes and voids of saturated concrete is filled with ice crystals, and the filling strength of ice crystals is higher, which makes the failure mode of concrete more inclined to axial splitting and tensile failure. The crack produced by the specimen is more parallel to the stress path, which reduces the guiding effect of the weak face on the crack propagation, thus improving the strength of the specimen as a whole.

Based on the relationship between peak strain and temperature of saturated concrete in Figure 9, it can be seen that the peak strain of saturated concrete decreases linearly with the increase of temperature, and the linear correlation coefficient is $R^2 = 0.97$. For concrete under natural condition, the peak strain of saturated concrete is always greater than that of concrete under natural condition when it drops from normal temperature to -15°C in the test range. However, the change rate of peak strain with temperature of saturated concrete (slope 0.06) is larger than that of natural concrete (slope 0.04). It can be seen that with the continuous decrease

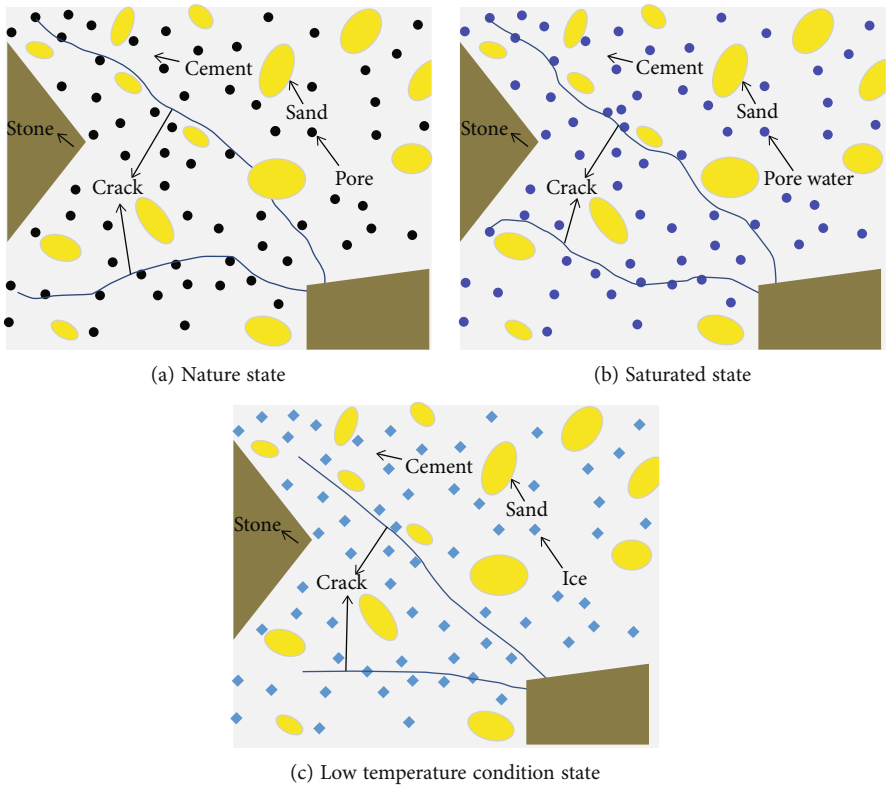

(a) Nature state

(b) Saturated state

(c) Low temperature condition state

Figure 10: Schematic diagram of failure model of water-saturated concrete.

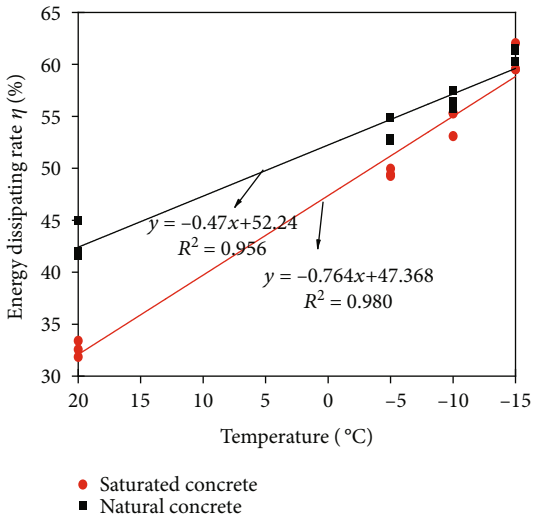

Figure 11: Relationship between energy dissipation rate of water-saturated concrete and temperature.

of temperature, the peak strain of saturated concrete will be smaller than that of concrete under natural state. The main reasons are as follows: first, with the decrease of temperature, the brittleness of ice crystal structure in saturated concrete becomes stronger. At the same time, considering the frost heave effect of ice crystal structure, the strength of saturated concrete increases within the test temperature range, and free water is mainly frozen inside the structure, which mainly produces filling and solidification. Second, with the decrease of temperature, the bound water inside the structure, including aggregate and sand, will also freeze, which will cause frost heave damage to the structure. Therefore, with the continuous decrease of temperature, the dynamic limit strain of saturated concrete will gradually decrease [36].

3.4. The Relationship between Energy Dissipation Rate and Temperature. Under different environments, the energy dissipation rate of specimens directly reflects the strength of energy dissipation. Based on Table 1, the relationship between the energy dissipation rate of saturated concrete and temperature is shown in Figure 11.

Figure 11 shows that the energy dissipation rate of saturated concrete increases linearly with the decrease of temperature, and the linear correlation coefficient $R^2 = 0.98$. Combined with Figure 6, the failure energy absorption process of saturated concrete specimens was analyzed from the perspective of absorbed energy and energy dissipation. In the initial stage of impact, the stress wave was in the rising edge, and the saturated concrete specimens were in the stage of elastic deformation. The absorbed energy of saturated concrete was stored in the form of elastic energy. With the increase of incident energy, due to the wave impedance mismatch between the specimen and the pressure bar, the incident end face of the specimen generates reflection energy, and the poststress wave propagates back and forth through the specimen in the transmission bar, specimen, and incident bar, and each energy is supplemented. As the stress wave strength is greater than the ultimate compressive

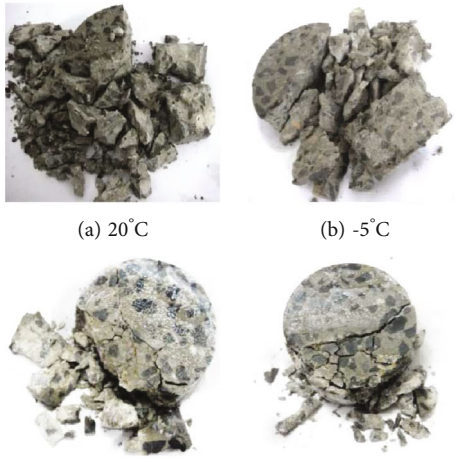

(a) 20°C (b) -5°C

(c) -10°C (d) -15°C

Figure 12: Failure pattern of water-filled concrete.

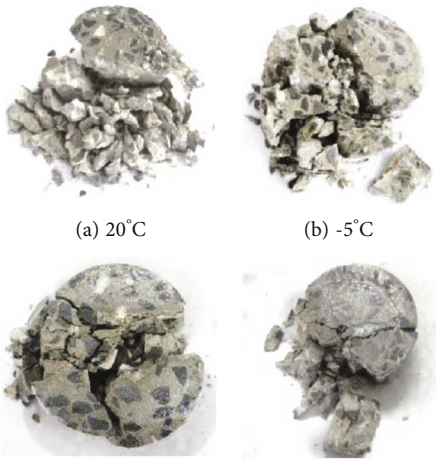

(a) 20°C (b) -5°C

(c) -10°C (d) -15°C

Figure 13: Failure pattern of natural concrete.

strength of saturated concrete, damage evolution and accumulation will occur in the saturated concrete specimen. The primary microcracks in saturated concrete expand and produce a large number of new microcracks at the same time, and the absorption energy continues to increase, which is also the main stage of energy dissipation. With lower temperature, the microcracks of concrete internal full water, microdefects by ice crystals, and low temperature damage will not be able to make full water concrete according to the original crack, weak surface development, and thus need to consume more energy, but with the lower temperature, feed water concrete and concrete energy dissipation is gradually close to nature.

The main reason is that with the decrease of temperature, regardless of saturated concrete and concrete in natural state, the bound water inside the structure, including aggregate, sand, and other internal water, also freezes, and the overall brittleness of the specimen becomes stronger. The dynamic compressive strength of concrete with low water and sufficient water will increase, but it is more likely to be broken, and the overall energy dissipation rate will tend to be the same when the ultimate strain decreases.

3.5. Fracture Morphology Characteristics. Figures 12 and 13 show the failure patterns of concrete in low water and full water and concrete in natural state at different temperatures.

It can be seen from Figure 12 that, under the impact of the same air pressure, the fragmentation of saturated concrete gradually increases with the decrease of temperature, and the integrity of specimens gradually improves. The decrease of temperature can improve the impact resistance of saturated concrete, which is consistent with the failure law of natural state concrete. The axial splitting tensile failure and compression shear failure of concrete specimens with low temperature and adequate water are the main. As the temperature decreases, the crushing state changes from crushing to axial splitting failure, and the axial through-crack gradually decreases. Saturated concrete is seriously

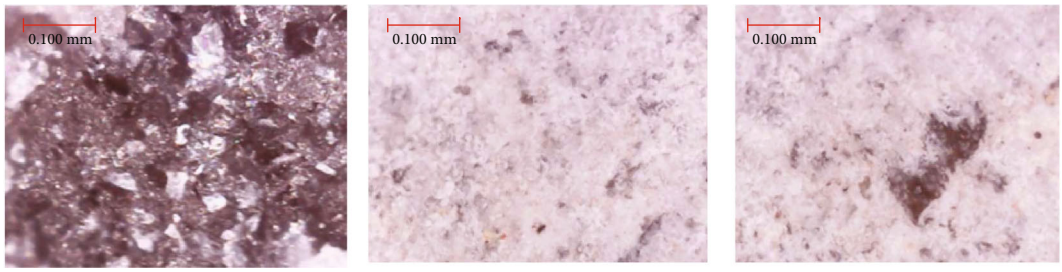

(A) Aggregate meso structure (B) Cement meso structure (C) Cement and mortar meso structure

(a) Mesostructure of concrete surface in natural state

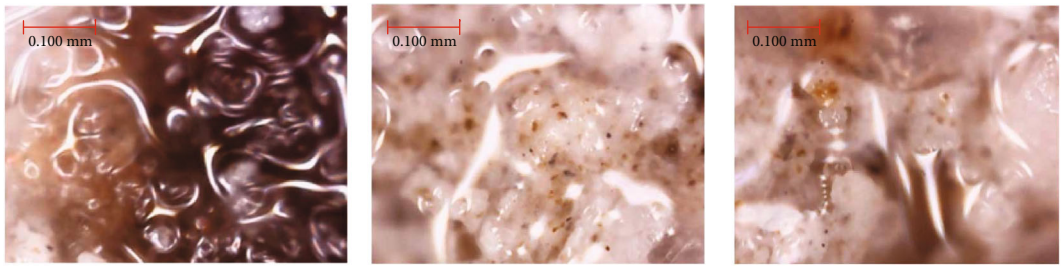

(A) Aggregate meso structure (B) Cement meso structure (C) Cement and mortar meso structure

(b) Mesostructure of concrete surface under saturated state

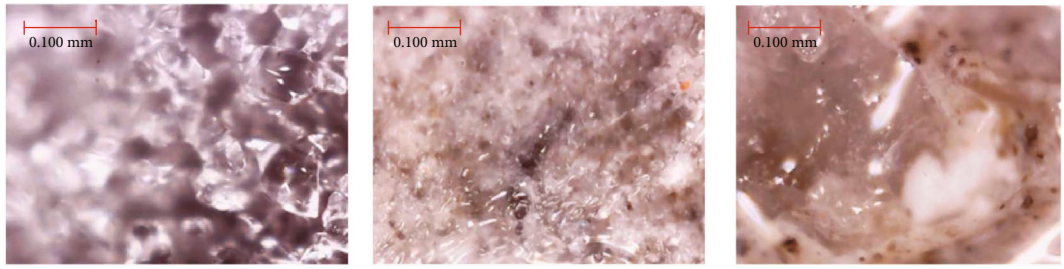

(A) Aggregate meso structure (B) Cement meso structure (C) Cement and mortar meso structure

(c) Microstructure of frozen concrete surface under saturated condition

Figure 14: Failure pattern of concrete.

broken at room temperature, and the destruction range at low temperature is smaller than that at natural state. Based on the mesostructure of concrete, the damage and evolution of saturated concrete are studied by analyzing the physical and mechanical process of the change of mesostructure, which can well reveal the damage mechanism and law of saturated concrete. In order to reveal the mesostructure of fracture and fracture of low water-saturated concrete, the surface of water-saturated concrete specimen was observed by a bester electronic digital microscope with magnification of 1000 times. The observations are shown in Figure 14.

It can be seen from Figure 14 that there are a large number of voids and defects (such as cavities, holes, and microcracks) in concrete in the natural state. In the saturated state, voids and microcracks are filled by water, as shown in Figure 14(b). In the water-saturated low temperature state, the surface of concrete is filled with ice crystal particles, but the ice crystal particles do not completely fill and fill the pores and voids as expected. That is mainly because the process of freezing water does not just freeze at zero degrees Celsius. To turn water molecules into ice crystals, they need an attachment called a nucleus. For saturated concrete, water molecules will preferentially form lattice on the contact surface with concrete, sand, and cement and form ice body structure on this basis. Therefore, the ice body of saturated mortar does not always fill the pores. However, due to the action of ice crystals, the weak surface of concrete is effectively connected. Therefore, under the impact load, the dynamic process of concrete defects in the natural state is intensified, and microdefects in different parts of the interior are simultaneously activated and developed, resulting in a small number of cracks. Under the continuous action of stress waves, a large number of microdamage and microcrack development, coupled with the development of internal structural defects, will produce cracks in the internal structure of particles, along the cracks between particles and grain boundaries. However, the microstructure of concrete subjected to impact dynamic load is not easily changed by ice crystal structure, and the distribution of concrete will change from a free state to directional distribution under stress direction. When the specimen is subjected to uniaxial impact compression, after the stress wave reaches the

contact surface between the incident bar and the specimen, the effective stress in all parts of the specimen is uniform with the propagation of the stress wave in the concrete with low temperature and adequate water. With the further increase of the axial stress, the microdefects of the specimen develop along the axial stress direction and produce cracks. The cracks occur along the direction parallel to the compressive stress direction, through the two ends of the specimen, and produce axial splitting tensile failure.

4. Conclusions

In bridge foundation, water supply, and drainage project, immersed concrete faces frost heaving dangers under low-temperature state. Additionally, the concrete also faces dynamic failure, when many cars drive on it. Hence, the mechanics characteristics of water-saturated concrete under the coupling of low temperature and dynamic load are studied. Water saturation and dry concrete impact compression tests were conducted at a normal temperature of -5°C, -10°C, and -15°C using Φ74 mm split Hopkinson pressure rod (SHPB). The following conclusions are reached:

(1) In the case of the same coupling value of low temperature and dynamic load, under normal temperature, the strength ratio of water-saturated concrete to natural state is 0.82, and the water molecules in the water-saturated state have a deteriorating effect on the dynamic strength of concrete, and when the temperature reaches -15°C, the strength ratio of water-saturated concrete to the strength in natural state is 1.10, and the transformation of water molecules into ice crystal structures has a certain enhancement effect on the dynamic strength of concrete. Under different temperatures, concrete in the natural state and the natural state of normal temperature and water-saturated concrete have obvious dynamic yield platform stage, but at low temperature, the yield stage of water-saturated concrete platform is not obvious, and the material properties become more and more "steep" and brittle

(2) In the range of the test, the various energies increase with the time of action. There is no obvious change of each energy between 0 and 50 μs. After 50 μs, the increase slope of absorbed and reflected energy is faster than that of transmitted energy. For saturated concrete at room temperature, the reflection energy is higher than -5°C, and the transmission energy is lower than -5°C. The energy dissipation rate of saturated concrete increases linearly with the decrease of temperature

(3) Under the experimental conditions, the dynamic strength of saturated concrete increases linearly with the decrease of temperature, and the dynamic compressive strength of saturated concrete increases by 34.37 MPa when the temperature drops from 20°C to -15°C at normal temperature. The peak strain of saturated concrete decreases linearly with the increase of temperature. For concrete under natural condition, the peak strain of saturated concrete is always greater than that of concrete under natural condition when it drops from normal temperature to -15°C within the test range. However, the change rate of peak strain with temperature of saturated concrete (slope 0.06) is larger than that of natural concrete (slope 0.04).

(4) The results of the thesis study have certain theoretical reference value for the design, construction, maintenance and reinforcement of bridge foundation concrete, water supply, and drainage engineering building structures and outdoor low-temperature concrete pavement in cold areas, and for concrete structures that need to be built in water and withstand dynamic load, it should be selected to increase silicon powder and other fine admixtures to reduce bubbles in concrete, or to select concrete with higher strength labels to reduce the effect of saturation deterioration. For the water-saturated concrete structure in the cold area, although under the action of low temperature dynamic load, the strength of the concrete increases, but the brittleness of the concrete increases, especially for some important structures, the sudden instability of the brittle damage is unpredictable, which will bring very serious disasters, for these places should improve the reinforcement rate of the concrete structure or increase the steel fiber; carbon fiber, polyester fiber, etc. can improve the overall ductility of the concrete under the condition of ensuring the strength of the concrete

Data Availability

All data included in this study are available upon request by contact with the corresponding author.

Conflicts of Interest

The authors declare no conflict of interest.

Acknowledgments

This work was supported by Anhui Province Key Laboratory of Building Structure and Underground Engineering, Anhui Jianzhu University, Hefei (KLBSUE-2022-03), and the High-Level Talent Introduction Scientific Research Start-Up Fund of Anhui University of Science and Technology.

References

[1] Y. J. Xie, W. Liu, B. J. Liu, and X. Feng, "Experimental study of com-pressive strength of early-strength con crete cured under low temperatures for Qinghai-Tibet railway," *Bridge Construction*, vol. 2, p. 27, 2003.

[2] L. P. Gu, "Quality control of low(minus)-temperature, early-strength and high-performance concrete of Qinghai-Tibet railway project in frozen plateau area," *Journal of Railway Engineering Society*, vol. 1, pp. 34–38, 2004.

[3] T. J. MacLean and A. Lloyd, "Compressive stress–strain response of concrete exposed to low temperatures," *Journal of Cold Regions Engineering*, vol. 33, no. 4, 2019.

[4] J. Xie, X. M. Li, and H. H. Wu, "Experimental study on the axial-compression performance of concrete at cryogenic temperatures," *Construction and Building Materials*, vol. 72, pp. 380–388, 2014.

[5] S. L. Gao and P. X. Xie, "Effect of temperatures and moisture content on the fracture properties of engineered cementitious composites (ECC)," *Materials*, vol. 15, no. 7, pp. 2604–2604, 2022.

[6] J. J. Guo, Z. Zhang, J. J. Wu et al., "Early-age mechanical characteristics and microstructure of concrete containing mineral admixtures under the environment of low humidity and large temperature variation," *Materials (Basel)*, vol. 14, no. 17, p. 5085, 2021.

[7] C. Y. Xu, Y. Qin, M. Li, and H. M. Liu, "Service performance analysis and stability evaluation of concrete face slab of Nazixia Dam," *Engineering Journal of Wuhan University*, vol. 53, no. 7, pp. 565–573, 2020.

[8] C. X. Wang, J. Xie, and H. J. Li, "Experimental research on the properties of concrete under low-temperature," *Engineering Mechanics*, vol. 28, no. S2, pp. 182–186, 2011.

[9] N. Zhang, J. Liao, W. Z. Ji, B. H. Wang, D. H. Zhang, and Y. W. Li, "Low temperature mechanical properties and test methods of concrete," *Journal of the Chinese Ceramic Society*, vol. 42, no. 11, pp. 1404–1408, 2014.

[10] L. Dahmani, A. Khenane, and S. Kaci, "Behavior of the reinforced concrete at cryogenic temperatures," *Cryogenics*, vol. 47, no. 9, pp. 517–525, 2007.

[11] Y. T. Wang, J. Y. Pang, and X. Huang, "Experimental research on compressive strength of rubber concrete with different particle sizes at low temperature," *Bulletin of the Chinese Ceramic Society*, vol. 38, no. 7, pp. 2308–2313, 2019.

[12] Q. Wang, Y. Y. Wang, and H. F. Xing, "An experiment research of mechanics performance of polypropylene fiber concrete under freezing temperature," *Journal of Shihezi University(Natural Science)*, vol. 2, pp. 229–231, 2007.

[13] Y. U. Liang-shu, X. U. Qing-yu, W. A. N. G. Wen-jin, and W. Li-yan, "Study on behaviors of asphalt concrete under low temperature," *Journal of Hydraulic Engineering*, vol. 5, pp. 634–639, 2006.

[14] Z. Fang, S. K. Liu, Z. Y. Huang, and J. T. Chen, "Flexural properties of ultra-high performance concrete under different temperatures," *Journal of the Chinese Ceramic Society*, vol. 48, no. 11, pp. 1732–1739, 2020.

[15] S. Chen, S. Q. Shi, Q. L. He, and J. Li, "Experimental study and numerical simulation on the impact resistance performance of concrete reinforced with metal meshes," *Materials Reports*, vol. 34, no. 20, pp. 20046–20052, 2020.

[16] W. H. Zhang, P. Y. Liu, and Y. J. Lyu, "Dynamic mechanical property of UHPCs: a review," *Materials Reports*, vol. 33, no. 19, pp. 3257–3271, 2019.

[17] S. L. Fan, S. Y. Zhao, B. X. Qi, and Q. Kong, "Damage evaluation of concrete column under impact load using a piezoelectric-based EMI technique," *Sensors*, vol. 18, no. 5, p. 1591, 2018.

[18] Y. He, M. Gao, H. Zhao, and Y. Zhao, "Behaviour of foam concrete under impact loading based on SHPB experiments," *Shock and Vibration*, vol. 2019, Article ID 2065845, 13 pages, 2019.

[19] H. Zhu, A. Liu, and Y. Yu, "Low temperature impact performance of basalt fiber reinforced concrete," *Journal of Materials Science and Engineering*, vol. 36, no. 4, pp. 600–604, 2018.

[20] B. F. Huang and Y. Xiao, "Impact tests of high-strength, lightweight concrete with large spilt Hopkinson pressure bar," *China Civil Engineering Journal*, vol. 54, no. 2, pp. 30–42, 2021.

[21] R. Y. Huang, L. L. Hu, J. Qin, D. Jiang, and L. Meng, "Effect of free water on the mechanical properties and blast resistance of concrete," *KSCE Journal of Civil Engineering*, vol. 25, no. 8, pp. 3084–3096, 2021.

[22] J. Liu, X. L. Du, and G. W. Ma, "Macroscopic effective moduli and tensile strength of saturated concrete," *Cement and Concrete Research*, vol. 42, no. 12, pp. 1590–1600, 2012.

[23] Q. F. Wang, Y. H. Liu, and G. Peng, "Effect of water pressure on mechanical behavior of concrete under dynamic compression state," *Construction and Building Materials*, vol. 125, pp. 501–509, 2016.

[24] D. M. Yan, K. H. Liu, H. D. Li, and S. L. Xu, "A study on the dynamic compressive behavior of pre-damaged concrete," *Journal of Hydraulic Engineering*, vol. 46, no. 9, pp. 1110–1118, 2015.

[25] B. Sun, H. Liu, D. Yuan, F. L. Wang, and S. Zeng, "Damage characteristics of uni-body bi-material specimen for rock-concrete under dry and saturated states," *Bulletin of the Chinese Ceramic Society*, vol. 38, no. 2, pp. 482–487, 2019.

[26] Y. X. Wang, J. Y. Xu, and Y. G. Yin, "Basic properties of water saturated geopolymeric concrete," *Bulletin of the Chinese Ceramic Society*, vol. 35, no. 12, pp. 4237–4241, 2016.

[27] L. Song and S. S. Hu, "Two-wave and three-wave method in SHPB data processing," *Explosion and Shock Waves*, vol. 25, no. 4, pp. 368–373, 2005.

[28] S. J. Liu, L. X. Wu, J. Z. Wang, Y. H. Wu, and Y. Q. Li, "Remote sensing-rock mechanics(VI)-features of rock friction-sliding and analysis on its influence factors," *Chinese Journal of Rock Mechanics and Engineering*, vol. 8, pp. 1247–1251, 2004.

[29] Z. Tao, Q. Geng, C. Zhu et al., "The mechanical mechanisms of large-scale toppling failure for counter-inclined rock slopes," *Journal of Geophysics and Engineering*, vol. 16, no. 3, pp. 541–558, 2019.

[30] Q. Wang, S. Xu, Z. Xin, M. He, H. Wei, and B. Jiang, "Mechanical properties and field application of constant resistance energy- absorbing anchor cable," *Tunnelling and Underground Space Technology*, vol. 125, article 104526, 2022.

[31] Q. Wang, S. Xu, M. He, B. Jiang, H. Wei, and Y. Wang, "Dynamic mechanical characteristics and application of constant resistance energy-absorbing supporting material," *International Journal of Mining Science and Technology*, vol. 32, no. 3, pp. 447–458, 2022.

[32] M. Z. Gao, B. G. Yang, J. Xie et al., "The mechanism of microwave rock breaking and its potential application to rock-breaking technology in drilling," *Petroleum Science*, vol. 19, no. 3, pp. 1110–1124, 2022.

[33] P. Zhang, D. Zhang, Y. Yang et al., "A case study on integrated modeling of spatial information of a complex geological body," *Lithosphere*, vol. 2022, no. Special 10, article 2918401, 2022.

[34] Z. Dou, S. Tang, X. Zhang et al., "Influence of shear displacement on fluid flow and solute transport in a 3D rough fracture," *Lithosphere*, vol. 2021, no. Special 4, article 1569736, 2021.

[35] Q. Yin, J. Wu, Z. Jiang et al., "Investigating the effect of water quenching cycles on mechanical behaviors for granites after conventional triaxial compression," *Geomechanics and Geophysics for Geo-Energy and Geo-Resources*, vol. 8, no. 2, p. 77, 2022.

[36] Y. Wang, Y. L. Li, and C. X. Liu, "Dynamic mechanical behaviors of ice at high strain rates," *Explosion and Shock Waves*, vol. 31, no. 2, pp. 215–219, 2011.